0 0 0 0 4 4 0 2 5 9 6

LBL-4281
c.1

QUANTUM ELECTRODYNAMICS WITH THE SPEAR MAGNETIC DETECTOR

John Edward Zipse
(Ph. D. thesis)

RECEIVED
LAWRENCE
BERKELEY LABORATORY
NOV 1 1 1975
LIBRARY AND
DOCUMENTS SECTION

September 1975

Prepared for the U. S. Energy Research and
Development Administration under Contract W-7405-ENG-48

For Reference

Not to be taken from this room

LAWRENCE BERKELEY LABORATORY
UNIVERSITY OF CALIFORNIA
BERKELEY

LBL-4281
c.1

DISCLAIMER

This document was prepared as an account of work sponsored by the United States Government. While this document is believed to contain correct information, neither the United States Government nor any agency thereof, nor the Regents of the University of California, nor any of their employees, makes any warranty, express or implied, or assumes any legal responsibility for the accuracy, completeness, or usefulness of any information, apparatus, product, or process disclosed, or represents that its use would not infringe privately owned rights. Reference herein to any specific commercial product, process, or service by its trade name, trademark, manufacturer, or otherwise, does not necessarily constitute or imply its endorsement, recommendation, or favoring by the United States Government or any agency thereof, or the Regents of the University of California. The views and opinions of authors expressed herein do not necessarily state or reflect those of the United States Government or any agency thereof or the Regents of the University of California.

0 0 0 0 4 4 0 2 6 9 7

QUANTUM ELECTRODYNAMICS WITH THE SPEAR MAGNETIC DETECTOR

John Zipse

ABSTRACT

Here we make a study of quantum electrodynamic processes which are present at the SPEAR colliding beam magnetic detector. We begin by describing the experiment performed by the SLAC-LBL collaboration and the results concerning the strong interaction. Then the interactions $e^+e^- \to e^+e^-$ and $e^+e^- \to \mu^+\mu^-$ are considered along with their third-order radiative corrections. These events, previously used to determine new limits for cutoff parameters in QED breakdown models, are further studied in this work to show that the full distribution in coplanarity angle fits the theoretical prediction well.

The major focus of this work is on the fourth order two-photon process, $e^+e^- \to e^+e^-A^+A^-$, which only recently has been realized to be significant in such experiments. Cross sections are derived and calculated exactly for this process and the results compared to a Weizacker-Williams equivalent photon calculation. The two-photon data is then isolated and fit to the calculation. A special experiment has been done where the small-angle scattered electron or positron is "tagged" along with particles in the main detector. Cross sections and coplanarity distributions are measured and compared to

calculation. Through these studies, we feel confident that we understand the nature of the two-photon process in our detector. We further explore the hadronic physics of the two-photon process, $e^+e^- \rightarrow e^+e^-$Hadrons, measuring pion cross sections, searching for resonances, and discussing future experiments.

0 0 0 0 4 4 0 2 6 9 8

ACKNOWLEDGEMENTS

I would like to gratefully acknowledge the work of the entire SLAC-LBL collaboration as well as the physicists and engineers involved in the construction and operation of SPEAR. In particular I would like to thank my advisor Professor W. Chinowsky for his direction and guidance of my graduate work. I would like to thank those with whom I have worked closely for contributing to my education and for their encouragement and companionship. Also I thank typists Jeanne Miller and Chris Stark and the many technical people who helped me to complete this thesis.

0 0 0 0 4 4 0 2 6 9 9

TABLE OF CONTENTS

		Page
I.	Introduction	1
II.	Description of the Magnetic Detector	4
	A. Detection Devices	4
	B. Trigger	13
	C. Event Reconstruction	13
	D. Background	20
	E. Resolution and Cutoffs	22
III.	Hadronic Cross Sections	27
	A. Determining the Detected Cross Section	28
	B. Unfolding the Cross Section	32
	C. Measured Cross Section	35
	D. The Narrow Resonances	35
	E. Present and Future Studies	45
IV.	Second and Third Order QED Cross Sections and the Radiative Corrections	46
	A. Calculation of the Cross Sections	47
	B. Test of Quantum Electrodynamics	51
	C. Fit of the Coplanarity Distributions	60
V.	Fourth Order QED Cross Sections and the Two-Photon Process	72
	A. Order of Magnitude Estimates	74
	B. The C = + Two-Photon Process	78
	C. The C = - Process	109
	D. Two-Prong Data	111
	E. "Tagged" Two-Prong Data	127
	F. Subtraction of Fourth Order Contamination	136
	G. Hadron Physics with the Two-Photon Process	138
VI.	Conclusion	148

References..... 149

Appendix A..... 152

Appendix B..... 154

I. Introduction

In the summer of 1973 construction and testing of the magnetic detector at SPEAR was completed, and preliminary data taking began on electron-positron annihilation in the center-of-mass energy region of 2.0 to 4.8 GeV. SPEAR is an electron positron storage ring fed by the Stanford Linear Accelerator, SLAC. It contains two interaction regions, one of which is reserved for a semi-permanent, large-solid-angle, charged-particle magnetic detector. The detector was constructed and used by a collaboration of physicists from the Stanford Linear Accelerator Center and the Lawrence Berkeley Laboratory. The experiments performed with this detector have yielded some very exciting results on high energy particle interactions and are presently continuing to do so.

The initial aims of the detector were threefold. First, the study of electron-positron scattering and annihilation into muon-antimuon pairs would provide a more stringent test of the theory of quantum electrodynamics than has ever been previously performed. Not only could total cross sections be measured, but angular distributions could be fit to various breakdown models to provide limits on anomalous effects.

The second aim of the detector would be to measure the timelike total hadronic cross section through electron-positron annihilation and to provide details on the prong multiplicities and momentum spectra. This would hopefully lead to new tests of existing theories,

particularly in their asymptotic predictions, and possibly lead to a new and more comprehensive theory of the strong interaction.

Finally, the detector would provide the ability to search for any new and unpredicted particles which exist in the previously unexplored mass range of 2.0 to 4.8 GeV/c^2. An electron-postitron pair annihilating to a photon have $J^{PC} = 1^{--}$ and lepton and baryon numbers 0. Thus the high energy photon can decay directly to any single vector meson and to practically any conceivable pair of particles with threshold below 4.8 GeV. In particular, the search would be on for new heavy leptons which could fit neatly into existing theories of weak and electromagnetic interactions.

The results of the experiment so far have more than fulfilled the aims. Of course the discovery of the vector mesons $\psi(3095)$ and $\psi(3684)$ is the most important single result. The properties of these particles and the hadronic cross section as measured by the magnetic detector have literally added a new dimension to high energy particle theory. Also of related and great importance is the verification of quantum electrodynamics to new accuracies both through Bhabha and muon production and through the fourth order two-photon process.

Several publications [1,2,3,4,5,6,7,8] have already appeared in the literature on the hadronic results of the magnetic detector. Therefore this work will concentrate primarily on the quantum electrodynamic predictions and results of the experiment. The purpose for this is twofold. First the beautiful agreement of the Bhabha and mupair cross sections with the third order predictions of Berends,

Gaemers, and Gastmans[9,10,11] is a huge success for quantum electrodynamics. A similar success is the agreement of fourth order QED cross sections with the predictions of Brodsky, Kinoshita, and Terazawa[12] and this work.

The other reason for exploring these cross sections in depth is to instill confidence in our separation of these events from the hadronic events. Indeed the separation is complete for hadronic events with three or more detected prongs. Contamination levels of the order of a few percent can be calculated for the two-prong hadron class with momentum greater than 300 MeV/c and coplanarity $20° < \psi < 160°$. These two classes comprise the hadron data used in previous works.

In section II we will describe the ring and detector and discuss the elimination of background due to beam-gas and beam-pipe interactions and cosmic rays. In section III we will briefly review the hadronic results from the magnetic detector and refer the reader to the literature for further information. Section IV will provide a detailed study of second and third order QED processes at SPEAR and compare predictions with magnetic detector data. Similarly in section V we will discuss the fourth order QED processes and in particular the two-photon process. The cross section for this process has been seen to be large in previous storage rings and is now known to increase logarithmically with energy. Fourth order four-prong events have been seen at SPEAR where two, three, and four of the prongs are detected. All cross sections are in excellent agreement with theory. This work concludes with section VI.

II. Description of the Magnetic Detector

A. Detection Devices

SPEAR is a single-ring, electron-positron storage ring which in its first phase was capable of colliding beams with energies from 1.0 to 2.5 GeV. The ring is shown in Fig. 1. Beams are injected at 1.5 GeV from the Stanford Linear Accelerator, SLAC. SPEAR is capable of accelerating them to 2.5 GeV or decelerating them to 1.0 GeV by changing the magnetic fields. This process is controlled by changing the magnetic fields. This process is controlled by an XDS Σ5 computer which is dedicated solely to SPEAR. As can be seen, there are 18 magnet sections consisting of bending magnets and focusing and defocusing quadrupoles. The ring can handle luminosities of up to 10^{31} $cm^{-2}sec^{-1}$ with lifetimes of several hours.

The particles travel in bunches rather than continuous bands. There is one bunch each of electrons and positrons and hence two regions in the ring where they intersect. These two regions are set up as experimental areas. The beams are well focused in transverse dimensions in the intersection regions, and large pit areas are available for experimental apparatus.

The west pit area is reserved permanently for the magnetic detector, shown in Figs. 2 and 3 and 4 in its most recent stage of development. The primary components of the detector are a 4 kG magnetic field coil surrounding four groups of cylindrical spark chambers, and a group of scintillation and shower counters to provide an event trigger. As a whole, the detector can detect all charged particles within roughly 2/3 of 4π steradians and

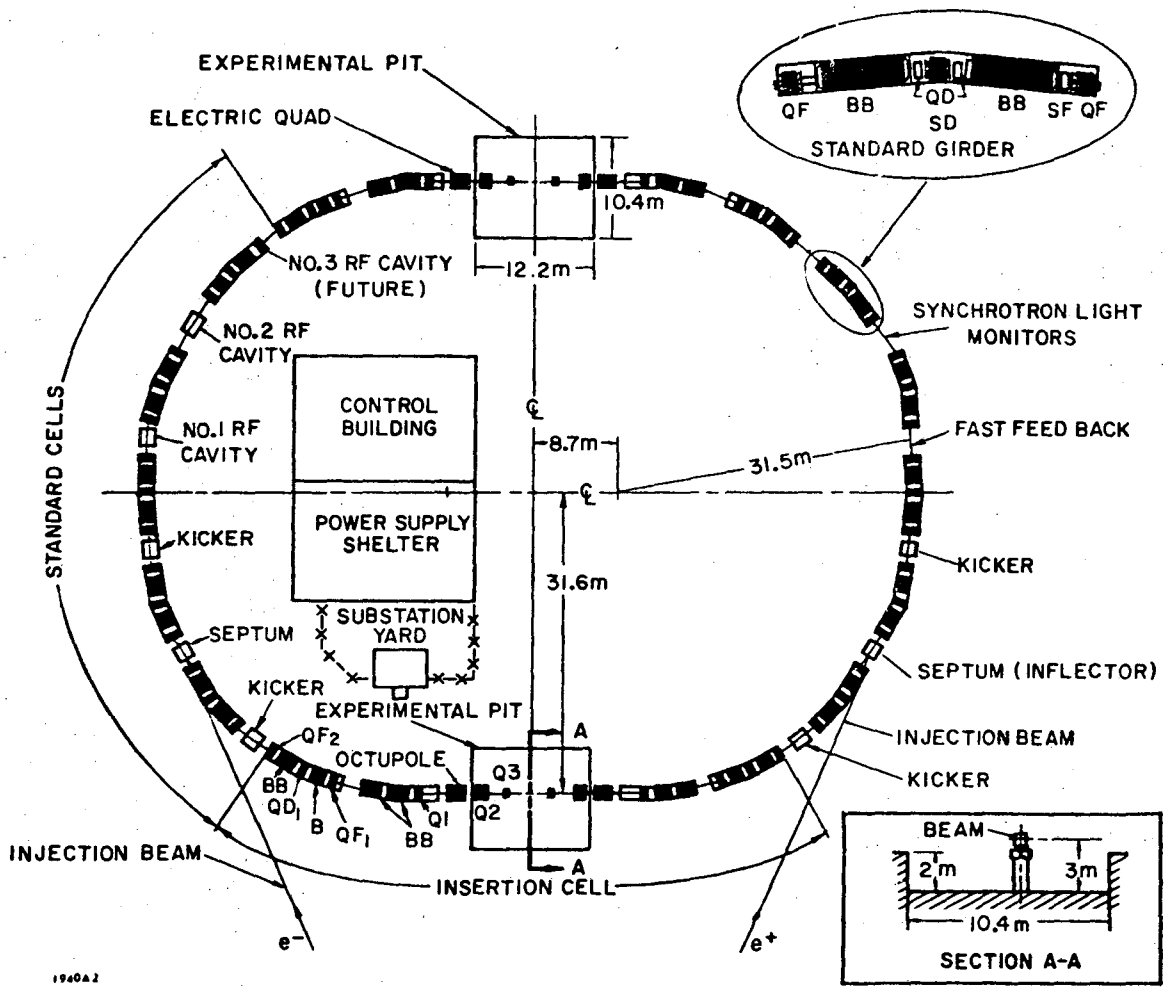
EXPERIMENTAL PIT
ELECTRIC QUAD
QF
BB
QD
SD
BB
SF QF
STANDARD GIRDER
10.4m
12.2m
NO.3 RF CAVITY
(FUTURE)
SYNCHROTRON LIGHT
MONITORS
NO.2 RF
CAVITY
CONTROL
BUILDING
NO.1 RF
CAVITY
8.7m
31.5m
FAST FEED BACK
STANDARD CELLS
KICKER
POWER SUPPLY
SHELTER
31.6m
KICKER
SUBSTATION
YARD
SEPTUM
SEPTUM (INFLECTOR)
KICKER
EXPERIMENTAL PIT
A
INJECTION BEAM
QF2
OCTUPOLE
Q3
KICKER
BB
QD1
B
QF1
BB
Q1
Q2
A
INJECTION BEAM
INSERTION CELL
e−
e+
BEAM
2m
3m
10.4m
SECTION A-A

Figure 1

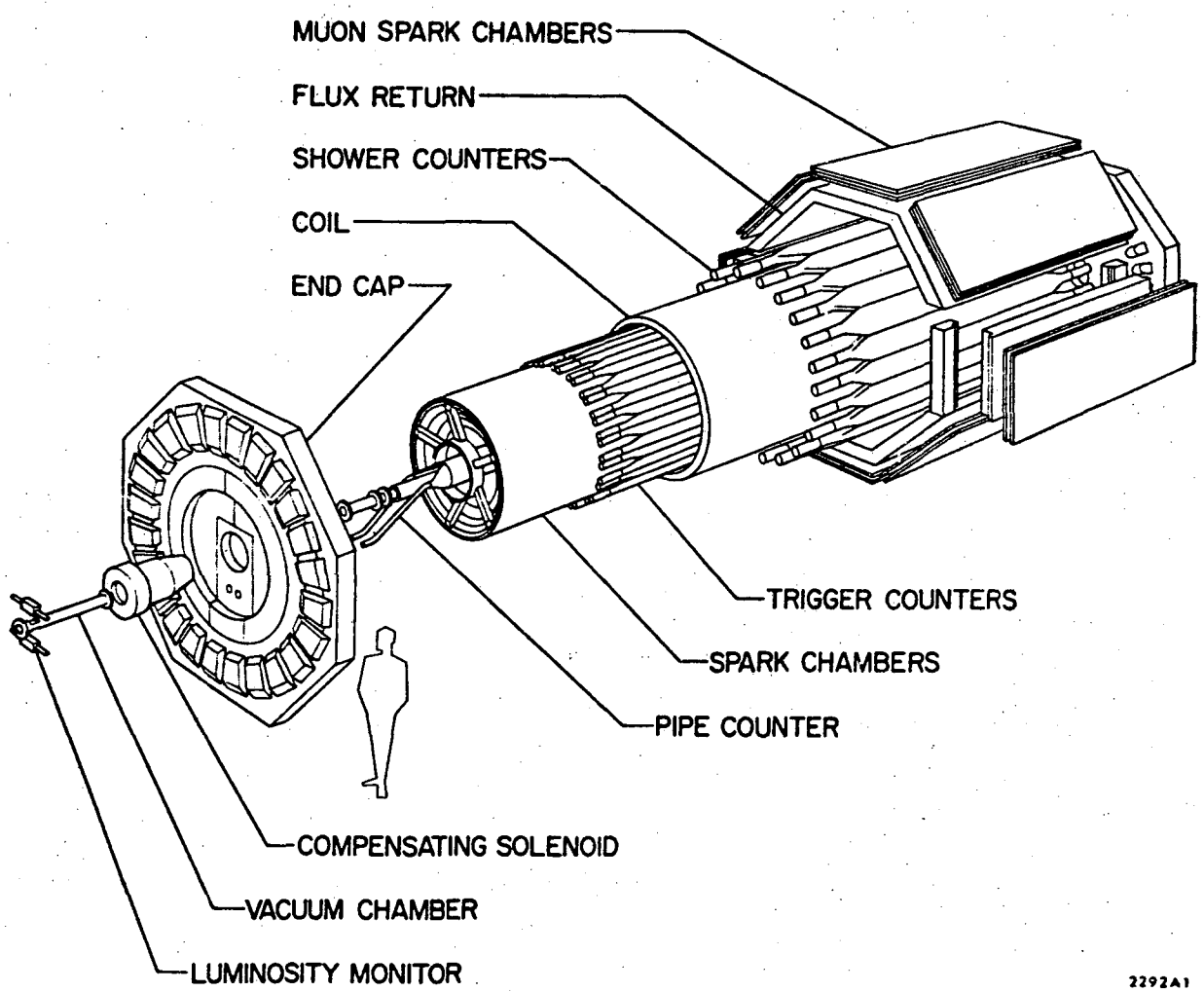
MUON SPARK CHAMBERS
FLUX RETURN
SHOWER COUNTERS
COIL
END CAP
TRIGGER COUNTERS
SPARK CHAMBERS
PIPE COUNTER
COMPENSATING SOLENOID
VACUUM CHAMBER
LUMINOSITY MONITOR
2292A1

Figure 2

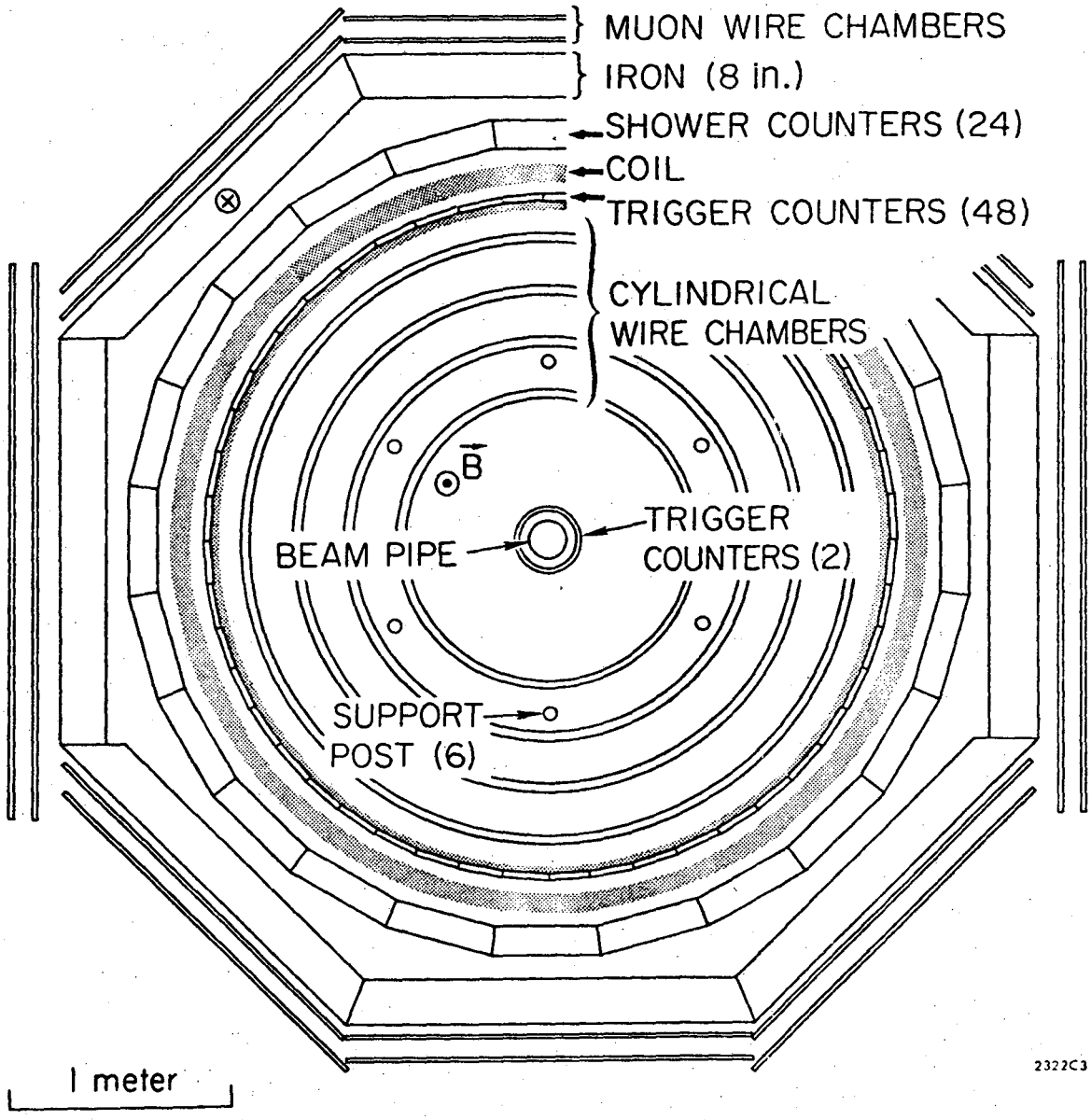
MUON WIRE CHAMBERS
IRON (8 in.)
SHOWER COUNTERS (24)
COIL
TRIGGER COUNTERS (48)
CYLINDRICAL
WIRE CHAMBERS
B
TRIGGER
COUNTERS (2)
BEAM PIPE
SUPPORT
POST (6)
1 meter
2322C3

Figure 3

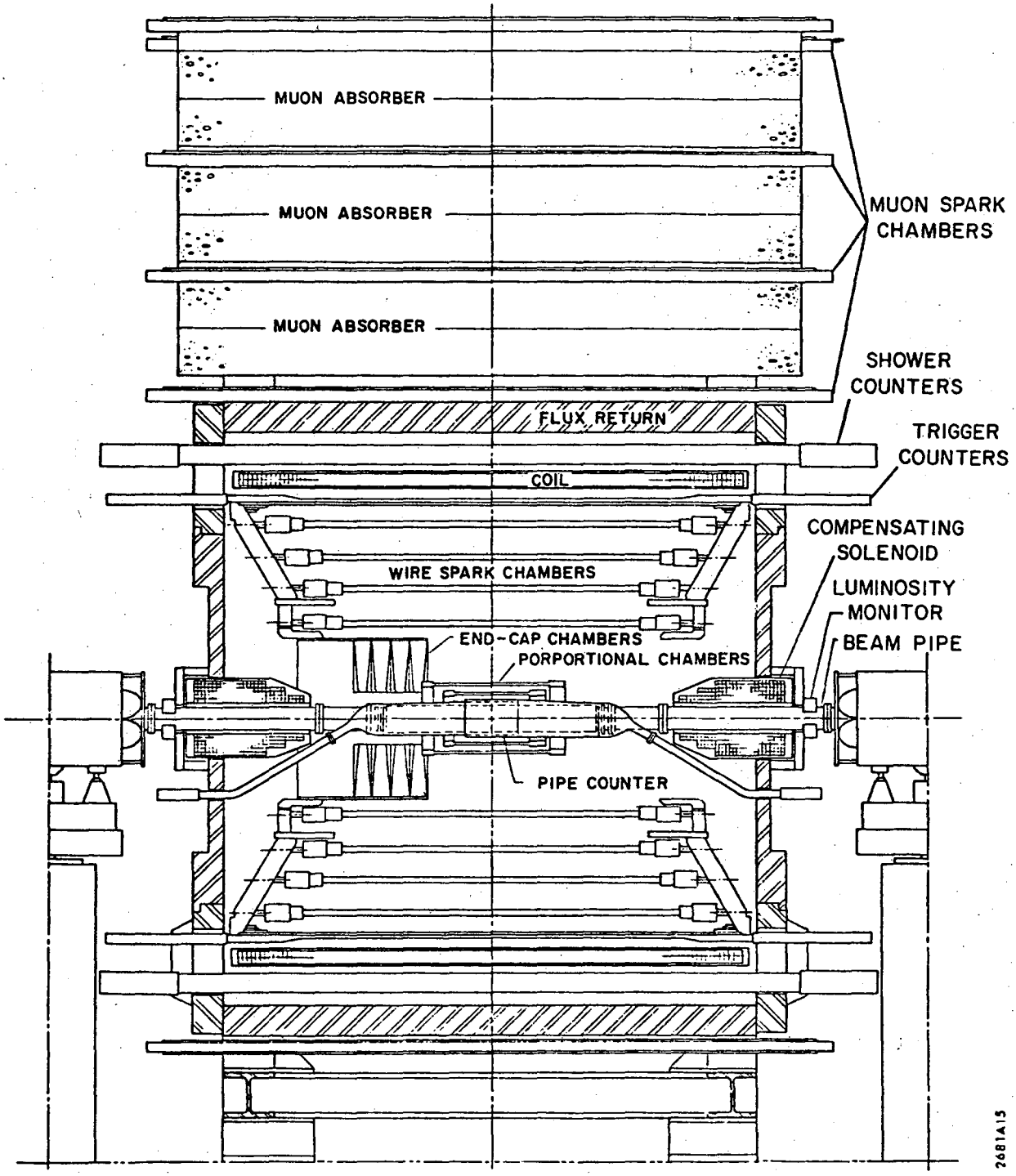
MUON ABSORBER
MUON ABSORBER
MUON ABSORBER
MUON SPARK CHAMBERS
SHOWER COUNTERS
FLUX RETURN
TRIGGER COUNTERS
COIL
COMPENSATING SOLENOID
WIRE SPARK CHAMBERS
LUMINOSITY MONITOR
END-CAP CHAMBERS
BEAM PIPE
PORPORTIONAL CHAMBERS
PIPE COUNTER
2681A15

Figure 4

will trigger on any event with two or more detected charged tracks. We will describe each of the detection devices in the order they are seen by produced particles, starting with the beam pipe and progressing to the muon spark chambers.

Fig. 4 is a side view of the detector. Electrons and positrons enter from the left and right respectively and collide in the center. There are 1.28×10^6 beam intersections per second which produce on the order of one event a second at full luminosity. The beam pipe must be sturdy and well evacuated for long beam lifetimes and thin to reduce multiple scattering. It is made of 6 mil of corrugated stainless steel.

Surrounding the beam pipe are the first triggering devices. In Fig. 4, the most recent version of the detector, two scintillation counters (pipe counters) and two proportional chambers are shown, as well as endcap spark chambers. When the data described in this work were taken, however, there was a single pipe counter consisting of two halves, front and rear in the figure, each with a phototube at the left and right ends. The pipe counter halves were semi-circular pieces of 3 mm scintillator, 91 cm long and 13 cm from the beam line. Two of the four phototubes were required to have pulses in them for the pipe counter to have "fired."

Next in the path are the four modules of cylindrical spark chambers. The modules are 2.2 meters in length and .66, .92, 1.12, and 1.35 meters in radius. Each module consists of two spark gaps, the outer one composed of two "cylinders" of wires oriented at +2° and -2° to the longitudinal, and the inner gap composed of similar

"cylinders" at ±4°. The wires are spaced 1 mm apart and are pulsed with high voltage when the trigger signals an event has passed. A magnetostrictive wand readout system is employed to determine which wires have sparked. This information will then yield "points" on the charged particle tracks accurate to within 0.5 mm in the azimuthal direction and 7 mm for the 4° gaps and 14 mm for the 2° gaps in the longitudinal direction provided the position of the chambers themselves is known. The two gaps in each module make the chambers very efficient (>99%) at finding at least one point on a track at each radius.

Surrounding the spark chambers is the next part of the triggering aparatus, a ring of 48 trigger counters made of 2.5 cm thick scintillator. The trigger counters are arranged such that each subtends 1/48 of the 2π azimuth and a pair is located underneath each of the 24 shower counters. There is a phototube at each end of each counter, and both are required to pulse to have a trigger counter "fire." The trigger counter efficiency is 100% for $0 < |\cos\theta| < 0.5$ and 97% for $0.5 < |\cos\theta| < 0.6$.

Each trigger counter also measures the time at which the particle passed through relative to the time the beams crossed. This time is typically 6-8 ns and is measured to an accuracy of .5 ns. From this information and the track path length determined by the spark chambers, $\beta = v/c$ is calculated for the particle. This leads ultimately to pion-kaon separation on a track-by-track basis for particles with momenta less than about 0.3 GeV/c. (See Fig. 10)

Next is the magnetic field coil which creates a 4 kG magnetic field in the region of the spark chambers. The iron flux return surrounds the entire detector to keep the field uniform with openings for the beam pipe and phototubes only. Compensating solenoids around the beam pipe provide for beam stability. The field is close enough to uniform (2%) to make charged particles travel in helical paths. Field non-uniformities are parameterized as a function of position to within .1% in order to minimize momentum measurement errors due to field inhomogeneities.

Between the coil and the flux return is a ring of 24 shower counters. Each one is a sandwich of 5 layers of 1/4 inch lead interleaved with five layers of scintillator. The shower counters have a dual purpose. They are used in the trigger and they provide electron-muon separation for 1 GeV/c particles and above. Electrons deposit all of their energy in the counters and yield large pulse heights, while more massive particles pass through giving small showers.

Finally outside of the iron flux return is a double layer of spark chambers which will detect particles which pass through the iron. Hadrons interact strongly in the iron and deviate significantly from their incident direction while electrons range out in the shower counters. This leaves the muons which need about 600 MeV/c of momentum to reach the chambers. The muon chambers do not give a clear particle separation and have not been used extensively to date. Improvements have recently been made, and the current system is shown in Fig.4 with concrete muon absorbers (which absorb the hadrons, not the muons) interleaved with the spark chambers.

The last detection device is the set of four luminosity monitors. These are 2.5 cm by 7.5 cm tungsten shower counters with defining counters in front, designed to measure the small-angle Bhabha cross section for a real time luminosity determination. The shower counters consist of eight layers of one radiation length of tungsten interleaved with eight layers of scintillator. They are located at an angle of 25 mr to the beam axis and set above and below the beam pipe at each end of the detector in specially designed notches 220 cm from the interaction region. To detect a Bhabha event, they require the defining and shower counters of two opposite monitors to fire in coincidence. Accidentals are simultaneously measured by recording similar coincidences, but with the signal from one counter delayed by one revolution of the beams. When used as luminosity monitors these counters are not gated by the detector trigger and have typical rates of 250 events/sec ($L = 10^{31}$ $cm^{-2}sec^{-1}$, $E = 2.4$ GeV).

The luminosity monitors have a second important function. They are used as "tagging" counters for measuring the fourth order two-photon events. The events, the subject of section V, are the result of collision of two bremsstrahlung photons and have surprisingly large cross sections. It is useful to detect the scattered electron and positron to measure such cross sections, and this is done by the luminosity monitor. When used for this purpose, pulses in the monitors are recorded with each event, and again both defining counter and shower counter are required for a "fire."

B. Trigger

The detector was designed to have a flexible triggering mode, but the most useful trigger for recording data was the one that required two or more charged particles in the detector.

The presence of a charged particle was detected by the firing of a trigger counter and an associated shower counter (TASH) during the passage of the beams. The 1.28 megacycle frequency of the beams gave a 780 ns revolution time and a 30 ns gate was opened with each crossing. Two TASH's as well as the pipe counter were required to fire in order to have an event.

When the presence of an event was detected, the triggering system was made inactive for .3-.5 sec while the spark chambers were pulsed with high voltage. Data from the magnetostrictive wands was recorded along with pulse heights from all of the counters. The event was then analyzed in real time, points determined and tracks and counters displayed, and the system was again made active to detect events.

The major source of dead time was the .3-.5 seconds required for the spark chambers to pulse and clear. This limits the rate at which events could be recorded on tape to 2-3/sec. Events could be analyzed and displayed in real time at the rate of about one per two seconds. The entire system was controlled by the Σ5 computer and required the operator only to start it and to watch out for problems.

C. Event Reconstruction

Once the data has been recorded, careful event analysis is done offline on IBM 360 and CDC 7600 computers. The primary information

used comes from the spark chamber data which provide momentum and charge for charged particle tracks. Other significant information comes from the trigger counter flight times, the shower counter pulse height, and the muon spark chambers.

The first step in track reconstruction is to determine the azimuthal positions of the spark chamber wires which have fired. For each real spark which occurs in a chamber, two wires will carry a current across the magnetostrictive wands, one wire from the outer cylinder of wires and one from the inner. Since the wires are skewed at a small angle to the longitudinal, but in opposite directions, finding the azimuthal positions of the two wires will determine the point in space at which the spark occurred. (See Fig. 5.)

The magnetostrictive wands are read and the set of all wires which pulsed is determined. Each pair of pulsed wires is then examined to determine if the two wires could have pulsed due to the same physical spark. For each such pair, the wire azimuthal angles are used to find r, θ, and z coordinates for the spark using the standard coordinate system of Fig. 6. The sum and difference of the azimuthal angles directly yield θ and z while r is taken to be the average of the radii of the two wires. Careful corrections are made to these r, θ, z values to account for the skewing of the wires, the placement of the wands, ExB drift of the ions, and inaccuracies in the positioning of the chambers. A set of almost 300 parameters is determined by fitting tracks with known characteristics (Bhabhas, cosmics, etc.) to

PARTIAL SECTION OF ONE GAP OF WIRES

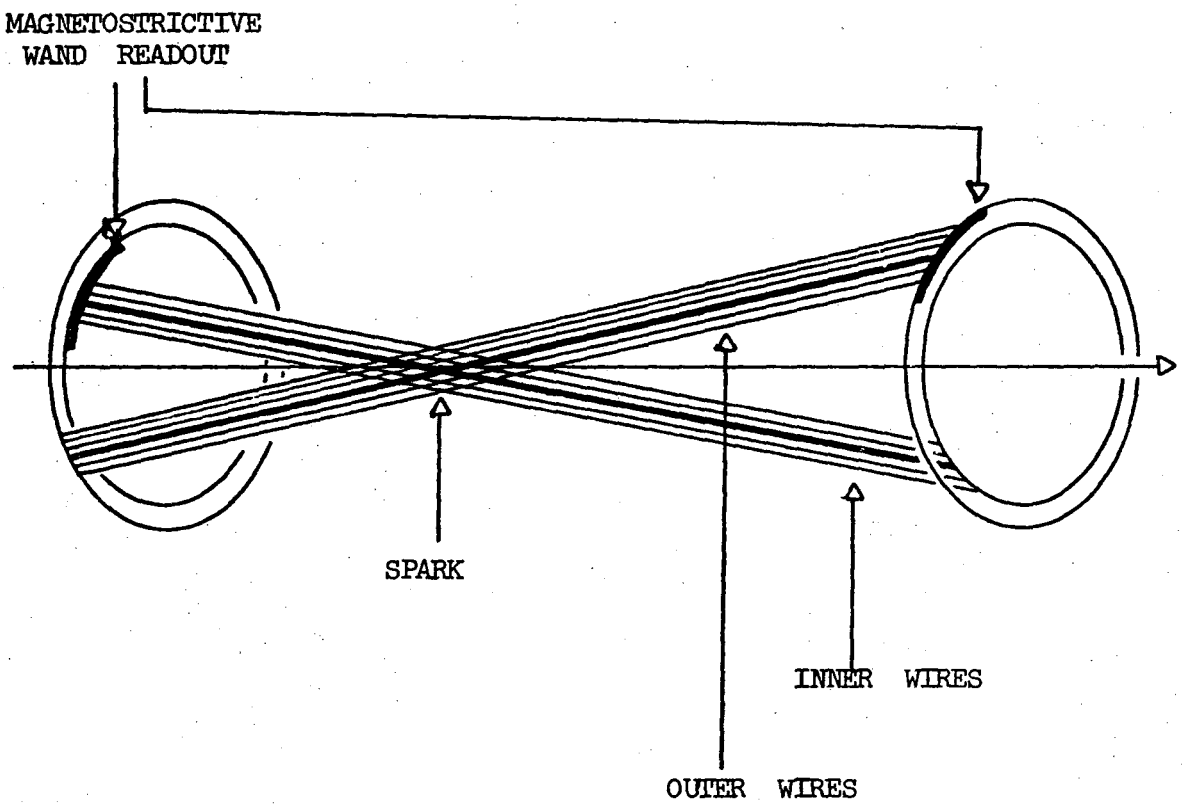

XBL 756-1719

Figure 5

MAGNETIC DETECTOR COORDINATE SYSTEM

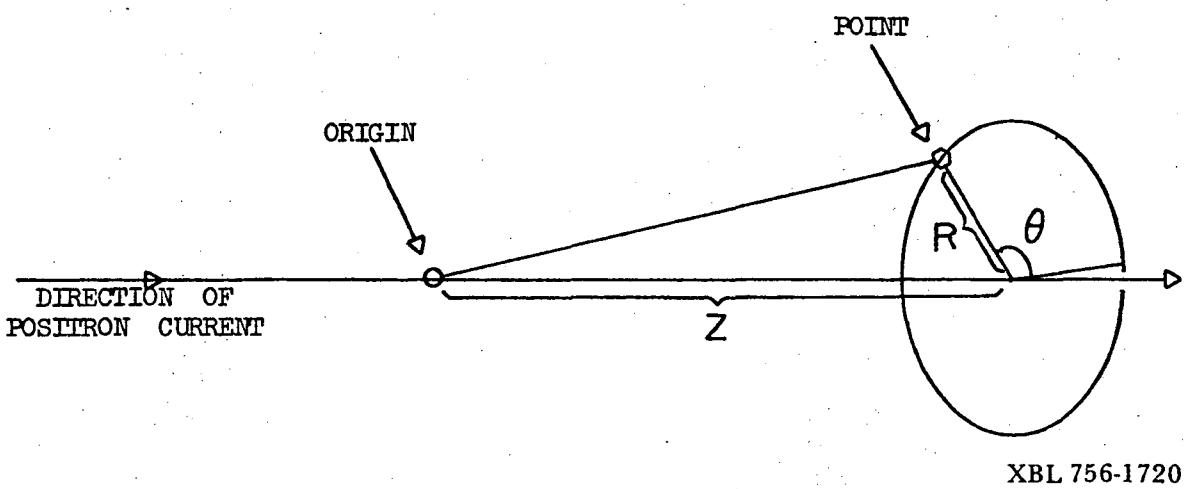

Figure 6

predicted r, θ, z values. These parameters fix the location in space of the wands and cylinders to a better precision than obtained during construction.

With a bank of coordinate locations found, the programs use several different algorithms to connect them into curved tracks in the magnetic field. All algorithms use loose bounds to connect points, allowing for multiple scattering and field errors. No spark is used in more than one track. Since finding at least one spark on the two gaps of each chamber is so probable, the efficiency for finding all tracks with at least two points on each is almost perfect (99.7%). For each track, a momentum is found from the curvature using the corrected magnetic field. Then a grand fit is done for all of the tracks, requiring a single vertex but not requiring energy or momentum conservation. The program CIRCE[13] is used, which minimizes the χ^2 error in the fit by varying the momenta of the tracks and the position of the vertex. The result of the track reconstruction is a number of charged tracks, a momentum and charge for each track, and a vertex position.

The accuracy of the momenta determined by the detector is crucial to most of the results it has produced. This accuracy is most closely dependent upon the accuracy with which the sagitta, s in Fig. 7 can be measured. The accuracy of s is roughly the same as the accuracy of a measured point. Consider Fig. 7:

$$s = \rho - \rho \cos(\theta) \approx \frac{1}{2} \rho \left(\frac{L}{2\rho}\right)^2 = \frac{L^2}{8\rho}$$

where ρ is the radius of curvature for a nearly circular track and

PARTICLE TRACK WITH SPARKS

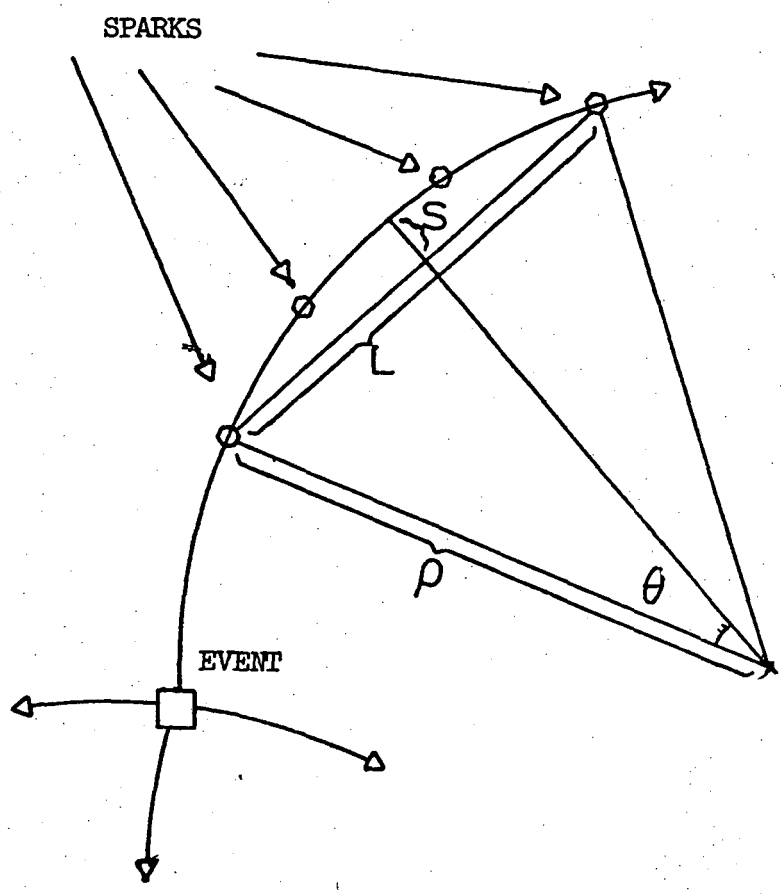

XBL 756-1721

Figure 7

L is the farthest distance between any two measured points. Using this formula and the relationship between momentum and radius of curvature:

$$p(\text{in GeV/c}) = .03\rho(\text{in m})\ B(\text{in kG})$$

one can derive the following crude formulas:

$$\frac{\Delta p}{p} = .14\ p(\text{in GeV/c})\ \Delta s(\text{in mm}) \quad \text{non-constrained } (L = .7)$$

$$\frac{\Delta p}{p} = .036\ p(\text{in GeV/c})\ \Delta s(\text{in mm}) \quad \text{constrained } (L = 1.4).$$

The first is for tracks not constrained to pass through the beam origin and the second is for tracks which are (an imaginary spark is placed at the origin).

Here, if Δs is assumed to be the error in the measurement of a space point rather than the sagitta, these formulas provide a useful means for estimating errors due to several effects. The most probable sources of error are the following:

1) Magnetic field errors not accounted for by the field parameterization. This will be constant and very small

$$\frac{\Delta p}{p} = \frac{\Delta B}{B} < .001.$$

2) Errors due to multiple scattering. These errors are theoretically the worst. For non-constrained fits, $\Delta\theta = (1.0\ \text{MeV/c})/p$ due to multiple scattering on the material in the spark chambers. For tracks constrained to pass through the origin, the beam pipe and pipe counter provide an additional $\Delta\theta = (1.4\ \text{MeV/c})/p$.

3) Errors due to wire spacing. The physical ions formed in a spark must travel to ground via a physical wire, even though the

spark may occur between two wires. The wand signal, however, displays the currents in all of the wires near the spark, and the centroid of the current distribution gives the spark position to a better accuracy than the 1 mm wire spacing. Depending on the hypothesis used for ion travel, the one standard deviation error in spark position varies from $\Delta s = 0.15$ mm at best to $\Delta s = 0.25$ mm using the worst model.

4) Errors due to chamber misalignments. These are the errors which are eliminated by fitting the 300 parameters to tracks with known properties. The best way to measure the residual error here is to measure the spread in momenta $\Delta p/p$ for tracks with known momenta. This $\Delta p/p$ will include errors from all of the above sources as well as chamber misalignments. At present $\Delta p/p = .04p$ (in GeV/c) for non-constrained fits which give a total $\Delta s = 0.3$ mm. This is the sum of errors due to all sources and demonstrates quite a remarkable determination of the position of chambers with dimensions in meters since Δs due to all other errors is very close to this value.

D. Background

The detector does an excellent job of eliminating events not derived from beam-beam interactions, background events. We will consider briefly the means for eliminating the three major types of background events: cosmic rays; beam-produced, photon-beam pipe collisions; and beam-gas interactions.

Cosmic rays incident on the detector can be mistaken for real events since the long single track passing from one trigger counter

to another can look like two single tracks coming from the vicinity of the beam. Cosmics are easily flagged in event analysis, however, by their unusual flight times recorded by the trigger counters. Also the "event" vertex is usually far from the beam axis. They remain a nuisance however since cosmics can "fire" two TASH's and the pipe counter at the rate of 1 per second. The inclusion of the pipe counter in the trigger and its duty cycle of only 3.8% (the time when the beams cross) is primarily to reduce the cosmic rate, but still there is no way to avoid logging a significant number of them onto tape.

Beam-pipe collisions occur when a bremsstrahlung photon produced by one of the incident beams collides with the beam pipe and produces enough particles to trigger. Most of these events are eliminated by putting a vertex cut on the events. Beam-beam events will have vertices at the origin with standard deviation in $r \approx 3$ cm. Beam-pipe events have vertices at the beam pipe, $r = 6$ cm, with a similar standard deviation. The vertex cut is made at $r = 3$ cm.

Beam-gas events occur when a beam particle collides with a particle of residual gas in the beam pipe. These events are similarly reduced, but not completely eliminated with a vertex cut. They will generally occur at the origin in r, θ space so the r cut does not eliminate them. The vertices, however, are uniformly distributed in z from -45 cm $< z <$ 45 cm while beam-beam event vertices seldom lie outside of $|z| < 30$ cm. The vertex cut in z is made at $|z| = 30$ cm and the number of background events not eliminated is estimated from the number of events with vertices $30 < |z| < 45$.

E. Resolution and Cutoffs

The spark chambers will measure the momenta of all tracks with

$$|\cos\theta| < 0.6, \quad p > 150 \text{ MeV/c}$$

or equivalently

$$|\cos\theta| < 0.6, \quad p > 200 \text{ MeV/c}.$$

It can measure somewhat beyond these bounds, but these are the standard safe cuts. The momentum resolution is roughly

$$\frac{\Delta p}{p} = .14\ p(\text{in GeV/c})\ \Delta s(\text{in mm}) \quad \text{non-beam constrained}$$

$$\frac{\Delta p}{p} = .036\ p(\text{in GeV/c})\ \Delta s(\text{in mm}) \quad \text{beam constrained}$$

with Δs on the order of .3 mm.

The triggering efficiency for two or more prong events in the detector is reduced only by shower counter inefficiencies. Trigger counter and pipe counter efficiencies are >99% for tracks with $p > 200$ MeV/c. Fig. 8 shows the shower counter efficiency as a function of z measured from cosmic rays; the dip at $z = 0$ is due to light attenuation. Fig. 9 shows the dropoff in efficiency for low-momentum pions due to ranging out in the field coil.

The shower counter efficiency for an electron or muon is $95 \pm 5\%$ for $225 \text{ MeV/c} < p < 400 \text{ MeV/c}$ and 100% for $p > 400$ MeV/c, determined from events where the shower counter fire was not necessary for a "trigger." In the effective two-photon calculations in section V the data are cut to require $p > 225$ MeV/c and $95 \pm 5\%$ as the shower counter efficiency, since most of the cross section is below $p = 400$ MeV/c.

0 0 0 0 4 4 0 2 7 1 1

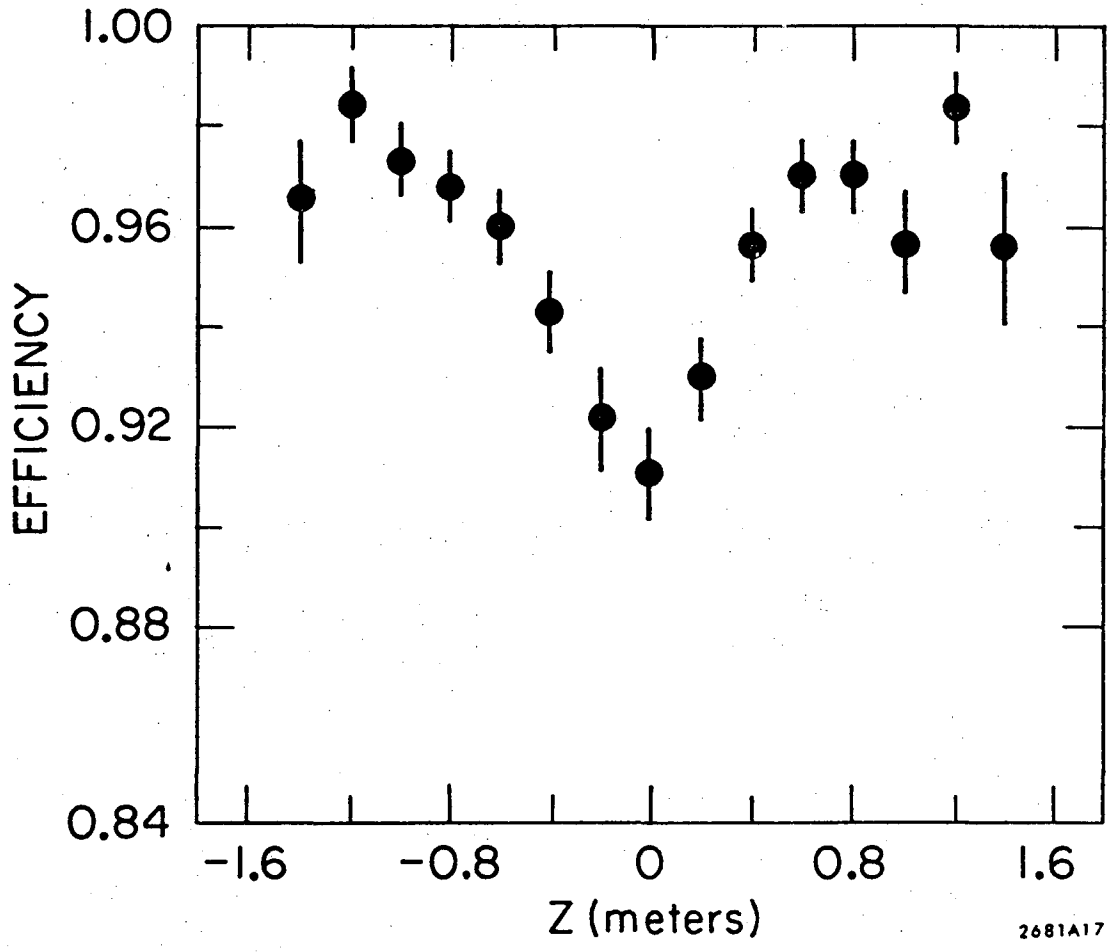

Figure 8

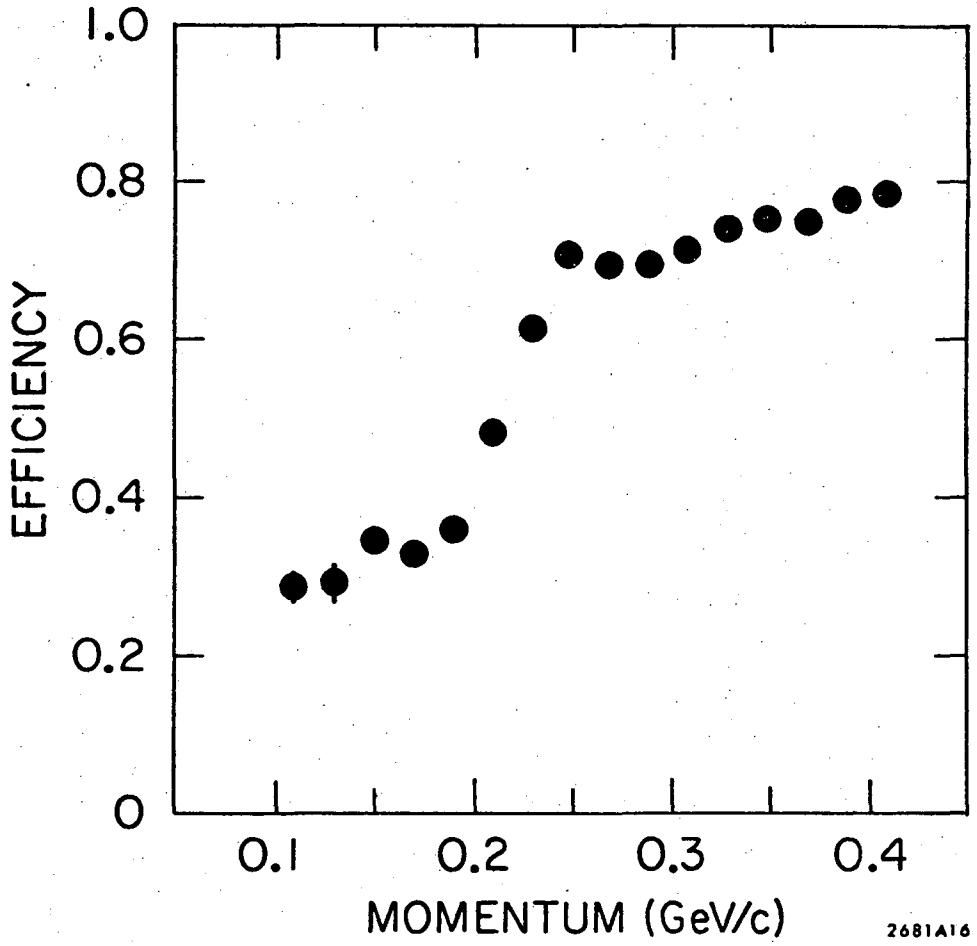

Figure 9

Particle identification (energy determination) is done in three separate ways. Trigger counter flight times, measured to .5 ns allow measurement of $\beta = v/c$.

Fig. 10 is a scatter plot of p versus β for a sample of hadronic events at 2.4 GeV beam energy. Theoretical curves for several particles are shown. (The blank area around the muon and pion curves should really be filled in with black.) As can be seen, pion-kaon separation is impossible above about p = 300 MeV/c using this method on a track-by-track basis. Shower counter pulse heights serve to separate electrons from more massive particles above about p = 1 GeV/c. They are used primarily to separate $e^+e^- \rightarrow e^+e^-$ from $e^+e^- \rightarrow \mu^+\mu^-$. Finally the muon spark chambers will signal muons which make it through the iron flux return. This requires a muon to have p > 600 MeV/c but contamination by pions is non-negligible.

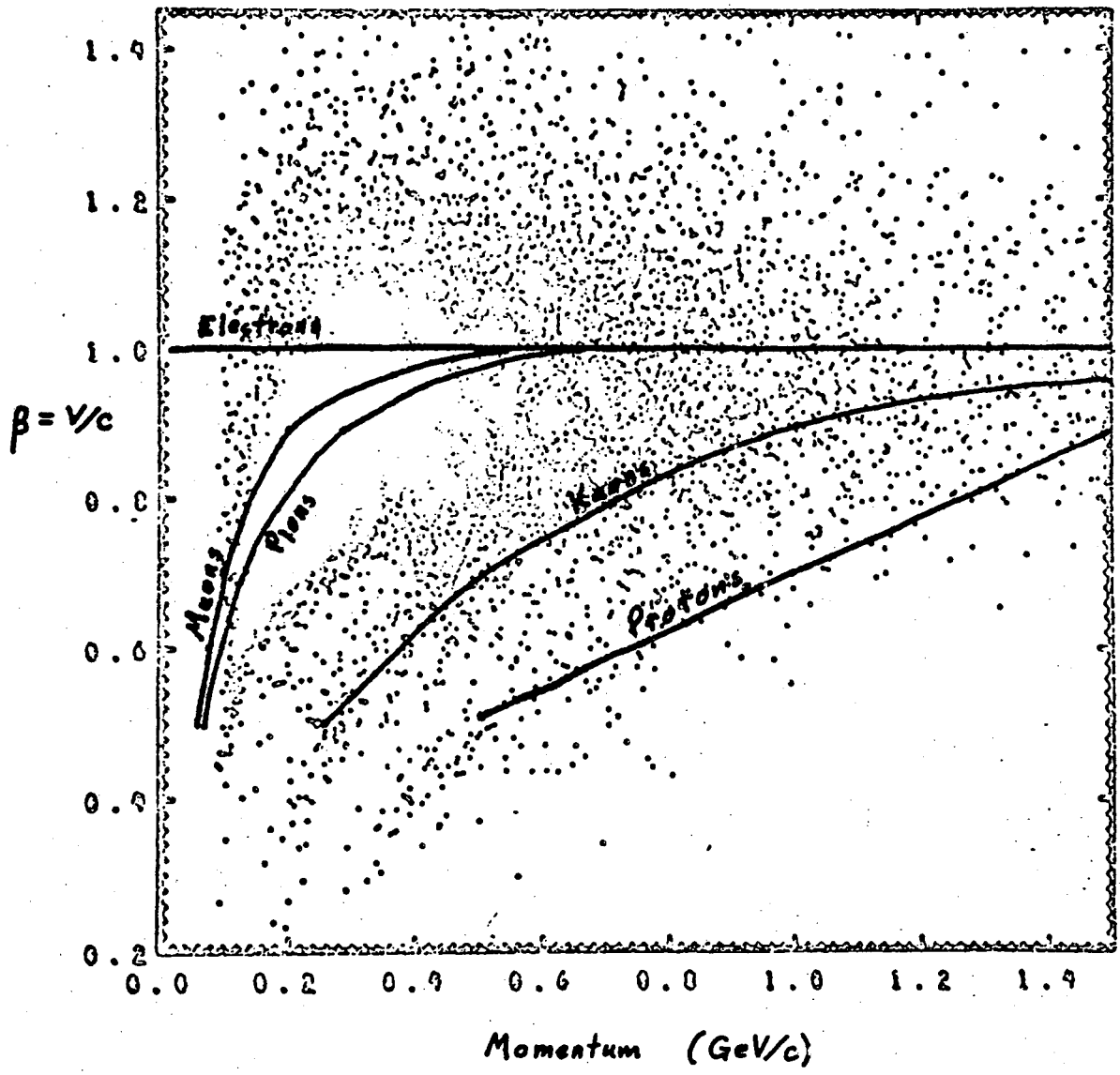

XBL 758-7961

Figure 10

III. Review of Hadronic Results

We begin the presentation of the detector data results with a brief review of the important hadronic or strong interaction results which have already been published. References will be given covering all publications by the SLAC-LBL group to date. The hadronic results consist of a measurement of the cross section for

$$e^+e^- \rightarrow \text{hadrons}$$

in the energy range 2.0 to 5.0 GeV, as well as the interesting resonant results at 3.1 and 3.7 GeV.

All known particle interactions can be put into four classes:

1) Gravitation
2) Electromagnetism
3) Strong Nuclear Interaction
4) Weak Nuclear Interaction.

Gravitational interactions are well understood but so weak that they are significant only when the other interactions are neutralized, that is for large masses of stable, slow-moving, and electrically neutral atoms. The electromagnetic interaction is similarly well understood in terms of the theory of relativistic quantum electrodynamics, QED. This theory predicts that all electromagnetic interactions are well described by the pointlike exchange of photons between charged particles. Cross sections can be calculated for all QED processes and the agreement with experiment has been excellent. In sections IV and V of this work we will use the detector data to make the most stringent tests of QED to date.

Again QED will be verified and we will be confident in our theoretical predictions for the electromagnetic interaction. The last two interactions, strong and weak nuclear, are not well understood in theory. Many models attempt to describe the interactions but none is complete and satisfying. It was hoped that SPEAR would shed some light on the subject as indeed it has, but the new structures found at 3.1 and 3.7 GeV leave a total description, such as QED, for these interactions far in the future. In this section we will be studying essentially the strong interaction. The weak interaction accounts for processes which break the nice symmetries of the strong interactions but with cross sections too small for our detector to measure. Since QED is so well understood, cuts can be made on the data to eliminate most QED events, and the residuals can be calculated. This leaves us with a large body of hadronic or strong interaction data.

A. Determining the Detected Cross Section

The primary sources of QED events which must be eliminated from the hadronic data are Bhabha and mu-pair events, shown in Fig. 11. Since the electron and positron collide with equal and opposite momenta, the produced particles in such events must also have equal and opposite momenta, making these events very distinctive. The final momenta may appear slightly unequal due to measurement errors, multiple scattering, or the radiation of a photon by one of the particles. To eliminate these events the hadronic events are required to satisfy

BHABHA AND MU-MU EVENTS

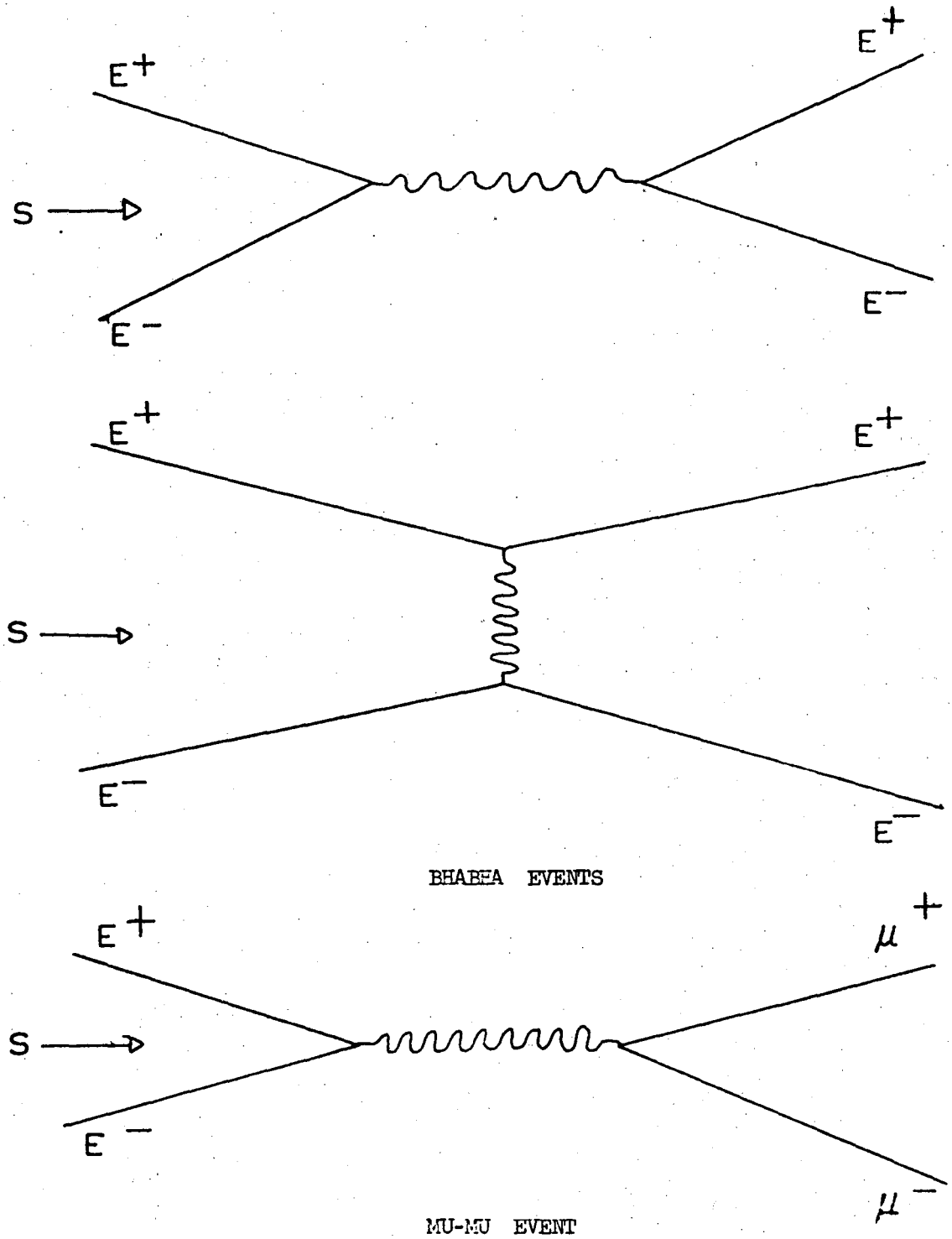

XBL 756-1722

Figure 11

1) 3 or more prong events may not contain two tracks collinear to within 10° and with large shower counter pulse heights;

2) 2-prong events must have a coplanarity angle between 20° and 160°. The coplanarity angle is the angle between the plane formed by one final state particle and the beam axis, and the plane formed by the other final state particle and the beam axis.

Another source of QED events which can contaminate the hadrons is the two-photon process shown in Fig. 12. This process is the subject of section V. Typically only the particles indicated will be detected, the others escaping down the beam pipe. This can be viewed as a "double-bremsstrahlung" process, where the photon propagators tend to make the detected particles have low momentum and be coplanar. Cut 2) on the 2-prong hadrons is not sufficient to eliminate "two photon" events. The following additional cut is made:

3) 2-prong events must have momenta of each prong greater than 300 MeV/c.

The residual two-photon cross section is calculated in section V (less than 6% of the detected hadron yield) and is figured into the systematic error on the hadronic cross section.

The remaining events comprise the hadronic data. Gas scatter background is subtracted as described in section II. From these data, the cross section for hadronic events detected by our detector can be computed using the Bhabhas for a luminosity normalization. The important quantity to measure, of course, is the total cross

0 0 0 0 4 4 0 2 7 1 5

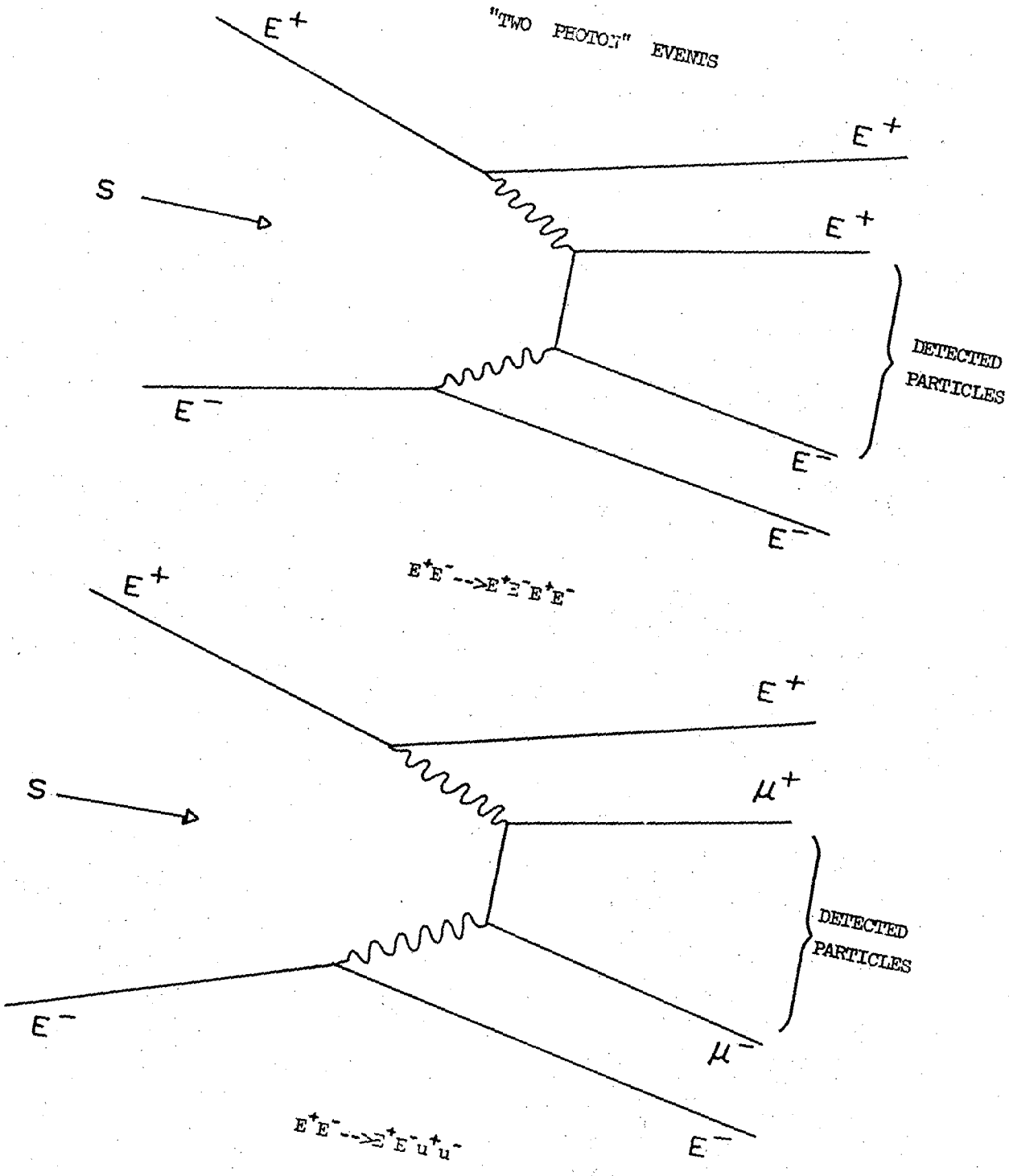

XBL 756-1723

Figure 12

section for $e^+e^- \rightarrow$ hadrons, not just the part measured by our detector. The "detected" cross section must be unfolded to give the total or "produced" cross section.

B. Unfolding the Cross Section

Determining the "produced" cross section from the "detected" cross section is a crucial and potentially dangerous step and deserves a careful explanation. Our method has been a two-step procedure. First a complete Monte Carlo simulation of the detector was constructed including the inefficiencies due to the fraction of the full solid angle covered by the detector and the inefficiency of the shower counters for detecting charged particles which pass through them. A model was used for the "produced" hadronic cross section, and various parameters were adjusted to make the "detected" cross section, coming from the Monte Carlo, fit the data. From this first step alone, one might infer that the produced cross section, as adjusted, was the true hadronic cross section. This method, however, would be highly model-dependent. Instead, this first step was used only to determine a "produced-detected" matrix Qmn, the probabilities that a produced event with n charged prongs would be detected with m charged prongs in the detector. Then using the data D_m, the number of events with m detected prongs, the m equations

$$D_m = \sum_{n=2}^{\infty} Q_{mn} P_n$$

were solved to find P_n, the number of events with n produced prongs.

The total number of produced events

$$\sum_{n=2}^{\infty} p_n$$

found by this method is an improvement in accuracy over the one-step method and is fairly model-independent.

We now describe the first step in detail. The simplest model for the detector is one in which the probability of detecting any one prong is independent of its momentum and the momentum and direction of the other prongs in the event. This probability, $\varepsilon = .47$, would account for shower counter inefficiencies and the possibility of missing the detector. Since two prongs must be detected to trigger the detector, the probability of detecting an event with two produced prongs would be ε^2. In general the probability of detecting an event with n produced prongs would be:

$$P(n) = 1 - (1 - \varepsilon)^n - n\varepsilon(1 - \varepsilon)^{n-1}.$$

In terms of this simple model, the produced-detected matrix is

$$Q_m = \frac{n!}{m!(n - m)!}\varepsilon^m(1 - \varepsilon)^{n-m}.$$

A more accurate model is complicated only by the following:

1) The shower counter efficiency and hence ε is momentum-dependent.

2) For most models, the momentum and direction of one prong depends on those of the others.

3) Possibilities of photon pair production, multiple scattering, QED contamination, etc. must be included in the model. The method,

however, is the same. A model is used to predict the prong momenta and the prong-to-prong angular correlations. Many events are generated and the matrix Q_{mn} is determined.

The most useful model, the all-pion model, predicts only pions produced with a phase space distribution. The only parameters to be adjusted in this model are the mean number of charged particles detected and their mean momentum assuming Poisson distributions. The total number of pions produced is made to follow a Poisson distribution. Other models tested are the heavy particle model, which allows for kaons and nucleons, and a jet model which inserts a matrix element

$$|M|^2 \propto e^{-\Sigma p_i^{\,2}/R}$$

where p_i is the momentum transverse to a jet axis and R is adjusted to make $p_i \approx 350$ MeV/c.

Using the Q_{mn} and the data D_m, the overdetermined set of m equations

$$D_m = \sum_{n=2}^{\infty} Q_{mn} P_n$$

are solved for P_n using a maximum likelihood mathod. The final result is the ratio of the detected hadronic cross section to the produced

$$\bar{\varepsilon} = \frac{\sigma_{\text{detected}}}{\sigma_{\text{produced}}} = \frac{\sum_{m=2}^{\infty} D_m}{\sum_{n=2}^{\infty} P_n}$$

Here the produced cross section does not include all neutral states.

The variation in $\bar{\varepsilon}$ using the three different models is less than 5%. This efficiency is shown in Fig. 13. Figs. 14 and 15 show how well the data is reproduced using just step one of the procedure (Monte Carlo) and both steps (unfold). Using $\bar{\varepsilon}$ from Fig. 13 $\sigma_{produced}$ may now be calculated from

$$\sigma_{produced} = \frac{\sigma_{detected}}{\bar{\varepsilon}}$$

C. Measured Cross Sections

The total measured cross sections have been reported in reference 1 and a detailed description of the detector and analysis programs in reference 14. Fig. 16 shows σ_T(produced) as a function of center-of-mass energy W and $R = \sigma_T/\sigma_{\mu\mu}$ where $\sigma_{\mu\mu}$ is the cross section for $e^+e^- \rightarrow \mu^+\mu^-$.

The most outstanding features of this data are the narrow resonances at W = 3.1 GeV and W = 3.7 GeV and the possible broad resonance or threshold at W = 4.1 GeV. A detail of these resonances is shown in Figs. 17 and 18.

D. The Narrow Resonances

In the early SPEAR data inconsistencies were found in the value determined for σ detected from hadrons at 3.1 GeV, a standard data point. The value of the cross section from one run to the next differed by as much as several standard deviations. A careful energy

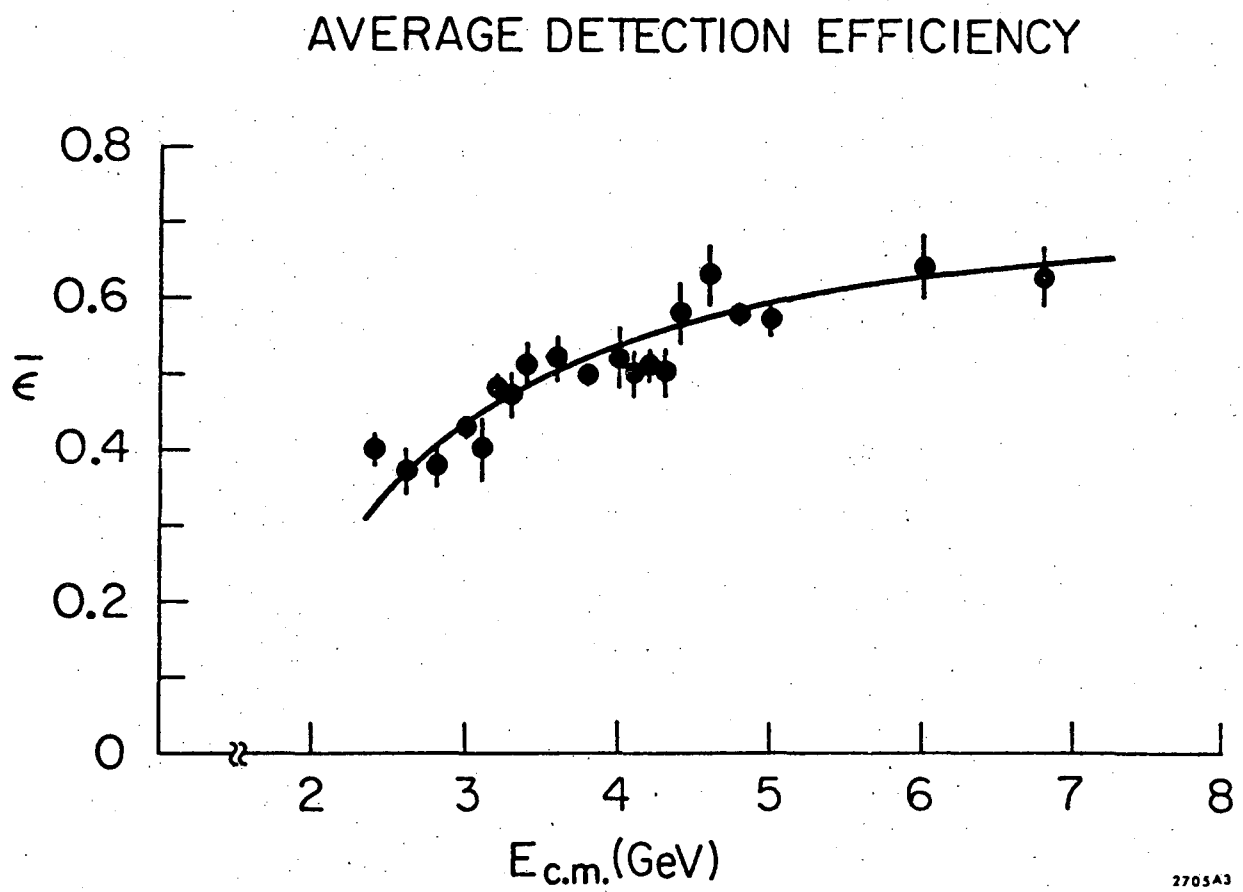
AVERAGE DETECTION EFFICIENCY
0.8
0.6
0.4
0.2
0
$\bar{\epsilon}$
2
3
4
5
6
7
8
$E_{c.m.}$(GeV)
2705A3

Figure 13

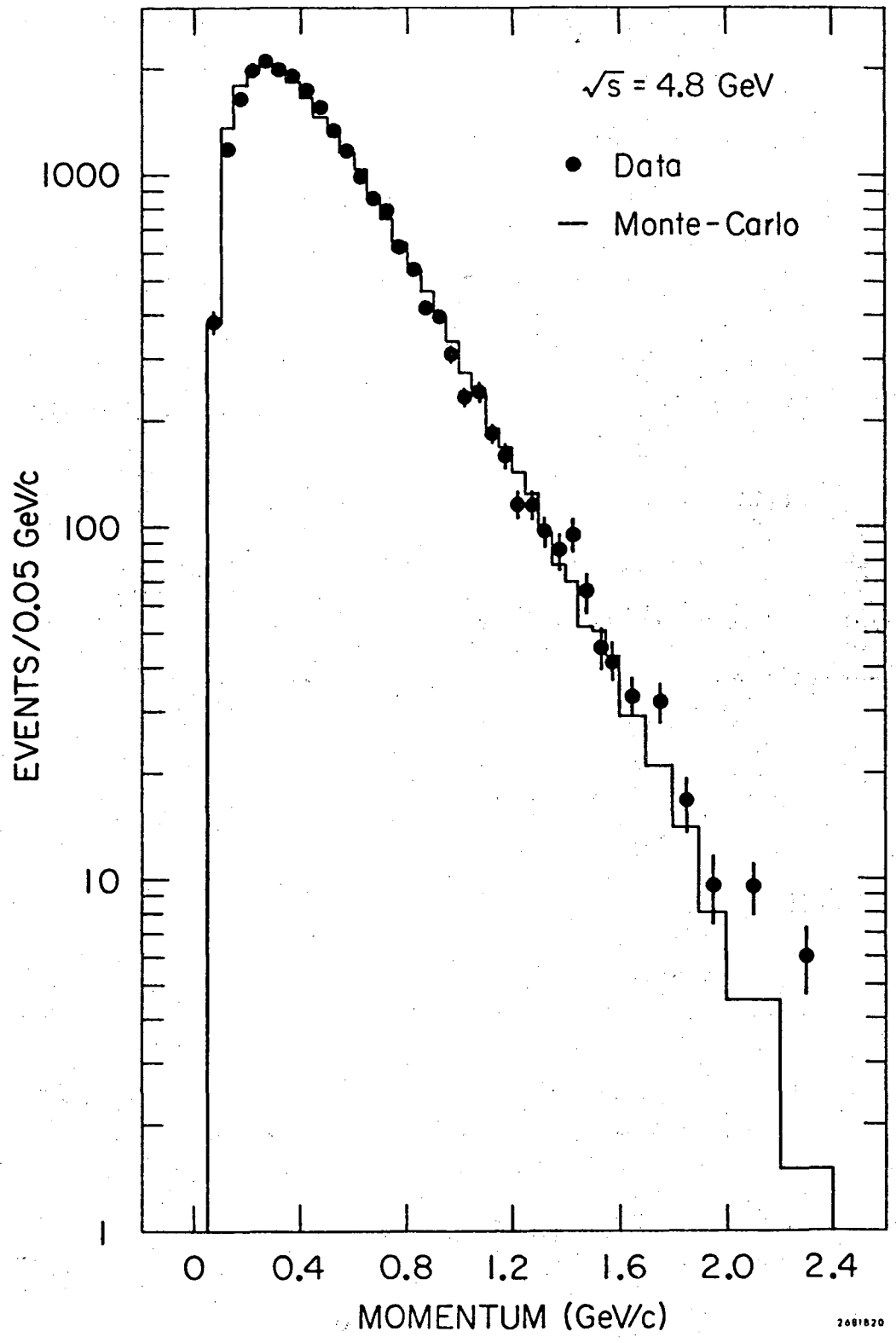
√s = 4.8 GeV
Data
Monte-Carlo
1000
100
10
1
EVENTS/0.05 GeV/c
0
0.4
0.8
1.2
1.6
2.0
2.4
MOMENTUM (GeV/c)
2681820

Figure 14

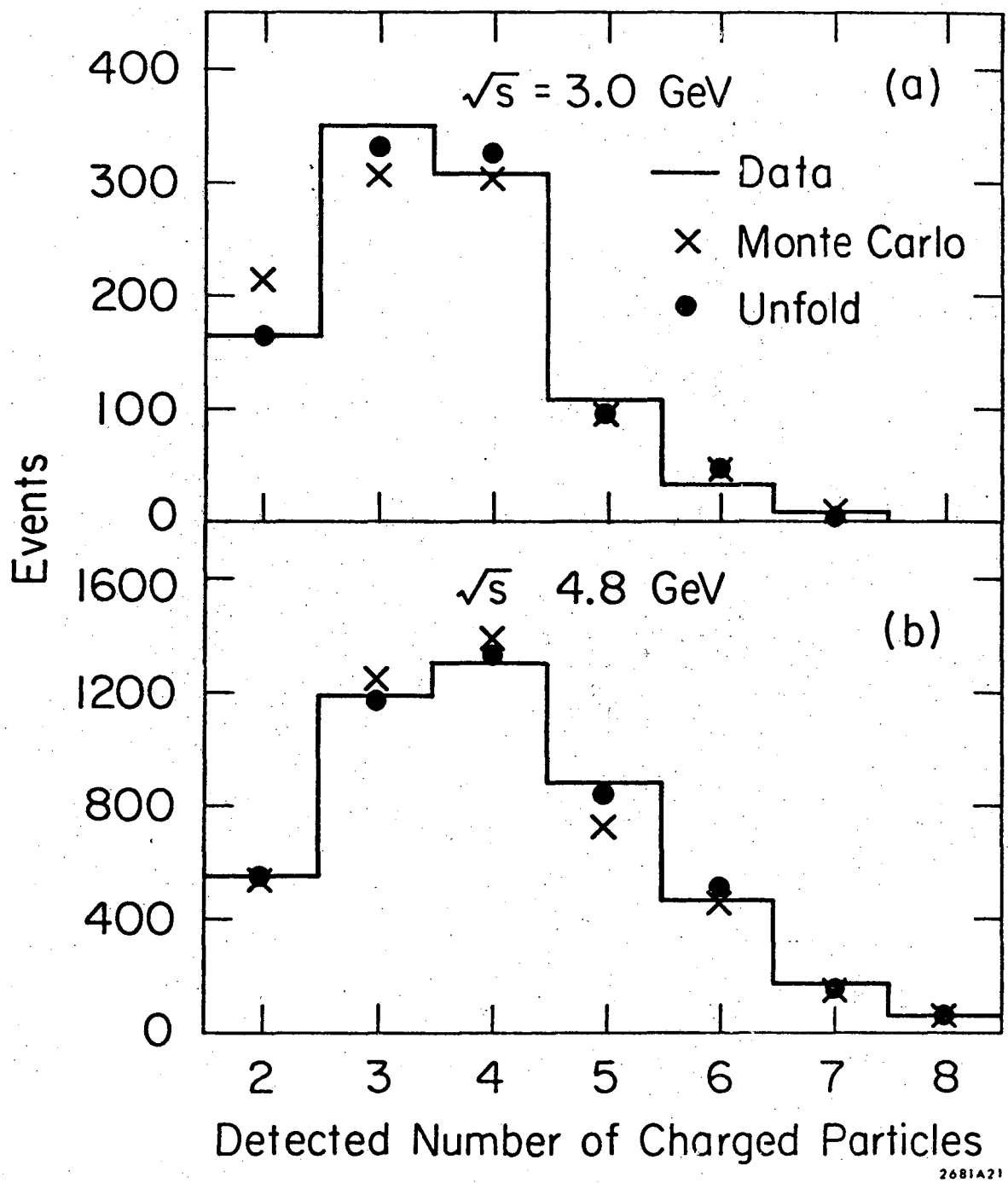
400
300
200
100
0
Events
√s = 3.0 GeV
(a)
Data
Monte Carlo
Unfold
1600
1200
800
400
0
√s 4.8 GeV
(b)
2
3
4
5
6
7
8
Detected Number of Charged Particles
2681A21

Figure 15

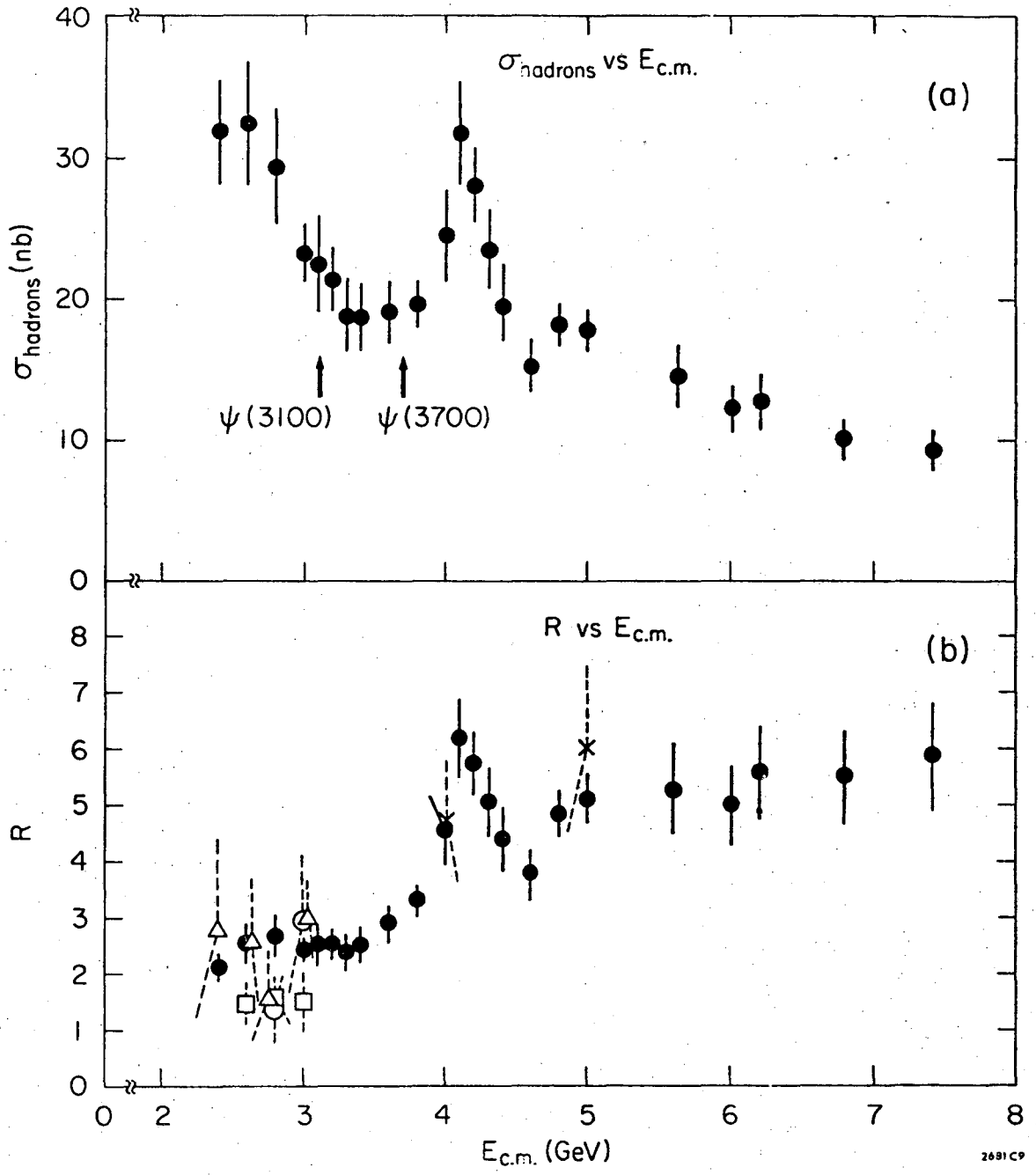
σhadrons vs Ec.m.
(a)
σhadrons (nb)
ψ(3100)
ψ(3700)
R vs Ec.m.
(b)
R
Ec.m. (GeV)
2691C9

Figure 16

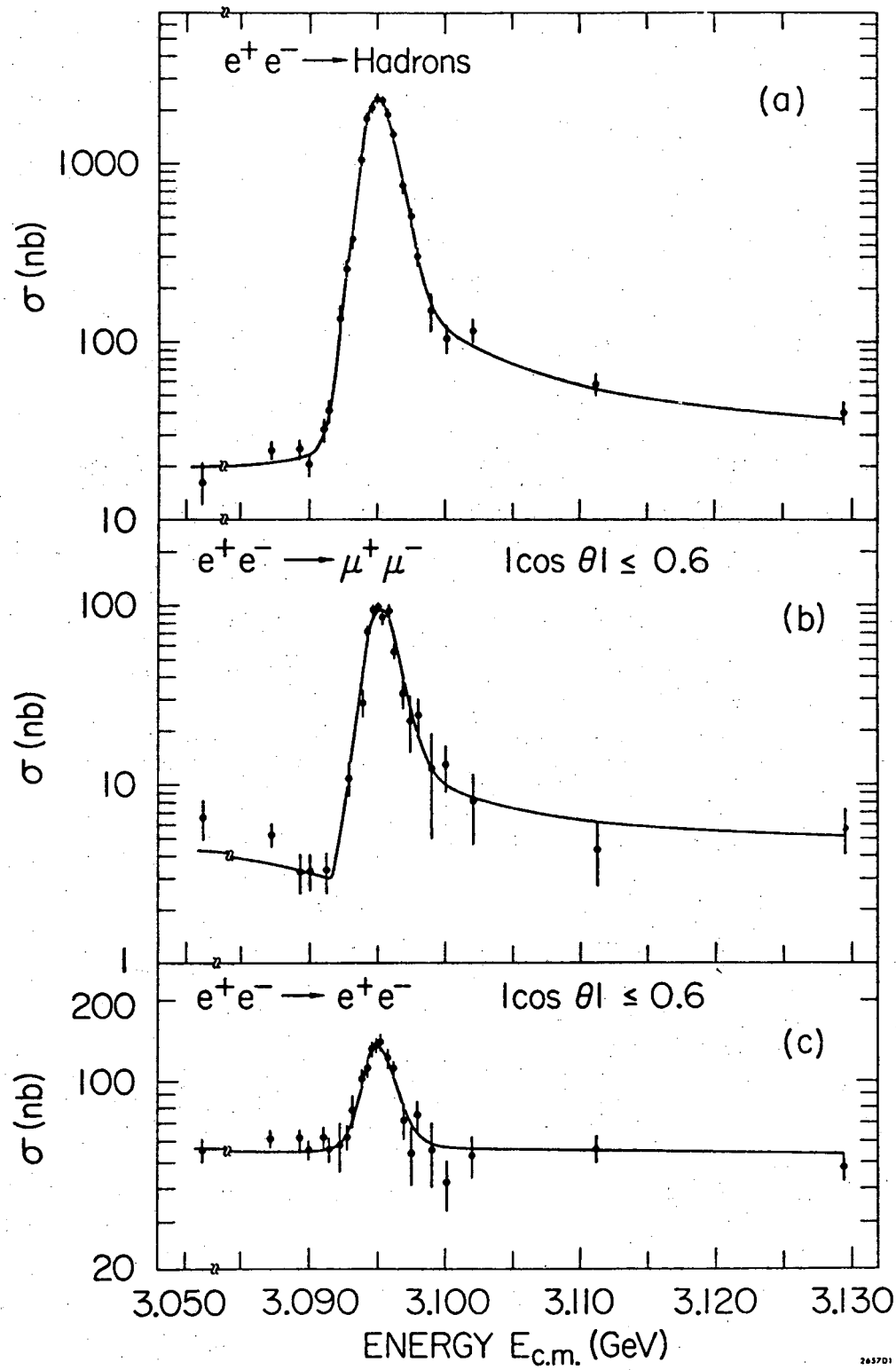
e+ e− → Hadrons
(a)
1000
100
10
σ (nb)
e+e− → μ+μ−
|cos θ| ≤ 0.6
(b)
100
10
1
σ (nb)
e+e− → e+e−
|cos θ| ≤ 0.6
(c)
200
100
20
σ (nb)
3.050
3.090
3.100
3.110
3.120
3.130
ENERGY Ec.m. (GeV)

Figure 17

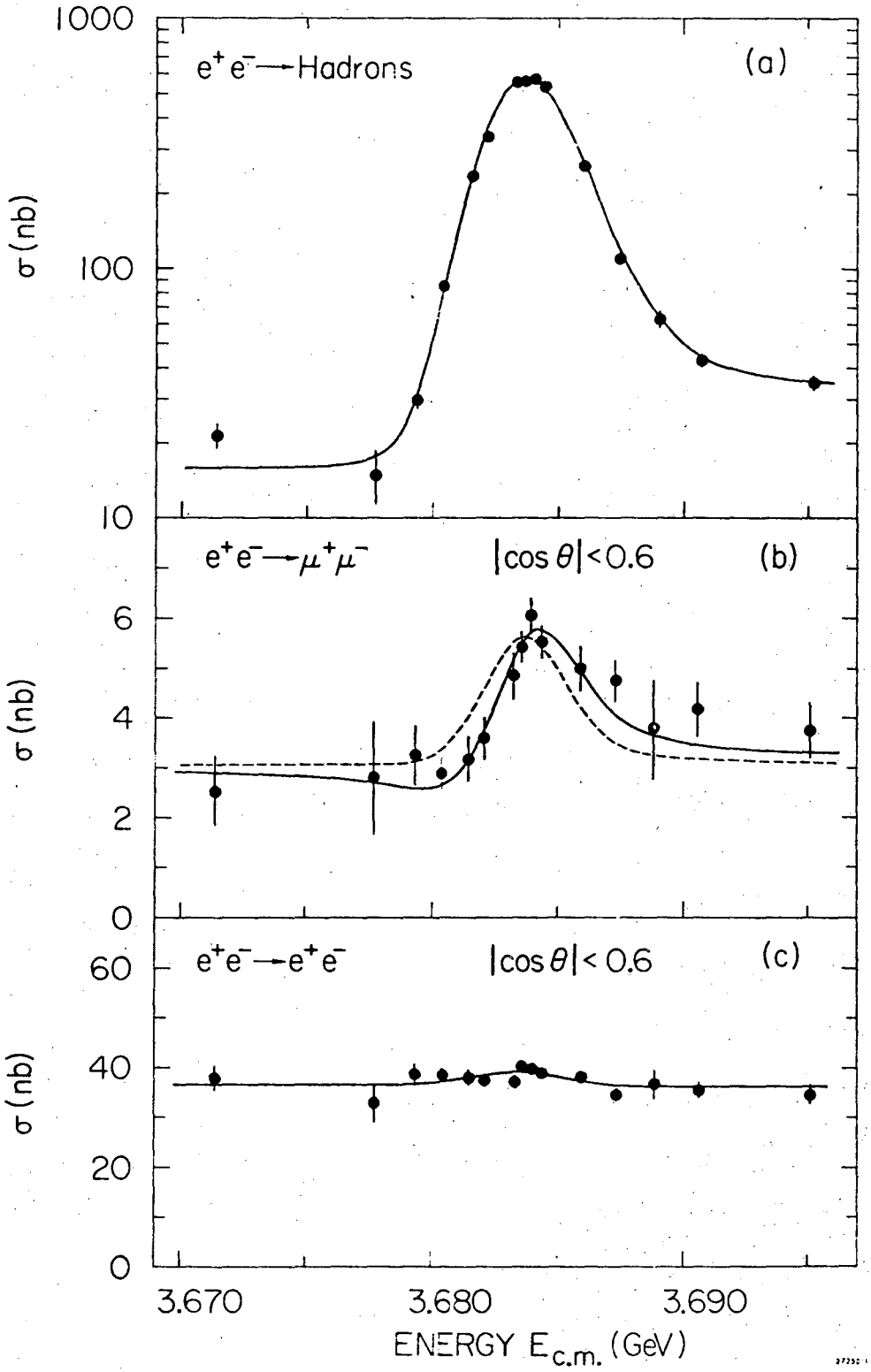
1000
100
10
σ (nb)
e⁺e⁻→Hadrons
(a)
e⁺e⁻→μ⁺μ⁻
|cos θ|<0.6
(b)
6
4
2
0
σ (nb)
e⁺e⁻→e⁺e⁻
|cos θ|< 0.6
(c)
60
40
20
0
σ (nb)
3.670
3.680
3.690
ENERGY E c.m. (GeV)

Figure 18

scan was done in that region, and in November of 1974 a very remarkable resonance was found, the $\psi(3095)$. Fig.17 shows σ vs W. The resonant cross section for hadrons was 100 times the background and only 2.5 MeV wide. This explained the previous run-to-run fluctuations; some runs were closer to the resonant energy than others.

Soon the $\psi(3684)$ was found and these surprisingly narrow resonances became the central focus of strong interaction theory. Their discovery is reported in references 2 and 3, and more detailed properties in 6 and 7. Table 1 shows their masses and widths. Several theories were constructed to explain the existence of these resonant particles, but most remain to be tested. The most interesting additional piece of information the detector data has provided is that the $\psi(3684)$ decays to the $\psi(3095)$, 0.57 ± 0.08 of the time, and via the reaction

$$\psi(3684) \rightarrow \psi(3095) + \pi^+ + \pi^-$$

0.32 ± 0.04 of the time (see reference 5). From this information one can infer that the ψ particles interact with each other through the strong interaction rather than the weak.

A complete search was done for other resonances in the energy range 3.2 to 5.9 GeV, Fig. 19, and no evidence was found for further structure (see reference 4). These resonances are, of course, the focus of a great deal of interest, and much has already been published by the SLAC-LBL collaboration concerning them. In particular, a good summary of the resonance results can be found in reference 15. Also a review article on electron positron hadronic physics is found in reference 16.

0 0 0 0 4 4 0 2 7 2 1

Properties Of The ψ Particles

	ψ (3095)	ψ (3684)
Mass	3095±4 MeV	3684±5 MeV
Γ_e (width to electrons)	4.8±0.4 KeV	2.1±0.3 KeV
Γ (full width)	69±10 KeV	228±56 KeV
$\int \sigma_{hadron}(W)dW$	10.8±2.7 nb-GeV	3.7±0.9 nb-GeV

Table 1

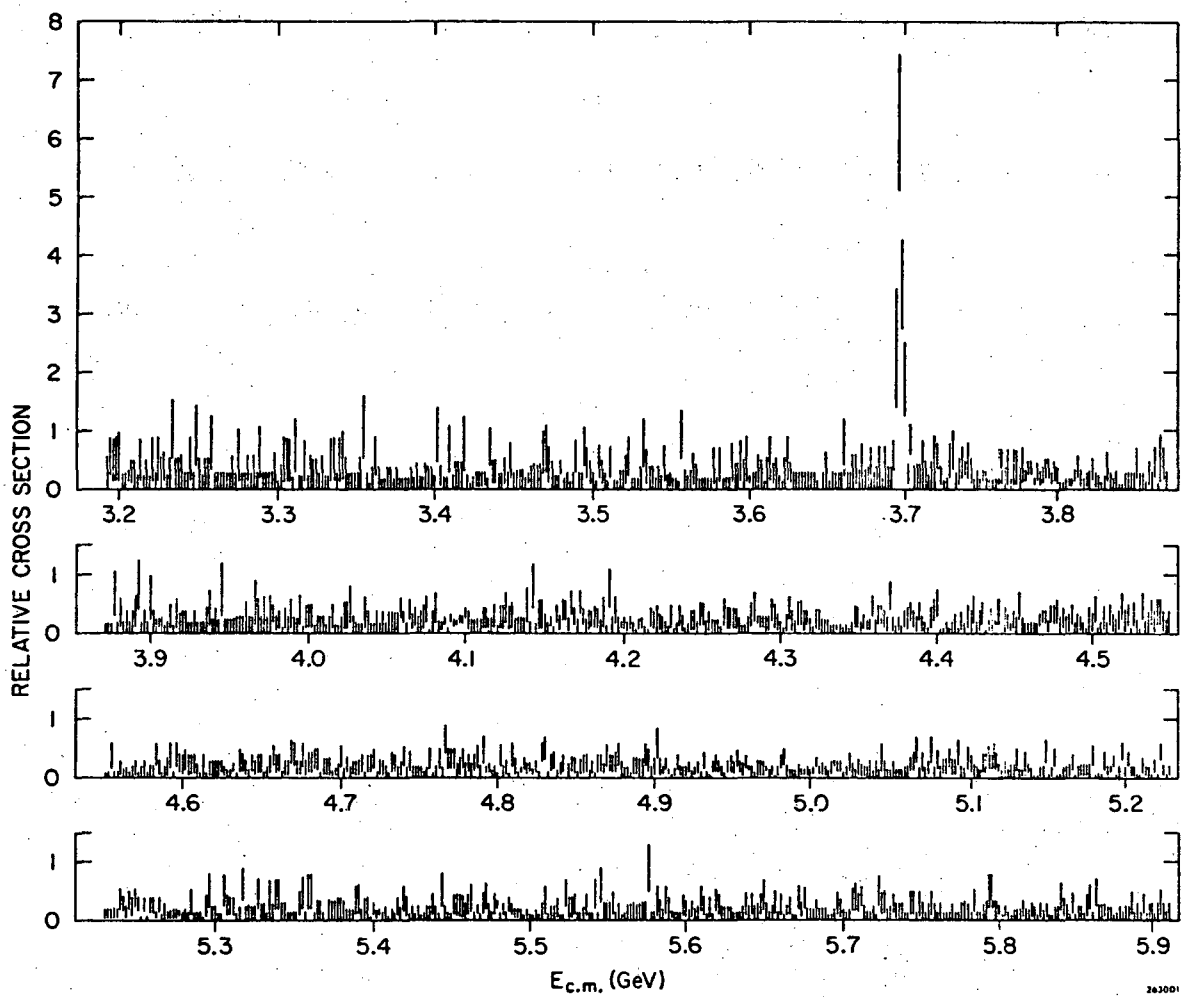
RELATIVE CROSS SECTION
8
7
6
5
4
3
2
1
0
3.2
3.3
3.4
3.5
3.6
3.7
3.8
3.9
4.0
4.1
4.2
4.3
4.4
4.5
4.6
4.7
4.8
4.9
5.0
5.1
5.2
5.3
5.4
5.5
5.6
5.7
5.8
5.9
$E_{c.m.}$ (GeV)

Figure 19

E. Present and Future Studies

Much work is presently being done with the magnetic detector at SPEAR to uncover further information on the strong interaction. Concerning the resonances, the search for further resonances will hopefully be extended to 8 GeV, and the decay modes of the $\psi(3095)$ and $\psi(3684)$ are being carefully analyzed to determine more about their properties. A popular theory of the particles is that they are composed of "charmed quarks," previously unseen. Several types of searches are being done for other kinds of "charmed" matter.[8] Other studies with the detector include a search for hadronic jet structure, an understanding of the unseen neutral particles, and a search for heavy leptons.

IV. Second and Third Order QED Cross Sections and the Radiative Corrections

In this section we will begin the study of quantum electrodynamics at SPEAR by studying the lowest order cross sections, $e^+e^- \rightarrow e^+e^-$ and $e^+e^- \rightarrow \mu^+\mu^-$, and comparing the predictions of QED to our data. These processes, second order in α, cannot be measured accurately without also accounting for processes which are third order in α. This includes calculating the cross sections for the above processes to third order in α as well as including the radiative corrections, the cross sections for $e^+e^- \rightarrow e^+e^-\gamma$ and $e^+e^- \rightarrow \mu^+\mu^-\gamma$ where the photon is of low enough energy that its presence goes undetected. Fourth order cross sections are generally small enough that they need not be considered; however the remarkable two-photon process has been shown to be comparable to second order processes. Fortunately these events are fairly distinctive and can be separated from those of other processes. The two-photon events are the subject of section V.

The aims of this section are twofold. First we will apply the most stringent test to quantum electrodynamics that has been done to date. Values for cutoff parameters in QED breakdown models will be determined which are significantly higher than the previously highest values. Although the determination of these cutoff parameters was done by the SLAC-LBL collaboration as a whole, rather that by the author individually, the results are presented here because they are crucial to the understanding of the second and third order QED events. Second we will demonstrate that our event classification scheme successfully separates hadronic events from QED events. This will be done by

showing an excellent fit of predicted to detected QED event distributions with various momentum cutoffs. The remaining events, not classified as QED events (or two-photon events as in section V) are then confidently called hadronic events and analyzed as described in section III.

A. Calculation of the Cross Sections

The calculation of Bhabha and mu-pair cross sections to third order has been carried out exactly by Berends, Gaemers, and Gastmans,[9,10,11] and we are grateful to them for supplying the SPEAR collaboration with their computer programs. The calculations are complete and exact to third order in α, and have been used exclusively to determine Bhabha and mu-pair cross sections. We will outline briefly here what is included in these cross sections and then use them for comparison with data.

We begin with the easier of the two cross sections, $e^+e^- \to \mu^+\mu^-$. the cross section to second order is well known to be:

$$\frac{d\sigma^\circ}{d\Omega} = \frac{\alpha^2}{2S}\left(\frac{\frac{1}{4}S - M_\mu^2}{\frac{1}{4}S - M_e^2}\right)^{1/2}\left(\frac{1}{2} + \frac{2(M_e^2 + M_\mu^2)}{S} - 2\cos^2(\theta)\ \frac{1}{4} + \frac{M_e^2 + M_\mu^2}{S} - \frac{4M_e{}^2M_\mu^2}{S^2}\right)$$

where $d\Omega$ and θ refer to the positively charged muon. This is for diagram a of Fig. 20.

To calculate the cross section to third order, two types of terms must be added. The first type is interference terms between the second order diagram a and the fourth order diagrams b, c, and d of Fig. 20. The result of such interference terms will, of course, be third order.

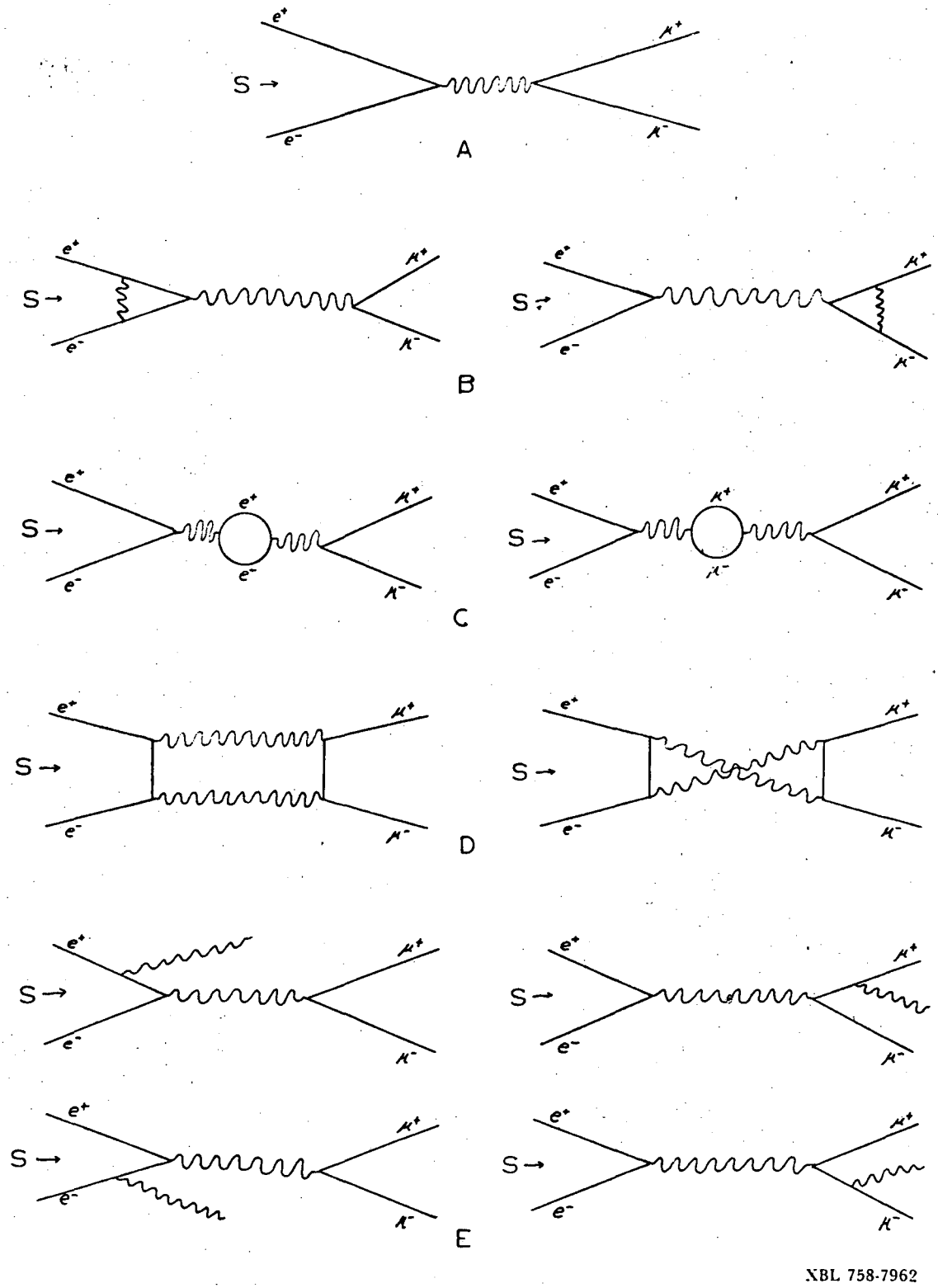

Figure 20

Interference of a with b, the vertex correction, will be divergent but the divergent term will be cancelled by the infra-red divergence of diagrams e.

The other third order terms are those for diagrams e including interference among themselves. This is the more difficult part of the calculation, for an integration must be done over the final state variables of the photon. The expression becomes very simple if one assumes that the photon momentum can be neglected and the muon momenta are unaltered by the emission of the photon. The approximation is good when the photons are sufficiently soft and hence is called the "soft photon" approximation. The approximation, however, is not adequate when angular distributions good to an accuracy of a few percent are needed. The calculation is therefore done exactly in the following way: for the integration region chosen, the maximal isotropic region in photon momentum is found. The soft photon approximation is used in this region to obtain an analytic expression, part of which will cancel the divergent term coming from the vertex correction diagram. The residual integral, exact minus soft photon, is then calculated numerically in the isotropic region I and the exact expression is calculated for the remaining anistropic region AI.

The expression derived for the third order cross section is the following:

$$\frac{d\sigma}{d\Omega} = \frac{d\sigma^{o}}{d\Omega}\{1+\delta_{VC}+\delta_{VP}+\delta_{TP}+\delta_{S}\} + \frac{d\sigma^{mag}}{d\Omega} +$$

$$\int_{AI} \frac{d^5\sigma^B}{d\Omega\, d\Omega_\gamma\, dE_\gamma}\, d\Omega_\gamma\, dE_\gamma + \int_{I} \frac{d^5(\sigma^B-\sigma^S)}{d\Omega\, d\Omega_\gamma\, dE_\gamma}\, d\Omega_\gamma\, dE_\gamma$$

Here $d\sigma^\circ/d\Omega$ is the second order cross section, a in Fig. 20 $d\sigma^\circ/d\Omega\ \delta_{VC} + d\sigma^{mag}/d\Omega$ is the vertex correction term b; $d\sigma^\circ/d\Omega\ \delta_{VP}$ is the vacuum polarization term c; $d\sigma^\circ/d\Omega\ \delta_{TP}$ is the two-photon term d; $d\sigma^\circ/d\Omega\ \delta_s$ is the "soft photon" approximation to terms e, taken over the maximum isotropic sub-region of the total region of integration. All of these terms are analytic; the last two terms must be integrated numerically. σ^B refers to the exact bremsstrahlung cross section for terms e, and σ^s refers to the "soft photon" approximation. The previous expression is also simply written:

$$\frac{d\sigma}{d\Omega} = \frac{d\sigma^o}{d\Omega}\ (\ 1 + \delta_A + \delta_N\ ) = \frac{d\sigma^o}{d\Omega}\ (\ 1 + \delta_T)$$

where δ_A refers to the analytic terms and δ_N to the numerically integrated terms. δ_T represents the total third order correction to the second order calculation.

Two particular types of integration regions have been programmed by Berends et al. The first requires the muons to be collinear to within some threshold η, and to have energy above some threshold E_{min}. This region was used with tight constants, $\eta = 10°$ and $E_{min} = 1/2$ (beam energy), to test quantum electrodynamics and determine breakdown parameters. The other type of region required a specific degree of acoplanarity between two muons, and energy above a threshold E_{min}. The acoplanarity angle, ψ, is π minus the angle between the two final state momenta projected onto the plane perpendicular to the incident particles. For this region the cross section is expressed as:

$$\frac{d\sigma}{d\psi} = \frac{d\sigma^{\circ}}{d\psi}(1 + \delta_A) + \int_{AI} \frac{d^5\sigma^B}{d\Omega_{\mu^+}d\Omega_{\mu^-}dE_{\mu^-}} d\Omega_{\mu^+}d\cos\theta_{\mu^-}dE_{\mu^-}$$

$$+ \int_{I} \frac{d^5(\sigma^B - \sigma^S)}{d\Omega_{\mu^+}d\Omega_{\mu^-}dE_{\mu^-}} d\Omega_{\mu^+}d\cos\theta_{\mu^-}dE_{\mu^-}$$

rather than $d\sigma/d\Omega$. An integration of this type will be used for comparison with a coplanarity distribution of all observed QED events with final state momenta above some threshold,

The calculation for Bhabha events $e^+e^- \rightarrow e^+e^-$ is similar to that for mu pairs. It is complicated only by the addition of the spacelike photon diagrams shown in Fig. 21. Here the second order cross section must include diagrams a from both Figs. 20 and 21 as well as the interference term between them. Vertex correction terms must include diagrams b from both figures, vacuum polarization terms must include diagrams c from both, etc. Otherwise, the calculation is the same and has been done in the same way as for muons.

B. Test of Quantum Electrodynamics

Results of the stringent test applied to quantum electrodynamics using the magnetic detector comprised the first publication of the SLAC-LBL collaboration.[17] The test parameterized QED breakdown models in terms of cutoff parameters and established values considerably larger than previously highest values established by Beron et al.,[18] also at SPEAR. Rigorous tests of QED are crucial since deviations from the QED cross section for $e^+e^- \rightarrow e^+e^-$ must ultimately be found at sufficiently large momentum transfer to preserve unitarity. The

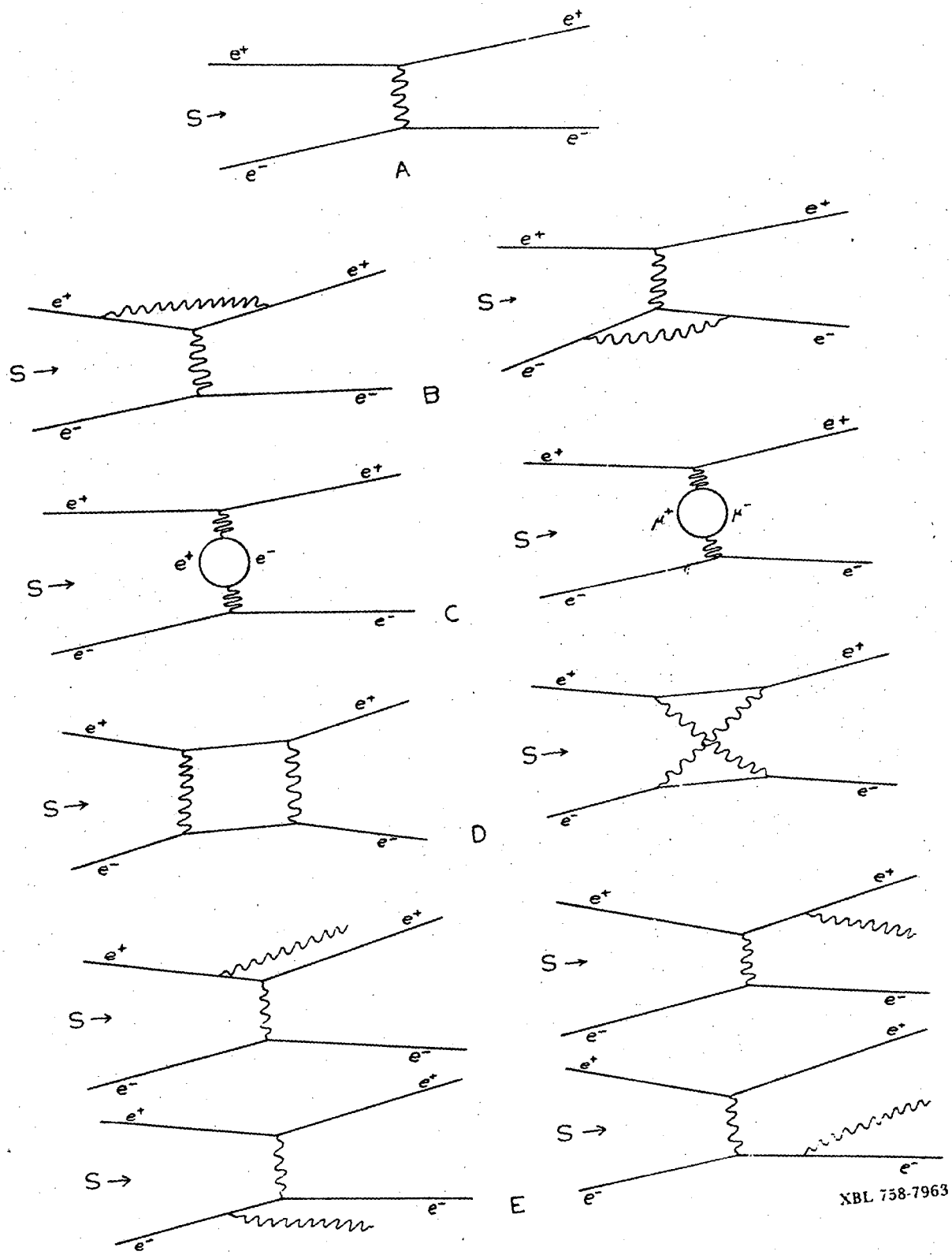

Figure 21

test involved selecting a clean sample of events of the types $e^+e^- \to e^+e^-$ and $e^+e^- \to \mu^+\mu^-$ and fitting them to cross sections containing breakdown parameters. Radiative corrections are included to third order in α.

The sample of events consisted of all two-prong events with opposite charges which originated from an interaction region fiducial volume of 4 cm radius and 80 cm length. The two tracks were required to have equal trigger counter times-of-flight to within 3 ns, to be collinear to within 10°, and to have momentum $p \geq E\ cm/4$. These last two cuts eliminated $e^+e^- \to e^+e^-$ and $e^+e^- \to \mu^+\mu^-$ events which radiated very strongly and suppressed $e^+e^- \to e^+e^-A^+A^-$ events where A is any particle.

The $e^+e^- \to e^+e^-$ and $e^+e^- \to \mu^+\mu^-$ events were separated using their shower counter pulse heights. Fig.[22] is a histogram of the sum of pulse heights for the two tracks for the sample of events at Ecm = 4.8 GeV. As can be seen, there is a clear separation of the mu-pair events with low pulse heights from the Bhabha events with larger pulse heights. A single cut was made at pulse height 70 to separate the two.

Although hadron events, such as $e^+e^- \to \pi^+\pi^-$, could appear in the mu-pair sample, a study of the muon spark chamber information showed no significant contamination from this source. The only significant hardware correction came from the shower counter efficiency on mu-pairs, which was 94% to 98% depending on θ. No background subtraction was necessary as no QED candidates were seen in non-colliding beam runs which comprised about 10% of the running.

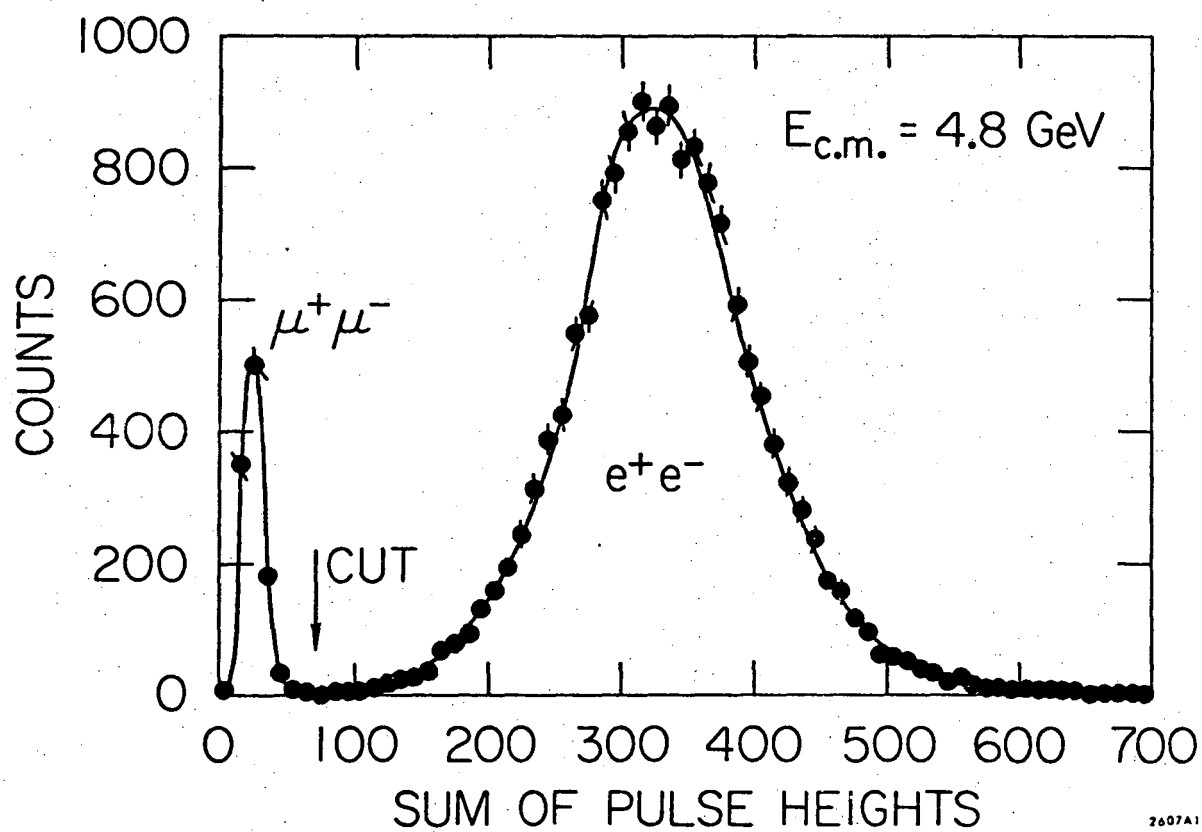
1000
800
600
400
200
0
COUNTS
$E_{c.m.}$ = 4.8 GeV
$\mu^+\mu^-$
e^+e^-
CUT
0
100
200
300
400
500
600
700
SUM OF PULSE HEIGHTS
2607A1

Figure 22

The events for the two samples were binned in cos(θ) and the distributions compared to third order calculations. Fig. 23 shows the normalized fit to QED and QED with the detector acceptance folded in.

To establish the validity of QED, one modifies the photon propagator:

$$\frac{1}{Q^2} \rightarrow \frac{1}{Q^2} F(Q^2)$$

where the most general form for $F(Q^2)$ to first order in Q^2 is

$$F(Q^2) = 1 + f\, Q^2.$$

One then attempts to prove that f is very small. Specific modified photon propagator models postulate $F(Q^2)$ to be

$$F_+(Q\ ) = \left(1 - \frac{Q}{\Lambda_+^2}\right)^{-1} \simeq 1 + \frac{Q^2}{\Lambda_+^2}$$

or

$$F_-(Q^2) = \left(1 + \frac{Q^2}{\Lambda_-^2}\right)^{-1} \simeq 1 - \frac{Q^2}{\Lambda_-^2}$$

for positive or negative metric models[19,20]. For each of our fits we will first determine f and its error and then separately equate f to $(\Lambda_+)^{-2}$ and $-(\Lambda_-)^{-2}$ in order to derive 95% confidence level lower limits for Λ_+ and Λ_-. Proving Λ_+ and Λ_- large is, of course, equivalent to proving f small. Note that to first order in Q^2, this method effectively tests every conceivable model for QED breakdown.

The third order radiative correction is determined as a single quantity $\delta_T(\theta)$ such that

$$\frac{d\sigma}{d\Omega} = \frac{d\sigma^\circ}{d\Omega}\ (1+\delta_T(\theta)\ )$$

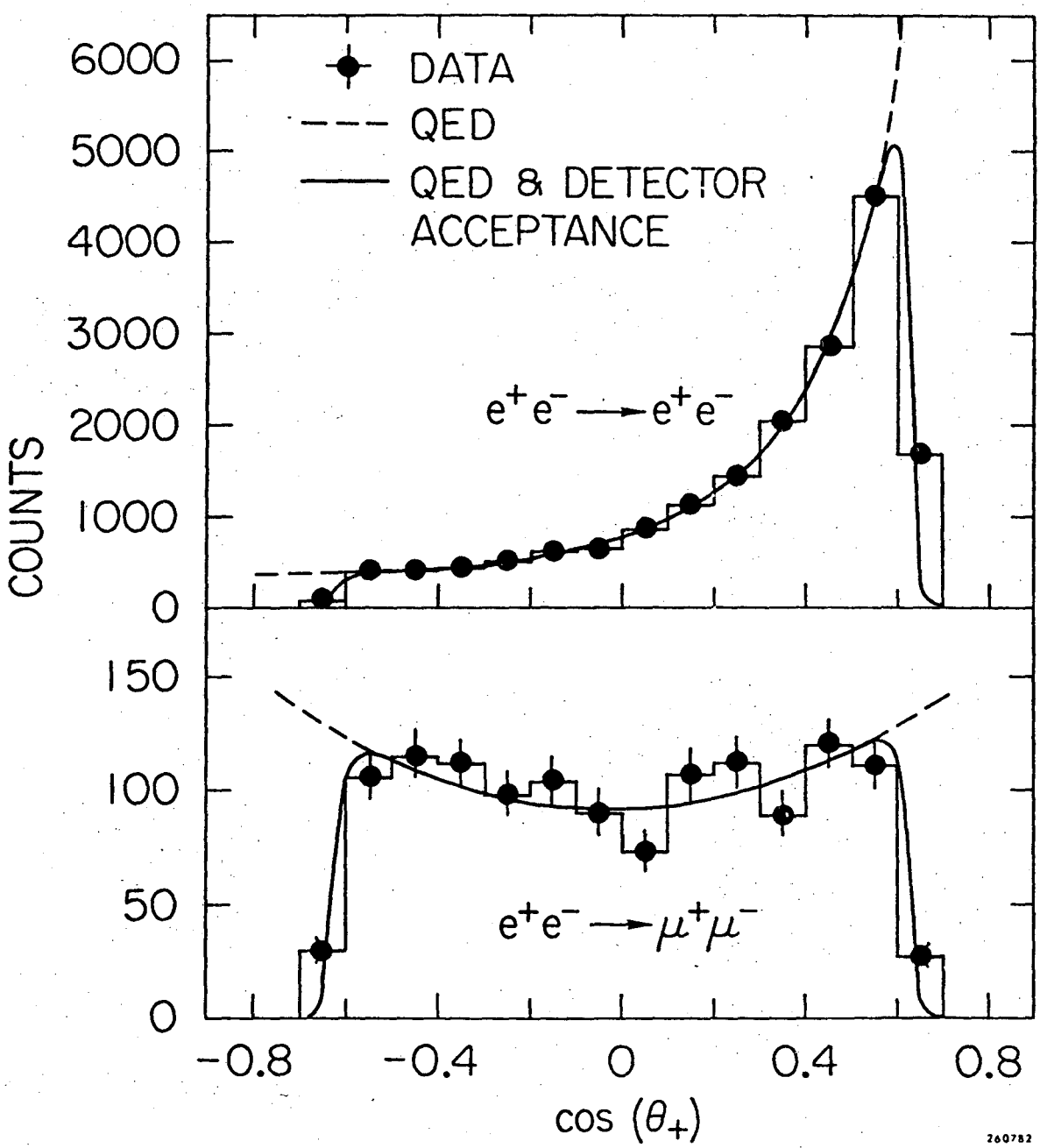
DATA
QED
QED & DETECTOR ACCEPTANCE
$e^+e^- \rightarrow e^+e^-$
$e^+e^- \rightarrow \mu^+\mu^-$
COUNTS
6000
5000
4000
3000
2000
1000
0
150
100
50
0
−0.8
−0.4
0
0.4
0.8
cos (θ_+)
260782

Figure 23

so in the following we will include it by multiplying our modified cross sections by $(1 + \delta_T)$. In the case of separate spacelike and timelike form factors, the corrections could be computed separately for the spacelike, timelike, and interference terms, but we will assume that the errors due to using the single factor $(1 + \delta_T)$ are the next order smaller in α.

The cross sections for $e^+e^- \to e^+e^-$ and $e^+e^- \to \mu^+\mu^-$ are (setting $M_e = 0$):

$$\frac{d\sigma_{ee}}{d\Omega} = \frac{\alpha^2}{2s}\left(\frac{s^2+u^2}{t^2} + \frac{2u^2}{st} + \frac{t^2+u^2}{s^2}\right)(1 + \delta_T^{ee})$$

$$\frac{d\sigma_{\mu\mu}}{d\Omega} = \frac{\alpha^2}{2s}\beta\left(\frac{t^2+u^2}{s^2} + (1-\beta^2)\frac{2tu}{s^2}\right)(1 + \delta_T^{\mu\mu})$$

where

$$\beta \quad |\vec{p}_{\mu^+}|/E_{\mu^+}$$

and s, t, u, are the Mandelstam variables:

$$s = (p_{e^+} + p_{e^-})^2 = (p_{\mu^+} + p_{\mu^-})^2$$

$$t = (p_{e^+} - p_{\mu^-})^2 = (p_{e^-} - p_{\mu^-})^2 \simeq -s\sin^2\frac{\theta_{\mu^+}}{2}$$

$$u = (p_{e^+} - p_{\mu^-})^2 = (p_{e^-} - p_{\mu^+})^2 \simeq -s\cos^2\frac{\theta_{\mu^+}}{2}.$$

The modified formulas are

$$\frac{d\sigma_{ee}^F}{d\Omega} = \frac{\alpha^2}{2s}\left(\frac{s^2+u^2}{t^2}|F_s|^2 + \frac{2u^2}{st}\mathrm{Re}\{F_sF_T^*\} + \frac{t^2+u^2}{s^2}|F_T|^2\right)(1+\delta_T^{ee})$$

$$\frac{d\sigma_{\mu\mu}^F}{d\Omega} = \frac{\alpha^2}{2s}\beta\left(\frac{t^2+u^2}{s^2} + (1-\beta^2)\frac{2tu}{s^2}\right)|F_T|^2(1 + \delta_T^{\mu\mu})$$

where $F_S = 1 + f_S t \qquad (Q^2 = t)$

$F_T = 1 + f_T s \qquad (Q^2 = s)$

are the spacelike and timelike form factors. The fits can be done requiring $f_S = f_T$ or allowing them to be different although this would violate crossing symmetry as well as QED.

Using these cross sections, the function $I(\cos\theta)$ is constructed for the 14 bins in $\cos(\theta)$ shown in Fig. 23

$$I(\cos\theta) = \frac{\text{Number of Events } (\cos\theta)}{\text{Luminosity} \times \text{Efficiency } (\cos\theta)} - \int_{\text{bin}} \frac{d\sigma^F}{d\Omega} (\cos\theta)_{d\Omega}$$

The luminosity is found by requiring

$$\sum_{\text{bins}} I(\cos\theta) = 0$$

and then $\sum_{\text{bins}} \frac{I^2(\cos\theta)}{\sigma^2(\cos\theta)}$ is minimized as a function of f of f_S or f_T, where $\sigma(\cos\theta)$ is the standard deviation of I for a given bin.

Table 2 shows the results of fits to the Bhabhas only and Bhabhas and mu-pairs together. These are the result of weighted averages over three samples of data at E_{cm} = 3.0, 3.8, and 4.8 GeV. In each case a fit was done separately requiring $f_S = f_T$ and allowing them to be independent. The results are the fitted parameters in column three. Columns four and five are the results of fitting f to $(\Lambda_+)^{-2}$ and $-(\Lambda_-)^{-2}$ respectively for the positive and negative metric models. Also shown in the table is the result of allowing the form factor at the muon vertex to be different from that at the electron vertex. To keep things simple, we require $f_T = \hat{f}_S$ for the Bhabhas, but now $f_{T\mu} \neq f_{Te}$. Thus in the formula for $d\sigma^F_{\mu\mu}/d\Omega$, we replace $|F_T|^2$ by $\mathrm{Re}\{F_{T_\mu} F_{T_e}{}^*\}$ where

Test of QED

Data Sample Used	Model	Fitted Parameters (In GeV^{-2})	Λ at 95% Conf. (In GeV)	
			Λ_+ Pos Met	Λ_- Neg Met
Bhabhas Only	f_s, f_t Independent	$f_s = 0.0008 \pm 0.0022$ $f_t = 0.0013 \pm 0.0031$	$\Lambda_{s+} > 15$ $\Lambda_{t+} > 13$	$\Lambda_{s-} > 19$ $\Lambda_{t-} > 16$
	$f_s = f_t$	$f = 0.0007 \pm 0.0022$	$\Lambda_+ > 15$	$\Lambda_- > 19$
Bhabhas and MuPairs	f_s, f_t Independent	$f_s = 0.0003 \pm 0.0013$ $f_t = 0.0001 \pm 0.0005$	$\Lambda_{s+} > 21$ $\Lambda_{t+} > 33$	$\Lambda_{s-} > 23$ $\Lambda_{t-} > 36$
	$f_s = f_t$	$f = 0.0002 \pm 0.0004$	$\Lambda_+ > 35$	$\Lambda_- > 47$
	$f_s = f_t$ but f_{tu}, f_{te} Independent	$f_e = 0.0004 \pm 0.0011$ $f_u = 0.0014 \pm 0.0021$ $f_{ue} = 0.0010 \pm 0.0024$	$\Lambda_{e+} > 21$ $\Lambda_{u+} > 14$ $\Lambda_{ue+} > 13$	$\Lambda_{e-} > 27$ $\Lambda_{u-} > 22$ $\Lambda_{ue-} > 15$

Table 2

$$F_{T_\mu} = 1 + f_\mu s$$
$$F_{T_e} = 1 + f_e s$$

and in the formula for $d\sigma^F_{ee}/\Omega d$ we have

$$F_{S_e} = 1 + f_e t$$
$$F_{T_e} = 1 + f_e s \cdot$$

The limits on μ-e universality is defined by

$$\frac{1}{\Lambda_{\mu e}^{\ 2}} = f_{\mu e} = f_\mu - f_e$$

and we also derive $\Lambda_{\mu e^+}$ and $\Lambda_{\mu e^-}$ for positive and negative metrics.

The cutoff parameters determined in Table 2 are considerably larger than any previous values and we have shown that QED is obeyed well in the energy range of our detector.

C. Fit of the Coplanarity Distribution

Now that we have shown to good accuracy that the Bhabha and mu-pair events are present in the detector, there is only one logical step left to complete our understanding of these events. That is to prove that all of the events which we classify as second and third order QED events do indeed belong in that classification. The event classification scheme is described in section V-D. Simply, only two-prong events are candidates for non-hadronic events. Of these, Bhabhas and mu-pairs are classified as in the previous section; collinearity <10°, momentum >Ecm/4. They are separated from each other by their shower pulse heights. The remaining two-prong events consist of radiative QED's ($e^+e^- \to e^+e^-\gamma$, $e^+e^- \to \mu^+\mu^-\gamma$), two-photon

events ($e^+e^- \to e^+e^-A^+A^-$), and two-prong hadronic events. The radiative Bhabhas are separated from the rest on the basis of their large pulse heights and at least one track having 2/3 of the beam energy or more. The remaining two prongs are cut to require $p < 300$ MeV/c and $\psi < 20°$; this eliminates hadron events. The removed events are considered entirely hadronic, as contamination by radiative mu-pairs should be small.

To test our classification of two prongs, we will fit a coplanarity distribution of all Bhabhas and radiative Bhabhas to the calculated distribution by Berends et al. Figs. 24, 25 and 26 show the coplanarity distribution of the data and the calculation. The region $\psi = [160°, 180°]$ is left off since it is not possible to separate events of the type $e^+e^- \to e^+e^-\gamma$ in this region from $e^+e^- \to \gamma\gamma$ events where one $\gamma \to e^+e^-$ in the beam pipe. The errors shown on the data are statistical. Those on the calculations are negligible in comparison, except in the bin $\psi = [0°, 2°]$. The calculation becomes very inaccurate as $\psi \to 0°$ so we exclude the first bin for fitting purposes. The three different momentum cutoffs are $p > 200$ MeV/c, a maximal sample, $p > 600$ MeV/c, and $p > 900$ MeV/c.

The remaining range $\psi = [2°, 160°]$ is divided into 79 two-degree bins. The effective luminosity (luminosity times efficiency) is found by requiring

$$\sum_{\psi=[2°,160°]} N(\psi) = L \sum_{\psi=[2°,160°]} \int_{\Delta\psi} \frac{d\sigma(\psi)}{d\psi}\, d\psi$$

where $N(\psi)$ is the number of events per bin, L is the time-integrated luminosity times efficiency and $\int_{\Delta\psi} d\sigma(\psi)/d\psi\, d\psi$ is the calculated

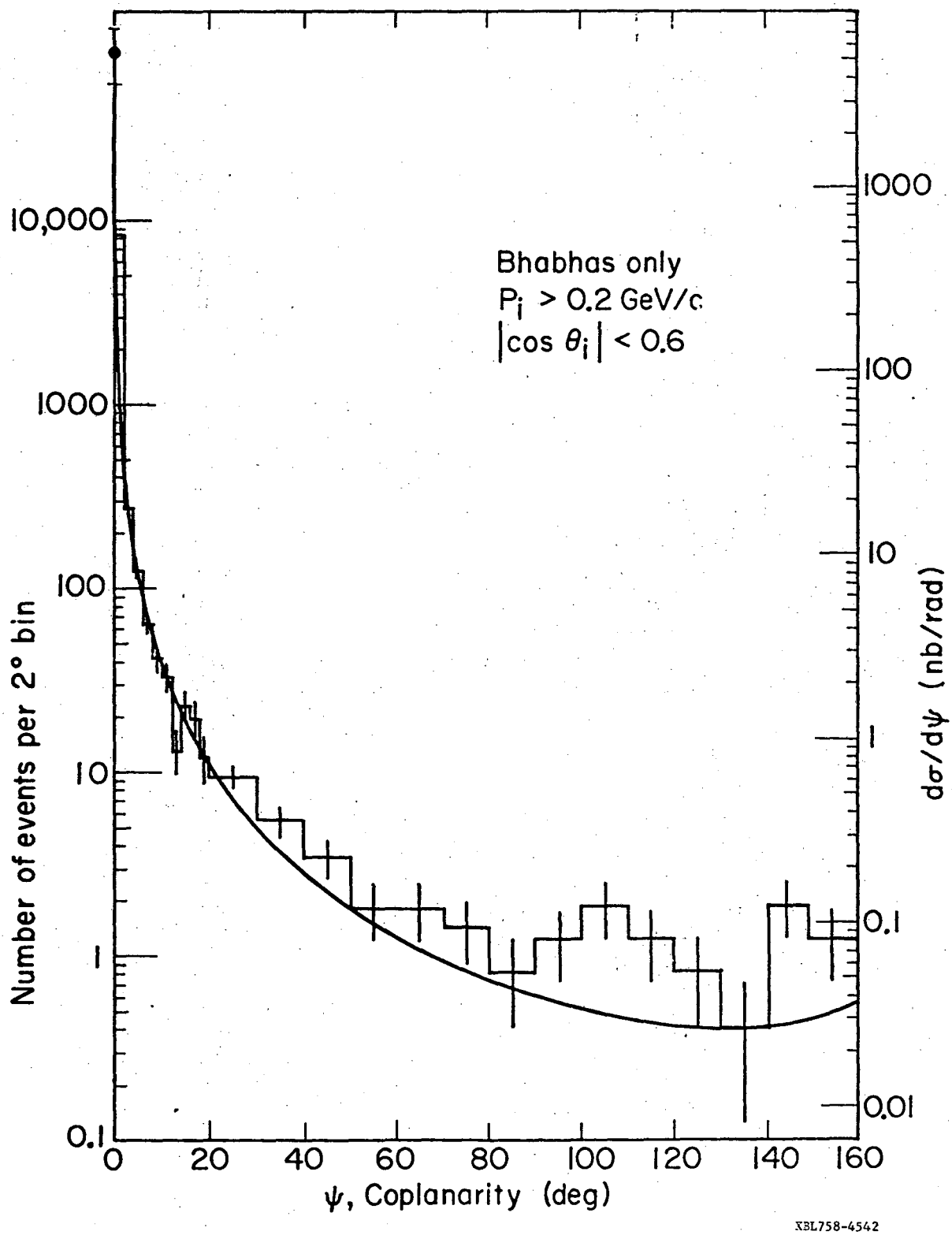
Bhabhas only
P_i > 0.2 GeV/c
$|\cos\theta_i|$ < 0.6
Number of events per 2° bin
10,000
1000
100
10
1
0.1
$d\sigma/d\psi$ (nb/rad)
1000
100
10
1
0.1
0.01
0
20
40
60
80
100
120
140
160
ψ, Coplanarity (deg)
XBL758-4542

Figure 24

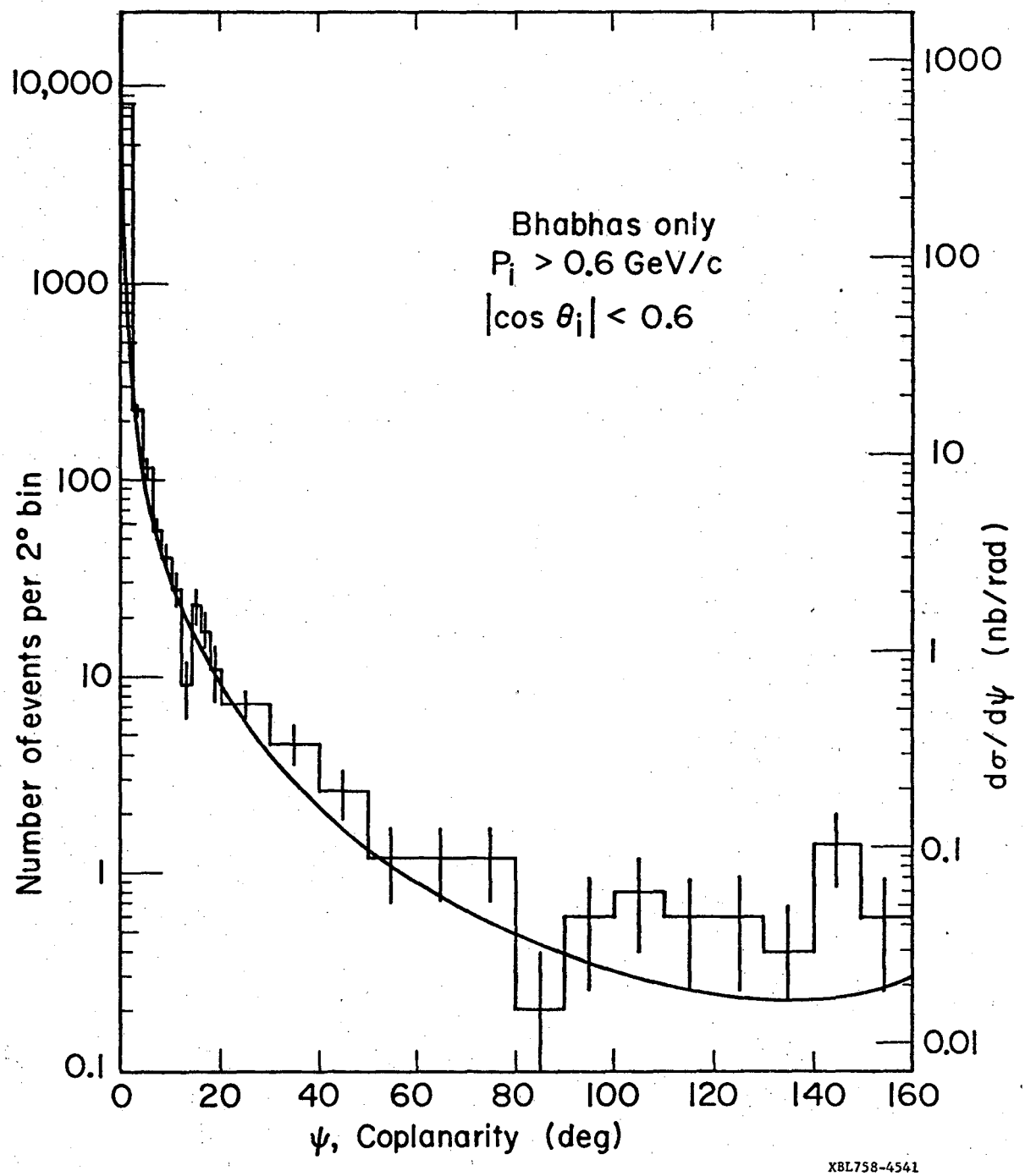
Bhabhas only
P_i > 0.6 GeV/c
$|\cos\theta_i|$ < 0.6
Number of events per 2° bin
10,000
1000
100
10
1
0.1
$d\sigma/d\psi$ (nb/rad)
1000
100
10
1
0.1
0.01
0
20
40
60
80
100
120
140
160
ψ, Coplanarity (deg)
XBL758-4541

Figure 25

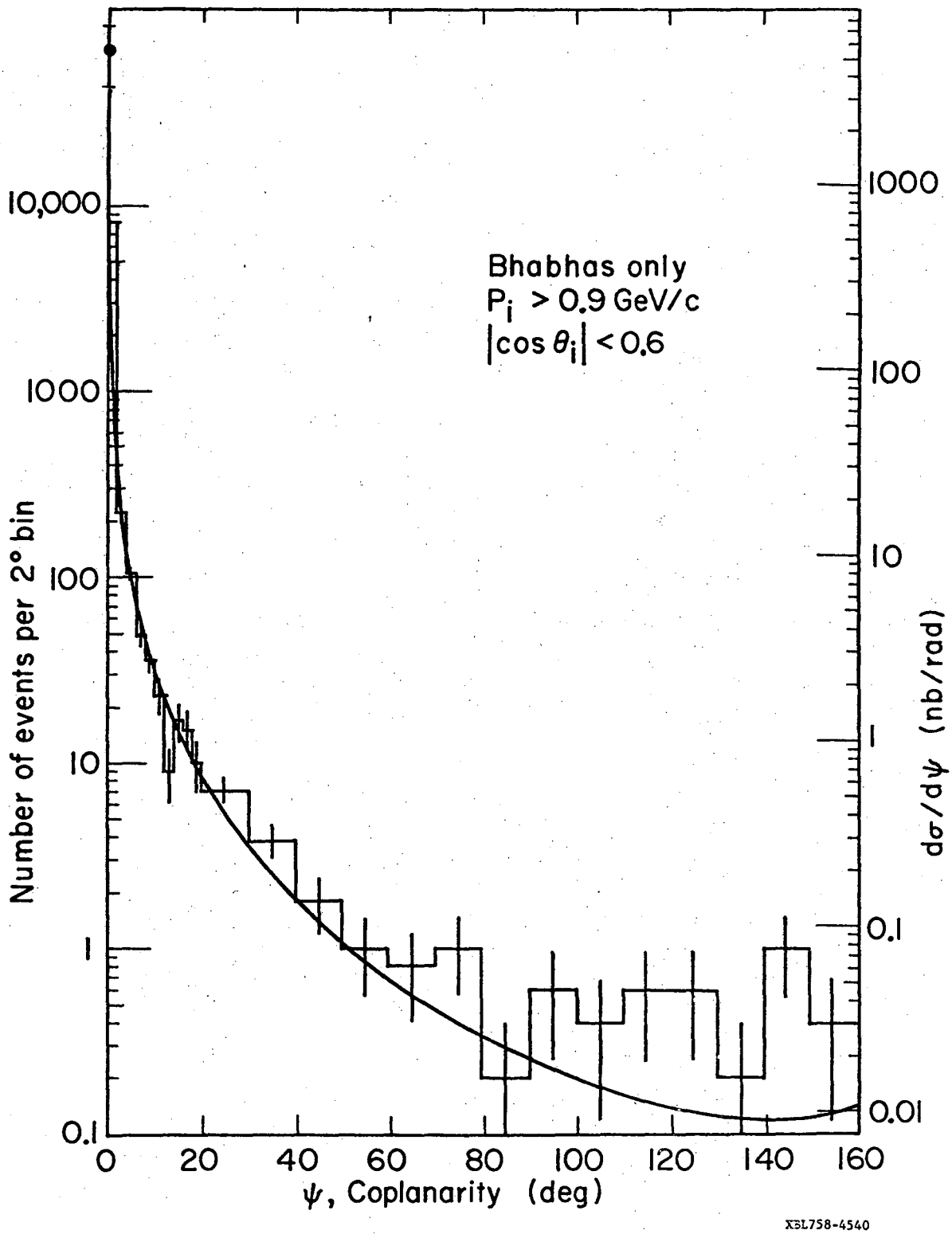
Bhabhas only
$P_i > 0.9$ GeV/c
$|\cos\theta_i| < 0.6$
Number of events per 2° bin
10,000
1000
100
10
1
0.1
$d\sigma/d\psi$ (nb/rad)
1000
100
10
1
0.1
0.01
0
20
40
60
80
100
120
140
160
ψ, Coplanarity (deg)
XBL758-4540

Figure 26

cross section integrated over a bin. This removes one degree of freedom. χ^2 is calculated for the fit in the range $\psi = [2°, 160°]$ and confidence levels are given in Table 3. As can be seen all fits are excellent.

Possible causes of errors in previous fits are:

1) All of the errors in determining space points in the spark chambers contribute to an error in the determination of ψ. This may cause the particularly steep bins to spill into each other enough to significantly flatten the distribution. We estimate the error on ψ is $<<1°$.

2) The separation of the Bhabhas from other two prongs is not infallible. Some Bhabhas are lost; some events are not Bhabhas. To eliminate error from the second source, we did a further fit of the following nature: All two-prong events, instead of just Bhabhas and radiative Bhabhas were fit to a theoretical coplanarity distribution. The theoretical distribution accounted for Bhabhas and mu-pairs using the calculations of Berends. It accounted for two-photon events using calculations borrowed from section V. Calculating the expected two-prong hadronic sample was more difficult. The Monte Carlo calculation described in section III was used to calculate the coplanarity distribution of two-prong hadrons and the overall normalization was found through a fit.

In this case we had

$$N(\Psi) = L \int_{\Delta\Psi} \frac{d\sigma(\Psi)}{d\Psi} + R \; H(\Psi)$$

where $N(\psi)$ is the number of all two-prong events in a 2° bin.

Radiative Bhabha Fit

	χ^2	Deg. of Freedom	Confidence Level
p>0.2 GeV/c	71.56	78	68.6%
p>0.6 Gev/c	72.60	78	65.6%
p>0.9 GeV/c	62.78	78	89.3%

All Two Prong Fit

	χ^2	Deg. of Freedom	Confidence Level
p>0.2 Gev/c	107.6	77	1.07%
p>0.6 GeV/c	58.33	77	94.2%
p>0.9 GeV/c	47.67	77	99.5%

Table 3

$\int_{\Delta\psi} d\sigma(\psi)/d\psi \, d\psi$ is a sum of the calculations for $e^+e^- \to e^+e^-$, $e^+e^- \to \mu^+\mu^-$, $e^+e^- \to e^+e^-e^+e^-$, and $e^+e^- \to e^+e^-\mu^+\mu^-$ integrated over a bin. L is the effective luminosity. $H(\psi)$ is the Monte Carlo distribution for two-prong hadron events integrated over a bin, and R is a factor to normalize this distribution. Again we used 79 two-degree bins in $\psi = [2°, 160°]$ and did three separate fits for $p > 200$ MeV/c, $p > 600$ MeV/c, and $p > 900$ MeV/c.

This time we had two constants, L and R, to fit. We did this by requiring an integrated fit in two sub-regions $\psi = [2°, 20°]$ and $\psi = [20°, 160°]$ rather than just the full region. Hence we had

$$\sum_{\psi=[2°,20°]} N(\psi) = L \sum_{\psi=[2°,20°]} \int_{\Delta\psi} \frac{d\sigma(\psi)}{d\psi} d\psi + R \sum_{\psi=[2°,20°]} H(\psi)$$

$$\sum_{\psi=[20°,160°]} N(\psi) = L \sum_{\psi=[20°,160°]} \int_{\Delta\psi} \frac{d\sigma(\psi)}{d\psi} d\psi + R \sum_{\psi=[20°,160°]} H(\psi)$$

and we solved the two equations for the two unknowns, L and R, eliminating two degrees of freedom. These fits are shown in Figs. 27, 28 and 29 and χ^2 and confidence levels are listed in Table 3.

In this case the fit is poor for the sample $p > 200$ MeV/c, but the fit gets better for $p > 600$ MeV/c and is even better than the radiative Bhabha fits for $p > 900$ MeV/c. The reason is that the $p \gtrsim 200$ MeV/c sample contains a large number of hadronic two prongs, most of which have low momenta. As the momentum cutoff is increased, the hadronic events are practically eliminated while the radiative events are unaffected. Thus, the small confidence level at low momentum is due to the crudely fit hadron events while the

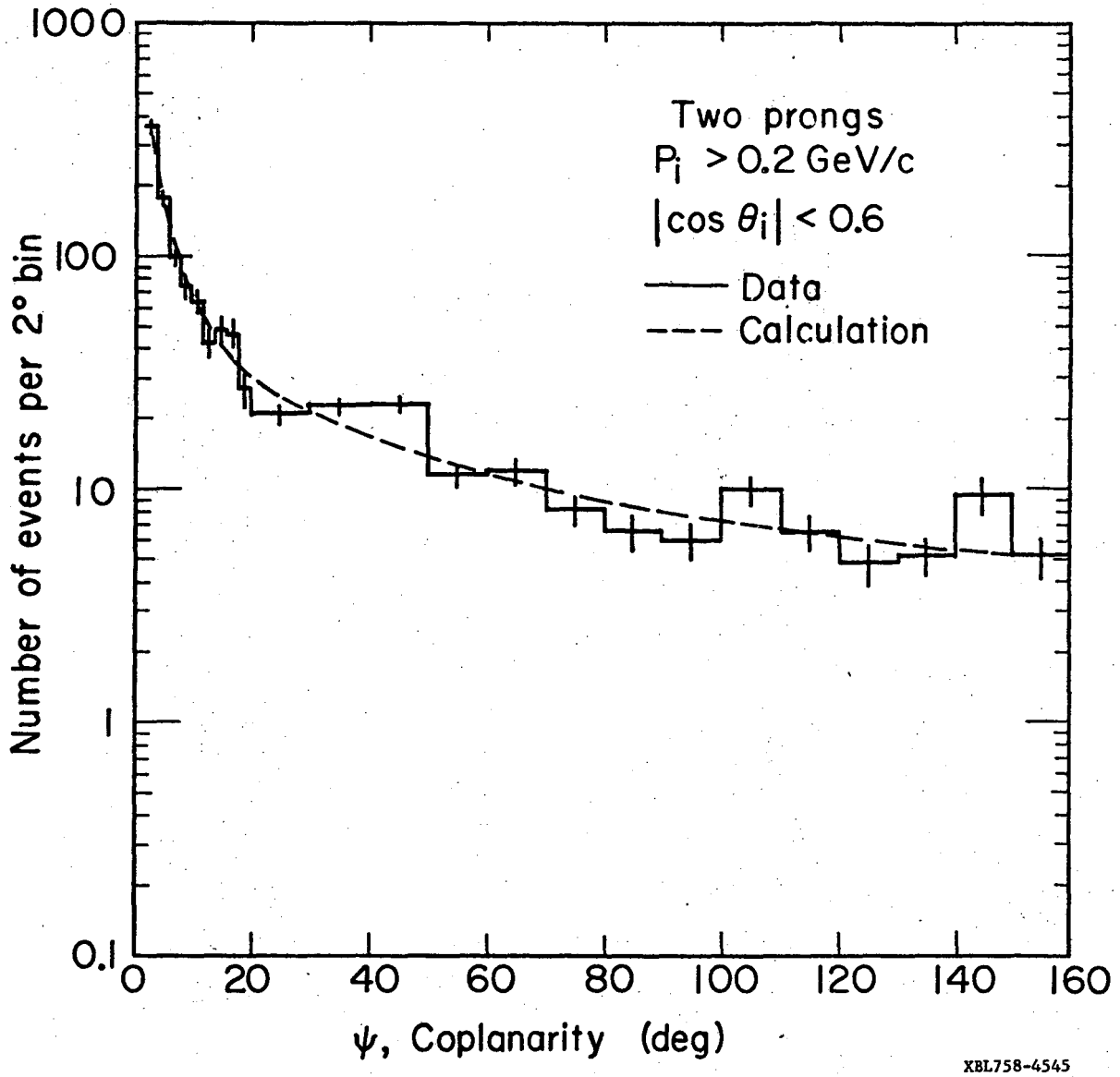
Two prongs
P_i > 0.2 GeV/c
$|\cos\theta_i| < 0.6$
Data
Calculation
Number of events per 2° bin
1000
100
10
1
0.1
0
20
40
60
80
100
120
140
160
ψ, Coplanarity (deg)
XBL758-4545

Figure 27

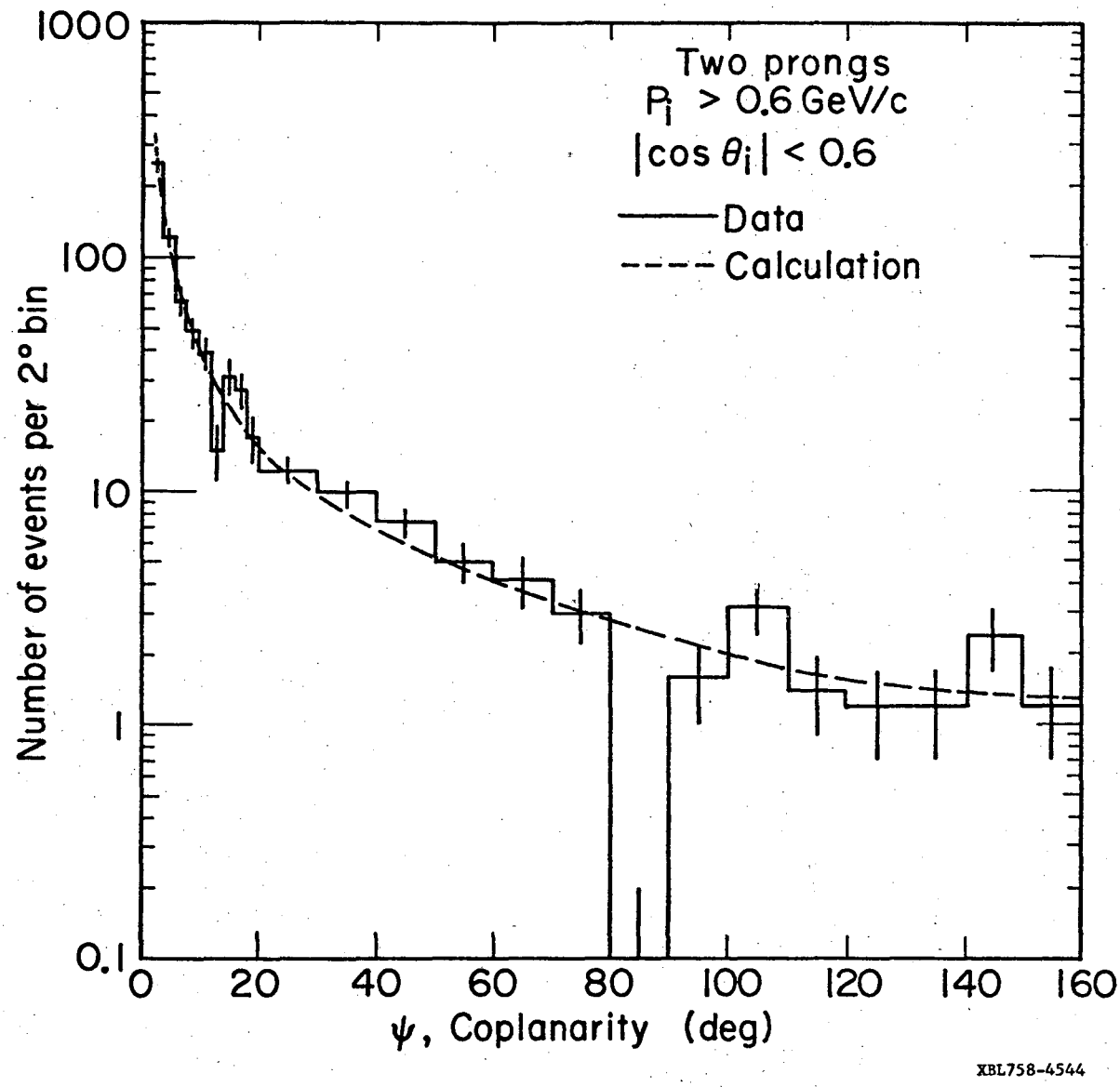
Two prongs
P_i > 0.6 GeV/c
$|\cos\theta_i|$ < 0.6
Data
Calculation
Number of events per 2° bin
1000
100
10
1
0.1
0
20
40
60
80
100
120
140
160
ψ, Coplanarity (deg)
XBL758-4544

Figure 28

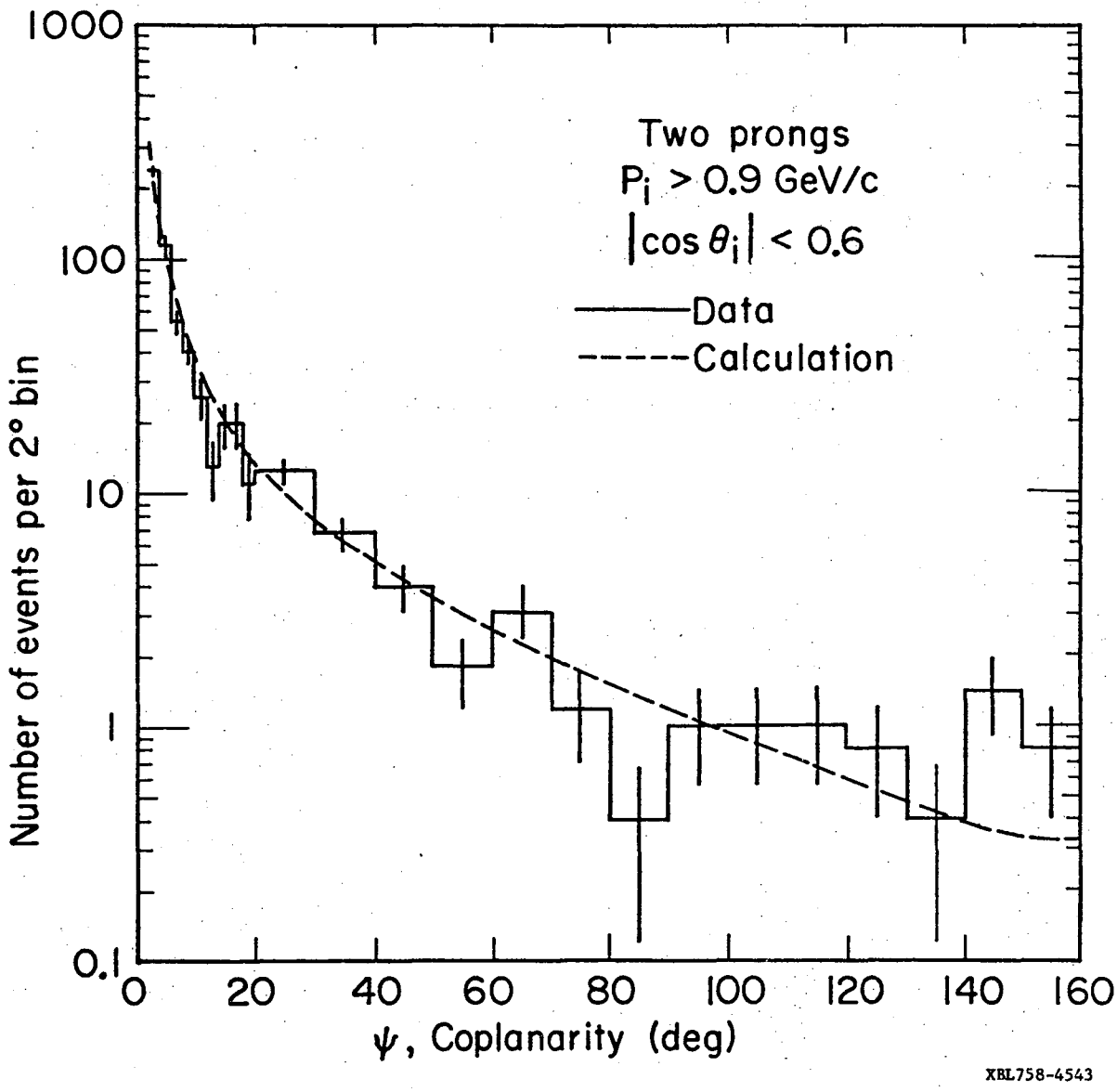
Two prongs
$P_i > 0.9$ GeV/c
$|\cos\theta_i| < 0.6$
Data
Calculation
Number of events per 2° bin
1000
100
10
1
0.1
0
20
40
60
80
100
120
140
160
ψ, Coplanarity (deg)
XBL758-4543

Figure 29

excellent fit at higher momenta demonstrate a fit to the radiative events which is even better than that to radiative Bhabhas only.

By doing all of these fits we have given ourselves confidence in two things. First, we know that our event classification scheme is reasonable and those events which are classified as QED events indeed fit the expected distribution. Also we know that the remaining events should be classified as hadron events, for they are not accountable for in any other way. Our use of this two-prong class in the hadron Monte Carlo and unfold is justified.

V. Fourth Order QED Cross Sections and the Two-Photon Process

In this section we will consider the fourth order cross sections which have not been discussed in the section on the radiative corrections. This is equivalent to the class of processes where the electron and positron produce four final state particles, none of them photons. The study of these processes is important for the understanding of their contamination to lower order processes, as a high order test of QED, and as a source of new information on the hadronic interaction.

In the past, the two-photon process (Fig. 30a) has been calculated to provide a significant cross section in e^+e^- interactions.[12] Here the electron and positron each emit a photon and continue forward, while the photons collide to produce a pair. Typically, the electron and positron escape down the beam pipe undetected and the pair is easily mistaken to be a one-photon event such as $e^+e^- \to \gamma \to \pi^+\pi^-\pi^+\pi^-$ where only two particles reach the detector. We will refer to the diagram of Fig. 30a as the C = + two-photon process, since the produced pair, which is usually all that is observed, has positive C parity.

Also, as has been shown by several authors,[21,22,23,24,25] the C = - two-photon processes (Fig. 30b) may become significant and must be understood. In this section we will calculate the cross sections for

$$e^+e^- \to e^+e^-e^+e^-$$
$$e^+e^- \to e^+e^-\mu^+\mu^-$$
$$e^+e^- \to e^+e^-\pi^+\pi^- \quad \text{(pointlike)}$$

0 0 0 0 4 4 0 2 7 3 6

FOURTH ORDER QED DIAGRAMS

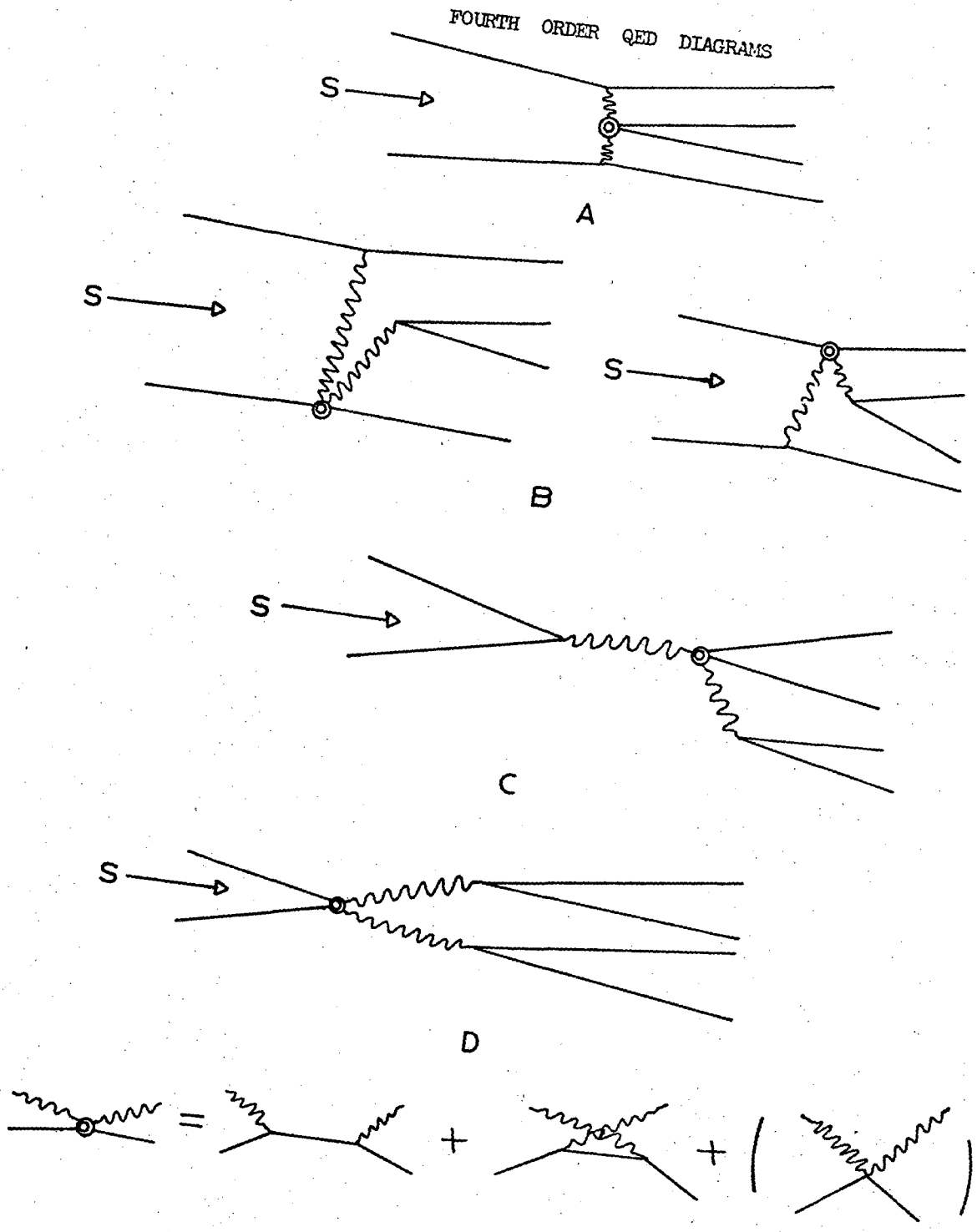

Figure 30

XBL 756-1724

and compare them with the data. This will provide a measure of our confidence in the calculation of their contamination to the lower order processes and provide a test of QED since the $\pi\pi$ cross section is relatively small. The cross section for the process

$$e^+e^- \to e^+e^- + \text{hadrons}$$

will also be measured from the data. The cross section is large enough at present energies to provide new information on the hadronic interaction through photon-photon collisions. The hadron physics of the two-photon process will be considered in the last section. Two photon events have previously been observed at Novosibirsk[40] and Frascati.[41,42]

A. Order of Magnitude Estimates

All non-radiative fourth order QED processes are shown in Fig. 30 , where it is understood that final state particles are electrons or muons where possible and exchange diagrams will be included. Naively one would guess that, since all of these processes are fourth order, the cross sections are of order

$$\sigma \cong (\hbar c)^2 \frac{\alpha^4}{E^2} = 2. \times 10^{-4}\ nb \qquad at \quad E = 2.4\ GeV$$

However, the process of emitting a bremsstrahlung photon as in 30a and b actually contributes a factor of $\alpha/\pi \ln E/m_e$ where m_e is the electron mass rather than α/E and the process 30a is asymptotically of order

$$\sigma_a \to \frac{112}{9\pi} \frac{\alpha^4}{m_f} \left(\ln \frac{E}{m_e}\right)^2 \left(\ln \frac{E}{m_f}\right)$$

where m_f is the mass of the produced particles.[12] For muons at E = 2.4 GeV this is

$$\sigma_a \rightarrow 90 \text{ nb}$$

which is comparable to the one-photon hadronic cross sections. Fortunately (or unfortunately from the point of view of two-photon physics) most of this cross section is undetectable with the magnetic detector cuts for two reasons. First, typical of bremsstrahlung processes, the scattered electron and positron tend to continue forward emitting only low-energy photons. The produced particles peak at zero momentum and tend to fail to reach the spark chambers. This eliminates most of the cross section. Secondly, of those produced particles that have enough momentum, only about 10% fall within the angle cuts $|\cos\theta| < 0.6$.[22]

Hence, in this section we will consider carefully the C = + (two-photon) process (Fig. 30a) and the C = - process (Fig. 30b). The remaining diagrams are expected to be of order 2×10^{-4} nb and therefore negligible. Contributions from 30c are discussed by Arteaga-Romero et al.[21,22,23,24] and those from 30d are discussed by Attukhov.[28]

In Table 4 we present estimates of the cross sections for the C = + and C = - processes from three different authors. First are estimates by Brodsky et al.[12] of C = + cross sections using the equivalent photon approximation. $\sigma_{tot}(c = +)$ are their calculations for $e^+e^- \rightarrow e^+e^-\mu^+\mu^-$ and $e^+e^- \rightarrow e^+e^-\pi^+\pi^-$ (pointlike) total cross sections. $\sigma_{eff}(C = +)$ are estimates of the cross sections detected by the magnetic detector. σ_{eff} is obtained by using their asymptotic formulae

Estimates of Cross Sections for $e^+e^- \to e^+e^-A^+A^-$

Where A is as Indicated and E=2.4 GeV

Brodsky, Kinoshita, Terazawa[12] - Equivalent Photon

A^+A^-	e^+e^-	u^+u^-	$\pi^+\pi^-$ point	$\pi^+\pi^-$ ρ dom.	K^+K^- point	K^+K^- ϕ dom.
$\sigma_{TOT}(C=+)$ =	-	40 nb	3 nb	-	-	-
$\sigma_{EFF}(C=+)$ =	7 nb	5 nb	0.6 nb	-	.05 nb	-

Baier, Fadin[25] - Asymtotic Limit

$\sigma_{TOT}(C=+)$ =	1 mb	30 nb	2 nb	-	.05 nb	-
$\sigma_{TOT}(C=-)$ =	-	1 nb	0.1 nb	0.8 nb	.01 nb	.03 nb

Arteaga-Romero, Jaccarini, Kessler, Parisi[22] - Upper Limits

$\sigma_{EFF}(C=+)$ =	6 nb	2 nb	0.3 nb	-	.03 nb	-
$\sigma_{TOT}(C=-) <$	300 nb	100 nb	30 nb	30 nb	.01 nb	10 nb

Table 4

$$\sigma(E) = \frac{112}{9\pi} \frac{\alpha^4}{m_f^2} \left(\ln \frac{E}{m_e}\right)^2 \left(\ln \frac{E}{m_f}\right) \quad \text{for Spin} = \tfrac{1}{2} \text{ produced particles}$$

$$\sigma(E) = \frac{16}{9\pi} \frac{\alpha^4}{m_f^2} \left(\ln \frac{E}{m_e}\right)^2 \left(\ln \frac{E}{m_f}\right) \quad \text{for Spin} = 0 \text{ produced particles}$$

and substituting for m_f, the energy of a "just detectable" particle, i.e. one with p = 200 MeV/c. This number is then multiplied by their bias factor to account for the angular cutoff of the detector.

Next are Baier and Fadin's[25,30] asymptotic estimates for both C = + and C = -. They have expressed cross sections in terms of leading logarithms without using the equivalent photon approximation. Included are results for pointlike particles and pions and kaons in the limit of ρ and ϕ dominance respectively.

Finally we use the $d\sigma/dM$ plots of Arteaga-Romero et al.[22] where M is the effective mass of the produced state. For the C = + process we assume the momenta of the produced particles are roughly opposite and integrate $d\sigma/dM$ down to the minimum allowed effective mass for p = 200 MeV/c particles. This number is then corrected for angular acceptance using their graphs of angular distribution for the produced particles. Since the scattered particles are cut off at $\theta < 1°$, we must also correct for the fraction of the cross section lost by multiplying by $(2.55)^2$, a factor calculated from the equivalant photon approximation. For the C = - process, it is not possible to incorporate the momentum cutoff into the effective mass since the momenta of the two produced particles are not primarily opposite. Therefore we calculate only a total cross section for C = -. Further, we cannot handle the 1° cutoff of the scattered

particles well. For the bremsstrahlung electron a factor of 2.55 is appropriate since the equivalent photon approximation applies, but the distribution of the other electron is difficult to estimate. It is likely to peak forward, but little more can be said. Therefore we merely assume a phase space distribution and use the result as an upper limit.

From the table we can see that the c = + effective cross section is definitely non-negligible, and no really good estimates of the C = - effective cross section exist. However, judging from the C = - total cross section, we can see that it may have a significant effective cross section and needs to be understood.

For these reasons, we have done detailed calculations for both of these cross sections using the cuts imposed by the detector. We generally regard cross sections of the order of 10^{-2} nb as negligible and find that, if a momentum cut of p = 300 MeV/c and a coplanarity cut of $\psi > 20°$ is imposed, the C = - process is eliminated, and cross sections for the C = + process can be calculated sufficiently well. In the next two parts we consider the calculations of these two processes in detail.

B. The C = + Two-Photon Process

1. Methods of Calculation

There has been considerable interest in the past few years in the two-photon process as a means of studying gamma-gamma collisions.[26,31] If the scattered electron and positron are detected

in the near forward direction, the photons are almost real, and the cross section appears to be large enough due to the bremsstrahlung enhancement, that measurable rates can be detected. The $\gamma\gamma \to X$ cross section can be determined from $e^+e^- \to e^+e^-X(C = +)$ cross sections from the formula[12]

$$\sigma_{e^+e^- \to e^+e^-X}(E) = 2\left(\frac{\alpha}{\pi}\right)^2\left(\ln\frac{E}{m_e} - \frac{1}{2}\right)^2 \int_0^{4E^2} \frac{ds}{s} f\left(\frac{\sqrt{s}}{2E}\right) \sigma_{\gamma\gamma \to X}(s)$$

where

$$f(x) = (2+x^2)^2 \ln\left(\frac{1}{x}\right) - (1-x^2)(3+x^2)$$

in the limit that the photons are real. The approximations used in obtaining this formula are:

1) The photons are emitted in the forward direction.

2) The photons have only transverse polarizations.

This allows one to average over the azimuthal angles of both the scattered electron and positron eliminating one degree of freedom, but also eliminating all information about the total transverse momentum of the produced state.

This method greatly simplifies the calculation of fourth order QED processes, because a seven-dimensional integral is reduced to two three-dimension integrals, one of which can be done analytically. Many authors have discussed the accuracy of this method both from a theoretical[32,33,34] and calculational[12,35,36] point of view. None claim it to be better than 10-20% and some claim it to be much worse. The major problems summarized by Bonneau et al.[32] are

1) The approximation that the photons are real breaks down when the electron or positron is scattered to large angles, and this can

happen for a significant part of the cross section. Since we will be interested in calculating contamination to the hadronic cross section, we cannot assume the scattered particles will be collected at small angles.

2) Longitudinal and scalar polarization terms will not necessarily be small, especially for massive photons.

3) The expression is derived to highest order in E/m_e. At $E = 2.4$ GeV we are not in a sufficiently asymptotic region to neglect the lower powers; E will have to increase by many orders of magnitude before that is possible.

4) The asymptotic form of this cross section is wrong by a factor of 2/3. This can be corrected by changing

$$\left(\ln \frac{E}{m_e} - \frac{1}{2}\right)^2$$

to

$$\left(\ln \left\{\frac{E}{m_e}\frac{\sqrt{s}}{\omega_1}\right\} - \frac{1}{2}\right)\left(\ln \left\{\frac{E}{m_e}\frac{\sqrt{s}}{\omega_2}\right\} - \frac{1}{2}\right)$$

where $\sqrt{s}$ is the invariant mass of the two-photon state and ω_1 and ω_2 are the energies of the photons, but this would increase the complexity of the integration. Bonneau et al. estimate the error at 30-40%.[32]

5) If this form is used to study $e^+e^- \to e^+e^-\pi^+\pi^-$, the three independent form factors in the Cheng-Wu analysis are constrained to just one, restricting the possible dynamics.

6) Total transverse momentum is an important quantity to measure for separation of two-photon events from other hadronic processes, but this quantity is lost in the approximation.

For these reasons we decided that the equivalent photon method would be insufficient for calculating fourth order cross sections.

Much work has been done on the exact calculation of these processes, but there has been considerable difficulty.[12,35,36] One generally attempts to numerically integrate the seven-dimensional cross section. This has been done successfully only by holding one or more of the variables fixed. The problems arise from peaks in the integrand as a function of almost all of the variables. For the SPEAR detector, however, the situation is not this bad, since the natural momentum and angle cutoffs of the detector eliminate or minimize the worst of these peaks. We have done a Monte Carlo integration of the exact formulas to determine effective cross sections good to about 10%. Later we compare the results to those using the equivalent photon method.

In the next section the exact formula is derived, and the results of the numerical integration are given in the following sections. The exact formula, F2 , can be integrated in several ways depending upon how one wishes to express the phase space. All methods in principle give identical results, but some are more efficient than others. Due to the complexity of the integration, four different methods were tested and one, the BKT method expressed by formula F3, was chosen and used throughout. The next sections include a discussion of these methods.

2. Exact Calculation of $e^+e^- \to e^+e^-A^+A^-$

a. Phase Space Calculation

The cross section for the process $e^+e^- \to e^+e^-A^+A^-$ can be calculated exactly when A^+A^- are a pointlike fermion-antifermion or boson-antiboson pair. The numerical integration can be performed in several different ways, however, and, due to its complexity, results have been found to differ by about 30%.

To calculate the cross section we follow Brodsky et al.[12] and label the momenta and energies as shown in Fig. 31 , E_x, $\vec{p}_x$ are the energy and momentum of the two-photon final state so that $\vec{p}_x = \vec{K}_1 + \vec{K}_2 = \vec{q}_1 + \vec{q}_2$. We choose a coordinate system such that the initial particles are in their center of mass traveling along the Z axis, and the scattered positron p_1' is in the X-Y plane. The cross section is:

$$\sigma = e^8 \frac{1}{|\vec{V}_1 - \vec{V}_2|} \frac{m_e}{E_1} \frac{m_e}{E_2} \frac{1}{4} \sum_{s_1, s_2, s_1', s_2'} \int \frac{m_e\, d^3p_1'}{(2\pi)^3 E_1'} \int \frac{m_e\, d^3p_2'}{(2\pi)^3 E_2'} \int \frac{\rho_1\, d^3q_1}{(2\pi)^3\, 2W_1} \int \frac{\rho_2\, d^3q_2}{(2\pi)^3\, 2W_2}$$

$$\times (2\pi)^4 \delta^4(p_1 + p_2 - p_1' - p_2' - q_1 - q_2)\, T^{\mu\nu}(p_1, p_1')\, M^{\dagger}_{\mu\alpha} M_{\nu\beta}\, T^{\alpha\beta}(p_2, p_2') \frac{1}{(K_1^2 K_2^2)^2}$$

where M_e is the electron mass, $\rho_i = 1$ if the produced particles are bosons and $\rho_i = 2M_p$, twice the mass, if the produced particles are fermions.

$$T^{\mu\nu}(p_1, p_1') = \bar{V}(p_1')\, \gamma^\mu\, V(p_1)\, V(p_1)\, \gamma^\nu\, \bar{V}(p_1')$$

$$T^{\alpha\beta}(p_2, p_2') = \bar{u}(p_2')\, \gamma^\alpha\, u(p_2)\, u(p_2)\, \gamma^\beta\, \bar{u}(p_2')$$

and $M_{\nu\beta}$ is the matrix element for $\gamma\gamma \to A^+A^-$. Then using current conservation we calculate

TWO PHOTON COORDINATE SYSTEM

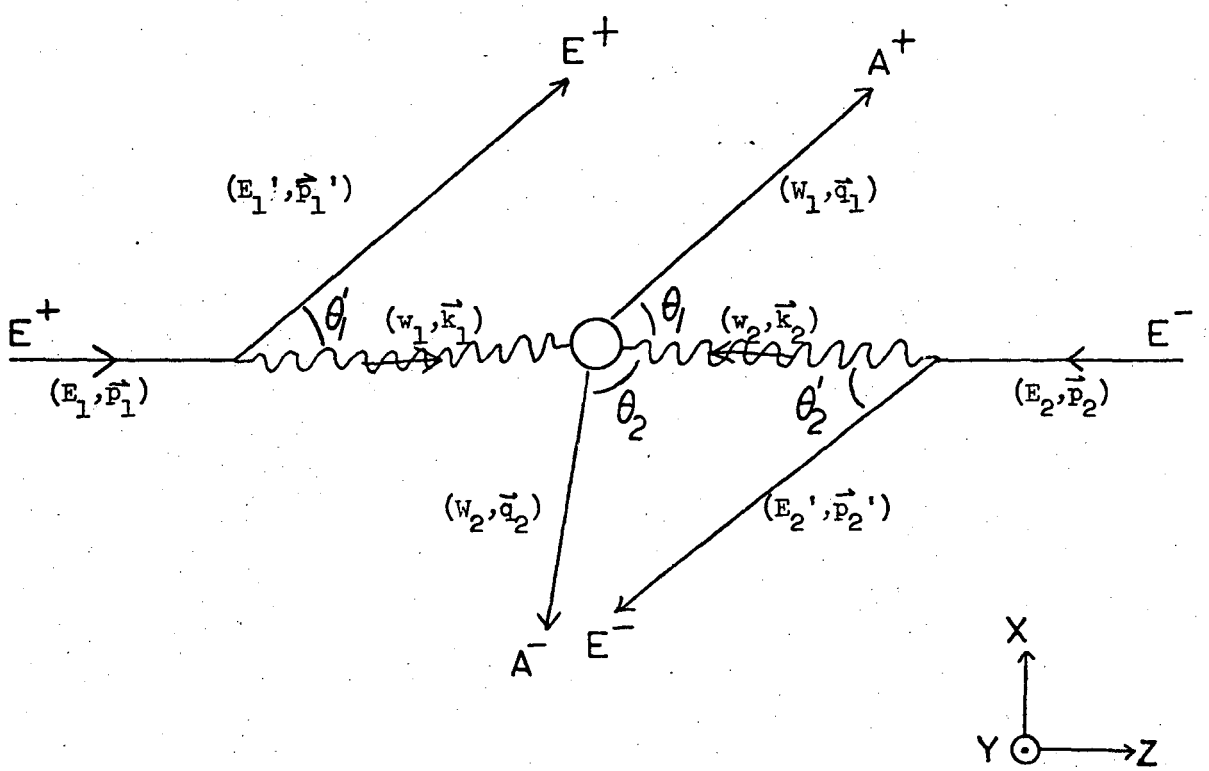

$$(E_x,\vec{p}_x)=(W_1+W_2,\vec{q}_1+\vec{q}_2)$$

$$\cos(\theta_x)=\frac{\vec{p}_x\cdot\vec{p}_1}{|\vec{p}_x|\,|\vec{p}_1|}$$

XBL 756-1725

Figure 31

$$m_e^2 \sum_{s_1, s_1'} T^{\mu\nu}(p_1, p_1') = 2 p_1^{\mu} p_1^{\nu} + \frac{1}{2} K_1^2 g^{\mu\nu}$$

$$= t^{\mu\nu}(p_1, K_1)$$

$$m_e^2 \sum_{s_2, s_2'} T^{\alpha\beta}(p_2, p_2') = t^{\alpha\beta}(p_2, K_2)$$

to find

$$\sigma = \left(\frac{e^2}{(2\pi)^3}\right)^4 \frac{1}{E^2} \frac{1}{|\vec{V}_1 - \vec{V}_2|} \int \frac{d^3p_1'}{E_1'} \int \frac{d^3p_2'}{E_2'} \int \frac{d^3q_1}{2W_1} \int \frac{d^3q_2}{2W_2} (2\pi)^4 \delta^4(p_1+p_2-p_1'-p_2'-q_1-q_2) \frac{D}{(K_1^2 \ldots}$$

where

$$D = \frac{1}{4} p_1 p_2 \, t^{\mu\nu}(p_1, K_1) M^{+}_{\mu\alpha} M_{\nu\beta} \, t^{\alpha\beta}(p_2, K_2)$$

and

$$E_1 = E_2 = E \qquad \text{(Formula F1)}$$

To do the exact calculation, we reduce the phase space in the following way

$$\int \frac{d^3p_1'}{E_1'} \int \frac{d^3p_2'}{E_2'} \delta^4(p_1+p_2-p_1'-p_2'-q_1-q_2)$$

$$= \int_{-1}^{1} d\cos\theta_1' \int_{m_e}^{\infty} dE_1' \frac{2\pi}{|\vec{p}_x|} \delta(\cos\beta - \cos\theta_x \cos\theta_1' - \sin\theta_x \sin\theta_1' \cos\phi_x)$$

$$\times \theta(2E - E_x - E_1')$$

where

$$\cos\beta = \frac{(2E - E_x)^2 - \vec{p}_x^{\,2} - 2E_1'(2E - E_x)}{2 \, |\vec{p}_1'| \, |\vec{p}_x|}$$

The produced particle phase space is written

$$\int \frac{d^3q_1}{W_1} \int \frac{d^3q_2}{W_2} = \int_{m_p}^{\infty} dW_1 \int_{-1}^{1} d\cos\theta_1 \int_{m_p}^{\infty} dW_2 \int_{-1}^{1} d\cos\theta_2 \, |\vec{q}_1||\vec{q}_2| \int_{-\pi}^{\pi} d\phi_1 \int_{-\pi}^{\pi} d\phi_2$$

It is useful to describe the final state in terms of "coplanarity

angle" ψ where $\cos\psi = (\vec{q}_1 \times \vec{p}_1)/(|\vec{q}_1 \times \vec{p}_1|) \cdot (\vec{q}_2 \times \vec{p}_2)/(|\vec{q}_2 \times \vec{p}_2|)$. This is equivalent to $\cos\psi = -\cos(\phi_1 - \phi_2)$. The coplanarity angle is a measure of the angle between the projections of $\vec{q}_1$ and $\vec{q}_2$ in the x-y plane. $\psi = 0$ indicates $\vec{q}_{1\perp}$ and $\vec{q}_{2\perp}$ oppositely directed while $\psi = \pi$ indicates they point in the same direction.

Using ϕ_x, the azimuthal angle of the vector $\vec{p}_x = \vec{q}_1 + \vec{q}_2$, we can write:

$$\int_{-\pi}^{\pi} d\phi_1 \int_{-\pi}^{\pi} d\phi_2 = \frac{1}{J} \iint_{\substack{-\pi < \phi_1 < \pi \\ -\pi < \phi_2 < \pi}} d\phi_x \, d\cos\psi$$

with

$$J = \frac{\partial(\phi_x, \cos\psi)}{\partial(\phi_1, \phi_2)}$$

and determine the limits on ϕ_x and $\cos\psi$ in the following way: ϕ_x is some angle in the acute region between ϕ_1 and ϕ_2 and can have any value between $-\pi$ and π. For a given value of ϕ_x, there are two possible regions for ϕ_1 and ϕ_2 as shown in Fig. 32.

1) The region we denote by b = +1

where

$$\phi_x - \pi < \phi_1 < \phi_x$$
$$\phi_x < \phi_2 < \phi_x + \pi$$

2) The region we denote by b = -1

where

$$\phi_x < \phi_1 < \phi_x + \pi$$
$$\phi_x - \pi < \phi_2 < \phi_x$$

For each of these regions $|\phi_1 - \phi_2|$ can range only from 0 to π since ϕ_x is in the acute region between ϕ_1 and ϕ_2, so $\cos(\phi_1 - \phi_2) = -\cos\psi$ ranges from -1 to 1. Therefore $\cos\psi$ also ranges from -1 to

TWO CONFIGURATIONS OF AZIMUTHAL ANGLES

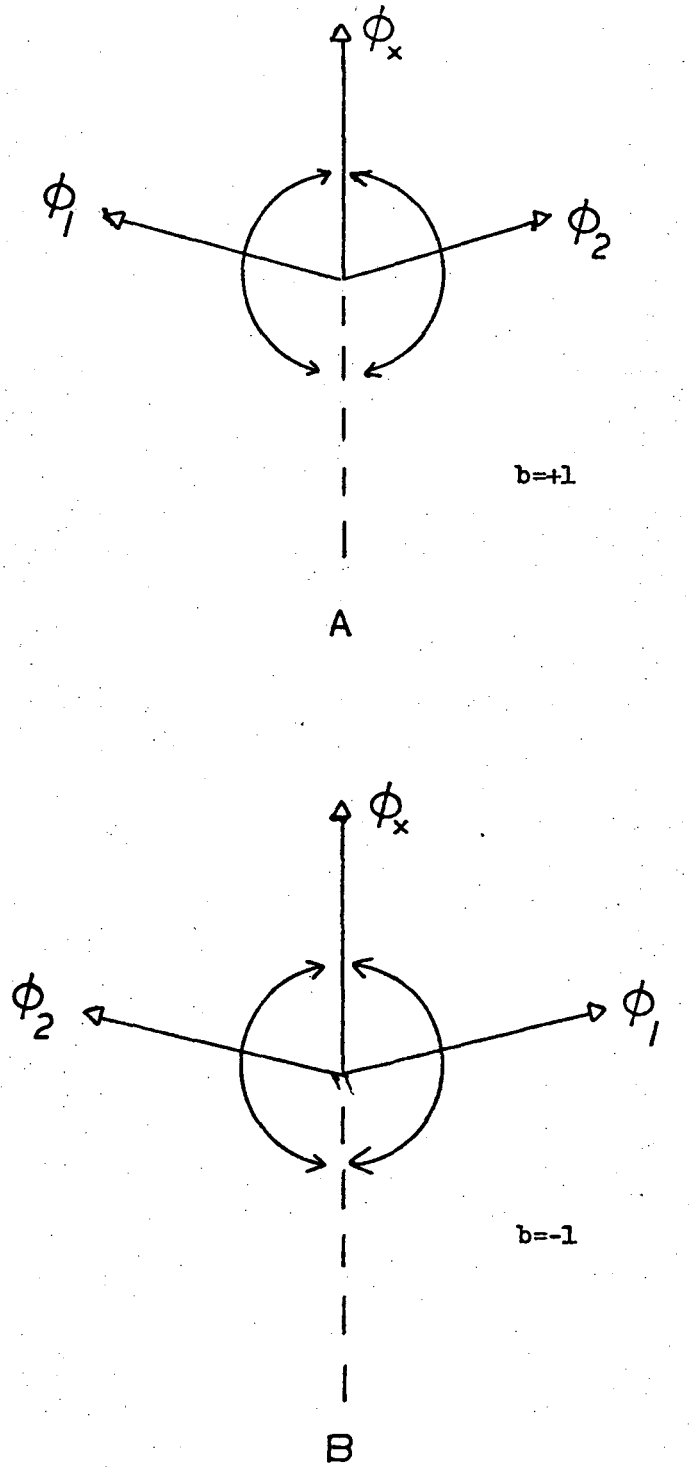

XBL 756-1726

Figure 32

1 and we can write:

$$\int_{-\pi}^{\pi} d\phi_1 \int_{-\pi}^{\pi} d\phi_2 = \frac{1}{J} \int_{-\pi}^{\pi} d\phi_x \sum_{b=\pm 1} \int_{-1}^{1} d\cos\psi$$

Since no other angles in ϕ have been chosen other than $\phi_1' = 0$ for the scattered electron, we have by parity symmetry:

$$\int_{-\pi}^{\pi} d\phi_1 \int_{-\pi}^{\pi} d\phi_2 = 2 \frac{1}{J} \int_{0}^{\pi} d\phi_x \sum_{b=\pm 1} \int_{-1}^{1} d\cos\psi$$

All that remains is to find the Jacobian J. As shown in Appendix A, $J = |\sin\psi|$ and the final expression becomes:

$$\int_{-\pi}^{\pi} d\phi_1 \int_{-\pi}^{\pi} d\phi_2 = 2 \int_{0}^{\pi} d\phi_x \sum_{b=\pm 1} \int_{0}^{\pi} d\psi$$

In the last step, we are free to choose $[0,\pi]$ or $[-\pi,0]$ for limits on ψ. However both give the same values for $\cos\psi$ which is the quantity used in calculating the matrix element, so the choice is arbitrary.

We now combine the results to get:

$$\sigma = \left(\frac{e^2}{(2\pi)^3}\right)^4 \frac{1}{E^2} (2\pi)^4 \frac{1}{4} \frac{1}{|\vec{V}_1 - \vec{V}_2|} \int_{m_p}^{\infty} dW_1 \int_{m_p}^{\infty} dW_2 \int_{-1}^{1} d\cos\theta_1 \int_{-1}^{1} d\cos\theta_2 \, |\vec{q}_1||\vec{q}_2|$$

$$\times \int_{-1}^{1} d\cos\theta_1' \int_{m_e}^{\infty} dE_1' \frac{2\pi}{|\vec{p}_x|} \int_{0}^{\pi} d\psi \int_{0}^{\pi} d\phi_x \, 2 \sum_{b=\pm 1} \delta(\cos\beta - \cos\theta_x \cos\theta_1' - \sin\theta_x \sin\theta_1' \cos\phi_x)$$

$$\times \theta(2E - W_1 - W_2 - E_1') \, D \frac{1}{(K_1^2 K_2^2)^2}$$

Finally we cancel the remaining delta function against the integral in ϕ_x. Since $\cos\phi_x$ is single valued in region $\phi_x = [0,\pi]$, we are left with

$$\int_{0}^{\pi} d\phi_x \, \delta(\cos\beta - \cos\theta_x \cos\theta_1' - \sin\theta_x \sin\theta_1' \cos\phi_x) = \theta(1 - |\cos\phi_x|) \frac{1}{\sin\theta_x \sin\theta_1' |\sin\phi_x|}$$

where

$$\cos\phi_x = \frac{\cos\beta - \cos\theta_x \cos\theta_1'}{\sin\theta_x \sin\theta_1'}$$

The maximum energy of the produced particles for an initial state $E_{TOT} = 2E, \vec{p}_{TOT} = 0$ is $E_{max} = E + (M_p^2 - M_T^2)/4E^2$ where M_p is the produced particles's mass and M_T is the invariant mass of the rest of the final state. Now $M_T > M_p$ so $E_{max} < E$ and we can replace ∞ by E as the upper limit in the integrations over W_1, W_2 and E_1'. Also using $|\vec{V}_1 - \vec{V}_2| = 2$ (good to 1 part in 10^8) we find for σ:

$$\sigma = \left(\frac{\alpha}{\pi}\right)^4 \frac{1}{E^2} \frac{\pi}{2} \int_{m_p}^{E} dW_1 \int_{m_p}^{E} dW_2 \int_{-1}^{1} d\cos\theta_1 \int_{-1}^{1} d\cos\theta_2 \int_0^{\pi} d\psi \int_{-1}^{1} d\cos\theta_1' \int_{m_e}^{E} dE_1'$$

$$\times\, \theta(1 - |\cos\phi_x|)\, \theta(2E - W_1 - W_2 - E_1') \frac{|\vec{q}_1|\,|\vec{q}_2|}{|\vec{p}_x| \sin\theta_x \sin\theta_1' |\sin\phi_x|} \sum_{b=\pm 1} \frac{D}{(K_1^2 K_2^2)^2}$$

where

$$|\vec{p}_x| = |\vec{q}_1 + \vec{q}_2|$$

$$\cos\theta_x = \frac{|\vec{q}_1| \cos\theta_1 + |\vec{q}_2| \cos\theta_2}{|\vec{p}_x|}$$

$$\cos\beta = \frac{(2E - E_x)^2 - \vec{p}_x^{\,2} - 2E_1'(2E - E_x)}{2\,|\vec{p}_1'|\,|\vec{p}_x|}$$

$$\cos\phi_x = \frac{\cos\beta - \cos\theta_1' \cos\theta_x}{\sin\theta_1' \sin\theta_x}$$

$$\phi_1 = \phi_x - b \cos^{-1}\left\{ \frac{\vec{q}_1^{\,2} \sin^2\theta_1 + \vec{p}_x^{\,2} \sin\theta_x - \vec{q}_2^{\,2} \sin^2\theta_2}{2\,|\vec{q}_1| \sin\theta_1\, |\vec{p}_x| \sin\theta_x} \right\}$$

$$\phi_2 = \phi_x + b \cos^{-1}\left\{ \frac{\vec{q}_2^{\,2} \sin^2\theta_2 + \vec{p}_x^{\,2} \sin\theta_x - \vec{q}_1^{\,2} \sin^2\theta_1}{2\,|\vec{q}_2| \sin\theta_2\, |\vec{p}_x| \sin\theta_x} \right\}$$

$$D = \frac{1}{4} \rho_1 \rho_1\, t^{\mu\nu}(p_1, k_1)\, M^{+}_{\mu\alpha} M_{\nu\beta}\, t^{\alpha\beta}(p_2, k_2)$$

(Formula F2)

b. Simplification of the Phase Space

The previous expression can be used in a numerical integration to calculate a cross section; however, the theta function $\theta(1 - |\cos\phi_x|)$ is very restrictive and eliminates a large fraction of the phase space, resulting in a prohibitive number of steps needed to obtain good accuracy. This situation can be improved by incorporating the theta function into the limits of integration on E_1' and θ_1'. This has been done in several different ways.

Brodsky et al.[12] use the following method: the theta function $(1 - |\cos\phi_x|)$ comes from imposing the limits of integration, $0 \le \phi_x \le \pi$, on the delta function $\delta(\cos\beta - \cos\theta_1'\cos\theta_x - \sin\theta_1'\sin\theta_x\cos\phi_x)$. This is equivalent to the requirement

$$\cos(\theta_1' + \theta_x) \le \cos\beta \le \cos(\theta_1' - \theta_x)$$

or

$$\cos(\theta_1' + \theta_x) \le \frac{A - B E_1'}{|\vec{p}_1'|} \le \cos(\theta_1' - \theta_x)$$

with

$$A = \frac{(2E - E_x)^2 - \vec{p}_x^{\,2}}{2\,|\vec{p}_x|} > \frac{2 m_e^2}{|\vec{p}_x|}$$

$$B = \frac{2E - E_x}{|\vec{p}_x|} > 1$$

They make the approximation $|\vec{p}_1'| \approx E_i$ and derive the limits

$$\frac{A}{B + \cos(\theta_1' - \theta_x)} \le E_1' \le \frac{A}{B + \cos(\theta_1' + \theta_x)}$$

resulting in

$$\sigma = \left(\frac{\alpha}{\pi}\right)^4 \frac{1}{E^2} \frac{\pi}{2} \int_{m_p}^{E} dW_1 \int_{m_p}^{E} dW_2 \int_{-1}^{1} d\cos\theta_1 \int_{-1}^{1} d\cos\theta_2 \int_0^{\pi} d\psi \int_{-}^{1} d\cos\theta_1' \int_{E_-}^{E_+} dE_1'$$

$$\times\ \theta(1-|\cos\phi_x|)\,\theta(2E-W_1-W_2-E_1')\,\frac{|\vec{g}_1|\,|\vec{g}_2|}{|\vec{p}_x|\sin\theta_x \sin\theta_1'|\sin\phi_x|} \sum_{b=\pm 1} \frac{D}{(K_1^2 K_2^2)^2}$$

where
$$E_- = \max\left\{\frac{A}{B+\cos(\theta_1'-\theta_x)},\ m_e\right\}$$
$$E_+ = \min\left\{\frac{A}{B+\cos(\theta_1'+\theta_x)},\ E\right\}$$

(Formula F 3)

Here, even though the phase space has been simplified, we keep the theta function in $\cos\phi_x$ because of the approximation made in deriving the limits. And still, there is some question as to whether part of the phase space has been accidentally eliminated through the approximation.

Grammer and Kinoshita[35] claim that the errors are ofthe order of 30% and simplify the phase space in a different way without approximation. Instead of applying the condition

$$\cos(\theta_1'+\theta_x) \leq \cos\beta = \frac{A-BE_1'}{|\vec{p}_1'|} \leq \cos(\theta_1'-\theta_x)$$

to the limits on E_1' <u>after</u> θ_1' has been chosen, they apply the looser condition

$$-1 \leq \cos\beta \leq 1$$

to E_1' <u>before</u> θ_1' has been chosen, and then apply the tighter limit to θ_1'. Their expression is

$$\sigma = \left(\frac{\alpha}{\pi}\right)^4 \frac{1}{E^2} \frac{\pi}{2} \int_{m_p}^{E} dW_1 \int_{m_p}^{E} dW_2 \int_{-1}^{1} d\cos\theta_1 \int_{-1}^{1} d\cos\theta_2 \int_0^{\pi} d\psi \int_{E_-}^{E_+} dE_1' \; \theta(C_+ - C_-)$$

$$\times \int_{C_-}^{C_+} d\cos\theta_1' \; \theta(2E - W_1 - W_2 - E_1') \frac{|\vec{q}_1| \; |\vec{q}_2|}{|\vec{p}_x| \sin\theta_x \sin\theta_1' |\sin\phi_x|} \sum_{b=\pm 1} \frac{D}{(K_1^2 K_2^2)^2}$$

where

$$E_- = \max\left\{ \frac{AB - \sqrt{A^2 - m_e^2 (B^2-1)}}{B^2-1} , m_e \right\}$$

$$E_+ = \min\left\{ \frac{AB + \sqrt{A^2 - m_e^2 (B^2-1)}}{B^2-1} , E \right\}$$

$$C_- = \cos(\beta + \theta_x)$$

$$C_+ = \cos(\beta - \theta_x)$$

(Formula F4)

This expression was derived without approximation.

As one can easily see, the theta function $\theta(C_+ - C_-) \equiv 1$ since $\cos(\beta + \theta_x) < \cos(\beta - \theta_x)$ for all β, θ_x where $0 < \beta < \pi$, $0 < \theta_x < \pi$. We were interested in calculating this integral for prescribed limits on θ_1' corresponding to our small angle electron detectors. This, however, puts additional restrictions on θ_1' and $C_\pm$ becomes

$$C_- = \max\{\cos(\beta + \theta_x), \cos(\theta_{1\,max}')\}$$

$$C_+ = \min\{\cos(\beta - \theta_x), \cos(\theta_{1\,min}')\}$$

No longer is $\theta(C_+ - C_-) \equiv 1$ and in particular for the limits

$$0 = \theta_1'{}_{min} \le \theta_1' \le \theta_1'{}_{max} = 5°$$

the theta function becomes as restrictive as the original $\theta(1 - |\cos\phi_x|)$ and the integral becomes very difficult. What happens is that for a large portion of the range on E_1', $(E_- \le E_1' \le E_+)$, $\theta(C_+ - C_-)$ vanishes and integration steps are wasted.

A third expression for the phase space was derived in hopes of combining the accuracy of the second method with the ease of integration of the first. The condition

$$\cos(\theta_1' + \theta_x) \leq \frac{A - BE_1'}{|\vec{p}_1'|} \leq \cos(\theta_1' - \theta_x)$$

was solved exactly, resulting in

$$\sigma = \left(\frac{\alpha}{\pi}\right)^4 \frac{1}{E^2} \frac{\pi}{2} \int_{m_\rho}^{E} dW_1 \int_{m_\rho}^{E} dW_2 \int_{-1}^{1} d\cos\theta_1 \int_{-1}^{1} d\cos\theta_2 \int_0^{\pi} d\psi \int_{-1}^{1} d\cos\theta_1' \int_{E_-}^{E_+} dE_1'$$

$$\times\, \theta(1 - |\cos\phi_x|)\, \theta(2E - W_1 - W_2 - E_1') \frac{|\vec{q}_1|\,|\vec{q}_2|}{|\vec{p}_x| \sin\theta_x \sin\theta_1' |\sin\phi_x|} \sum_{b=\pm 1} \frac{D}{(K_1^2 K_2^2)^2}$$

where

$$E_- = \max\left\{ \frac{AB - \cos(\theta_1' - \theta_x)\sqrt{A^2 - m_e^2(B^2 - \cos^2(\theta_1' - \theta_x))}}{B^2 - \cos^2(\theta_1' - \theta_x)},\ m_e \right\}$$

$$E_+ = \min\left\{ \frac{AB - \cos(\theta_1' + \theta_x)\sqrt{A^2 - m_e^2(B^2 - \cos^2(\theta_1' + \theta_x))}}{B^2 - \cos^2(\theta_1' + \theta_x)},\ E \right\}$$

(Formula F5)

If the expression under the square root is less than zero in the formulae for E_+ and E_-, we must use $E_+ = E$ or $E_- = M_e$ for the limits, which is why $\theta(1 - |\cos\phi_x|)$ was left in the integral.

c. Calculation of the Matrix Element

The matrix element D can be calculated in QED for either bosons or fermions. In the case of bosons we can find only a rough approximation for the cross section for $e^+e^- \to e^+e^-\pi^+\pi^-$ since the pion interacts strongly. In the case of fermions we can calculate exactly the processes $e^+e^- \to e^+e^-e^+e^-$ and $e^+e^- \to e^+e^-\mu^+\mu^-$.

For bosons, diagrams a, b, and c of Fig. 33 give

$$|M_{\nu\beta}| = \frac{b_{1\nu}\, b_{3\beta}}{p_a} + \frac{b_{2\nu}\, b_{4\beta}}{p_b} + 2\, g_{\nu\beta}$$

with

$$b_{1\nu} = K_{1\nu} - 2\, q_{1\nu} \qquad b_{2\nu} = K_{1\nu} - 2\, q_{2\nu}$$

$$b_{3\beta} = K_{1\beta} - q_{1\beta} + q_{2\beta} \qquad b_{4\beta} = K_{1\beta} + q_{1\beta} - q_{2\beta}$$

$$p_a = 2\, K_1 \cdot q_1 - K_1^2 \qquad p_b = 2\, K_1 \cdot q_2 - K_1^2$$

and

$$\rho_1 = \rho_2 = 1$$

$$\frac{1}{4}\, t^{\mu\nu}(p_1, K_1)\, t^{\alpha\beta}(p_2, K_2) = \left(p_1^{\mu} p_1^{\nu} + \frac{1}{4} g^{\mu\nu} K_1^2\right)\left(p_2^{\alpha} p_2^{\beta} + \frac{1}{4} g^{\alpha\beta} K_2^2\right)$$

giving

$$D = \left(2\, p_1 \cdot p_2 + \frac{(b_1 \cdot p_1)(b_3 \cdot p_2)}{p_a} + \frac{(b_2 \cdot p_1)(b_4 \cdot p_2)}{p_b}\right)^2$$

$$+ \frac{K_1^2}{4}\left(2 p_2 + \frac{(b_3 \cdot p_2)\, b_1}{p_a} + \frac{(b_4 \cdot p_2)\, b_2}{p_b}\right)^2$$

$$+ \frac{K_2^2}{4}\left(2 p_1 + \frac{(b_1 \cdot p_1)\, b_3}{p_a} + \frac{(b_2 \cdot p_1)\, b_4}{p_b}\right)^2$$

$$+ \frac{K_1^2 K_2^2}{16}\left(16 + \frac{4\, b_1 \cdot b_3}{p_a} + \frac{4\, b_2 \cdot b_4}{p_b} + \frac{b_1^2\, b_3^2}{p_a^2} + \frac{b_2^2\, b_4^2}{p_b^2} + 2\, \frac{(b_1 \cdot b_2)(b_3 \cdot b_4)}{p_a\, p_b}\right)$$

For fermions, only diagrams a and b of Fig. 33 contribute to give

$$|M_{\nu\beta}| = \bar{V}(q_2)\left[\gamma_\beta \frac{\not{q}_1 - \not{K}_1 + m_p}{(q_1 - K_1)^2 - m_p^2}\gamma_\nu + \gamma_\nu \frac{\not{K}_1 - \not{q}_2 + m_p}{(K_1 - q_2)^2 - m_p^2}\gamma_\beta\right] u(q_1)$$

$$= -\bar{V}(q_2)\left[\frac{1}{p_a}\gamma_\beta\,(2 q_{1\nu} - \not{K}_1 \gamma_\nu) + \frac{1}{p_b}(\gamma_\nu \not{K}_1 - 2 q_{2\nu})\gamma_\beta\right] u(q_1)$$

DIAGRAMS IN $|M|^2$

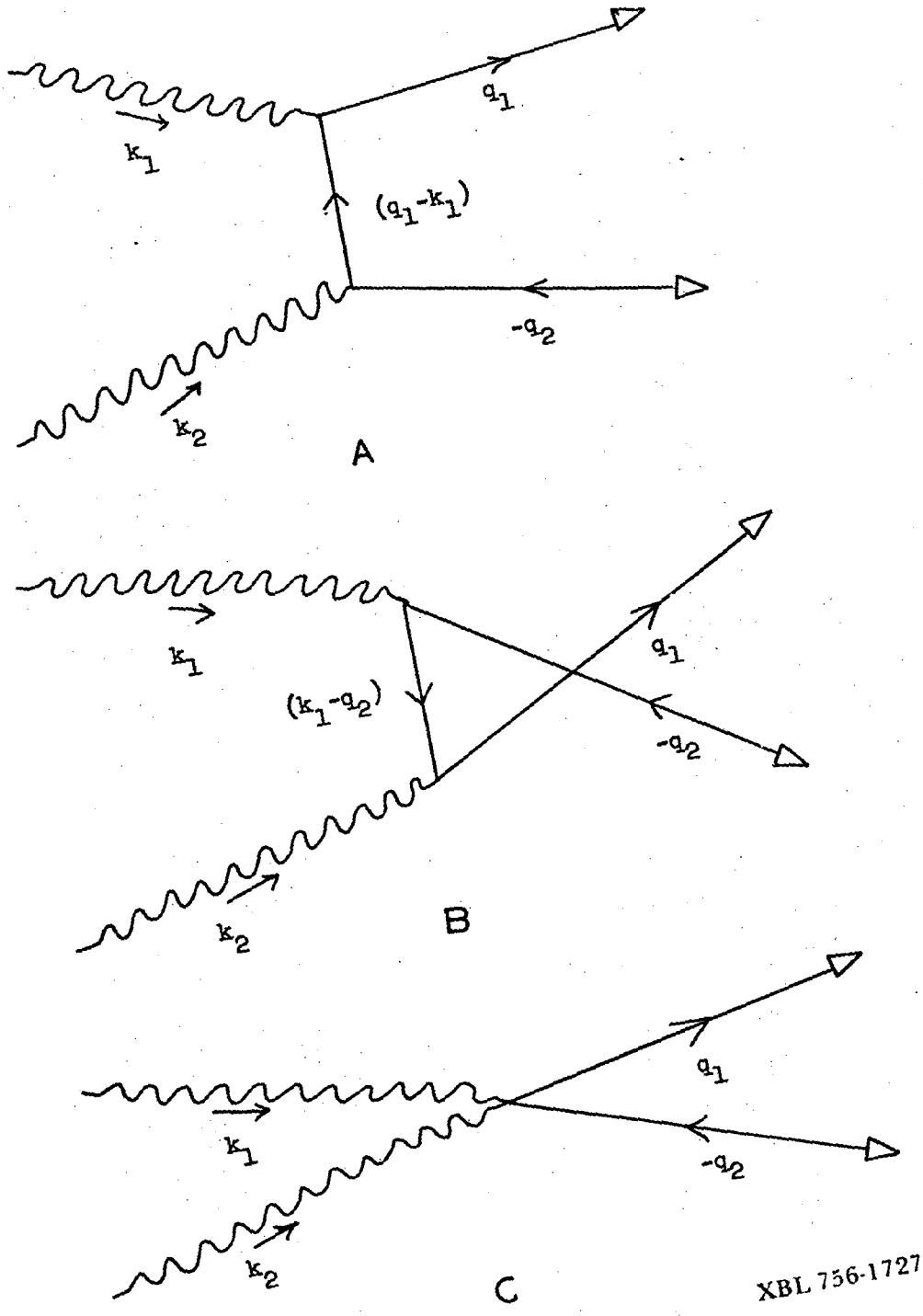

Figure 33

$$\rho_1 = \rho_2 = 2 m_\rho$$

Then

$$D = \frac{1}{4} \rho_1 \rho_2 t^{\mu\nu}(p_1, k_1) M^{+}_{\mu\alpha} M_{\nu\beta} t^{\alpha\beta}(p_2, k_2)$$

$$= \frac{A_1}{p_a^2} + \frac{A_2}{p_b^2} + \frac{2 A_{12}}{p_a p_b}$$

with

$$A_1 = t^{\mu\nu}(p_1, k_1) t^{\alpha\beta}(p_2, k_2) \frac{1}{4} \mathrm{Tr} \{ (-\not{q}_2 + m_\rho) \gamma_\beta (2 q_{1\nu} - \not{k}_1 \gamma_\nu) (\not{q}_1 + m_\rho) (2 q_{1\mu} - \gamma_\mu \not{k}_1) \gamma_\alpha \}$$

$$A_2 = t^{\mu\nu}(p_1, k_1) t^{\alpha\beta}(p_2, k_2) \frac{1}{4} \mathrm{Tr} \{ (-\not{q}_2 + m_\rho) (\gamma_\nu \not{k}_1 - 2 q_{2\nu}) \gamma_\beta (\not{q}_1 + m_\rho) \gamma_\alpha (\not{k}_1 \gamma_\mu - 2 q_{2\mu}) \}$$

$$A_{12} = t^{\mu\nu}(p_1, k_1) t^{\alpha\beta}(p_2, k_2) \frac{1}{8} \mathrm{Tr} \{ (-\not{q}_2 + m_\rho) \gamma_\beta (2 q_{1\nu} - \not{k}_1 \gamma_\nu) (\not{q}_1 + m_\rho) \gamma_\alpha (\not{k}_1 \gamma_\mu - 2 q_{2\mu}) \}$$

$$+ t^{\mu\nu}(p_1, k_1) t^{\alpha\beta}(p_2, k_2) \frac{1}{8} \mathrm{Tr} \{ (-\not{q}_2 + m_\rho) (\gamma_\nu \not{k}_1 - 2 q_{2\nu}) \gamma_\beta (\not{q}_1 + m_\rho) (2 q_{1\mu} - \gamma_\mu \not{k}_1) \gamma_\alpha \}$$

These traces have been worked out by Grammer and Kinoshita[35] and we quote their result here:

$$
\begin{aligned}
A_1 = {} & 32 p_1\cdot q_1\, p_2\cdot q_2 (k_1\cdot q_1\, p_1\cdot p_2 - k_1\cdot p_2\, p_1\cdot q_1 + p_1\cdot q_1\, p_2\cdot q_1) \\
& - 8k_1^2 p_2\cdot q_2 (k_1\cdot q_1\, k_1\cdot p_2 - 2k_1\cdot p_2\, p_1\cdot q_1 + 2p_2\cdot q_1\, p_1\cdot q_1 \\
& \qquad + 2p_1\cdot q_1\, p_1\cdot p_2) \\
& + 8k_2^2 p_1\cdot q_1 (k_1\cdot q_2\, p_1\cdot q_1 - k_1\cdot q_1\, p_1\cdot q_2 - q_1\cdot q_2\, p_1\cdot q_1) \\
& + 8M^2 k_1^2 (p_2\cdot q_1\, p_2\cdot q_2 - k_1\cdot p_2\, p_2\cdot q_2) - 4m^4 k_1^2 q_1\cdot q_2 \\
& + 4m^2 M^2 k_1^2 (k_1\cdot q_1 + k_1\cdot q_2 - q_1\cdot q_2 + 2p_1\cdot q_1 - M^2 - m^2) \\
& + 4m^2 k_1^2 (k_1\cdot q_1\, k_1\cdot q_2 - 2p_1\cdot q_1\, k_1\cdot q_2 + 2q_1\cdot q_2\, p_1\cdot q_1 \\
& \qquad + 2p_2\cdot q_1\, p_2\cdot q_2 + 2p_1\cdot q_1\, p_1\cdot q_2) \\
& - 4k_2^2 (4M^2 (p_1\cdot q_1)^2 - m^2 k_1\cdot q_1\, k_1\cdot q_2) \\
& + 2k_1^4 (2p_2\cdot q_1\, p_2\cdot q_2 - m^2 q_1\cdot q_2 - 2m^2 M^2) \\
& + 2k_1^2 k_2^2 (k_1\cdot q_1\, k_1\cdot q_2 - 2k_1\cdot q_2\, p_1\cdot q_1 + 2q_1\cdot q_2\, p_1\cdot q_1 \\
& \qquad + 2p_1\cdot q_1\, p_1\cdot q_2 - m^2 q_1\cdot q_2) \\
& + 2k_1^2 k_2^2 M^2 (k_1\cdot q_2 + 2k_1\cdot q_1 - q_1\cdot q_2 + 4p_1\cdot q_1 - 2M^2 - 2m^2) \\
& - k_1^4 k_2^2 (4M^2 + q_1\cdot q_2) - 16m^2 M^2 (p_1\cdot q_1)^2 \\
& + 8m^4 k_1\cdot q_1\, k_1\cdot q_2 + 16m^2 (p_1\cdot q_1)^2 (k_1\cdot q_2 - q_1\cdot q_2) \\
& - 16m^2 k_1\cdot q_1 (k_1\cdot p_2\, p_2\cdot q_2 + p_1\cdot q_1\, p_1\cdot q_2)
\end{aligned}
$$

$$A_2 = A_1(q_1 \longleftrightarrow q_2)$$

XBL 757-1776

$$
\begin{aligned}
A_{12} = {} & 16k_1\cdot q_2\ p_1\cdot p_2\ p_1\cdot q_1(p_2\cdot k_1 - p_2\cdot q_1) \\
& + 8k_1\cdot p_2\ p_1\cdot q_2\ p_1\cdot q_1(2p_2\cdot q_1 - k_1\cdot p_2) \\
& - 8(p_1\cdot p_2)^2 k_1\cdot q_1\ k_1\cdot q_2 - 16p_1\cdot q_1\ p_2\cdot q_1\ p_1\cdot q_2\ p_2\cdot q_2 \\
& + 4k_2^2 p_1\cdot q_1(k_1\cdot q_2\ p_1\cdot q_1 + p_1\cdot q_2\ q_1\cdot q_2 - p_1\cdot q_2\ k_1\cdot q_1 + 2M^2\cdot p_1\cdot q_2) \\
& + 2M^2 k_1^2((k_1\cdot p_2)^2 - 2k_1\cdot p_2\ p_1\cdot p_2 + 2(p_1\cdot p_2)^2) \\
& + 2m^2M^2k_1^2(q_1\cdot q_2 - 2p_1\cdot q_1 - m^2) \\
& + 2m^2k_1^2 q_1\cdot q_2(q_1\cdot q_2 - 2k_1\cdot q_1 - m^2) \\
& + 4m^2k_1^2 p_1\cdot q_1(p_1\cdot q_2 - q_1\cdot q_2 - k_1\cdot q_2) \\
& + k_1^4(m^2M^2 + 2m^2 q_1\cdot q_2 - 2p_2\cdot q_1\ p_2\cdot q_2) \\
& + 4k_1^2 p_2\cdot q_1\ p_2\cdot q_2(k_1\cdot q_1 - q_1\cdot q_2 + 2p_1\cdot q_1 + m^2) \\
& + 4k_1^2 p_2\cdot q_1\ k_1\cdot q_2(2p_1\cdot p_2 - p_2\cdot q_1) \\
& + 4k_1^2 k_1\cdot p_2\ q_1\cdot q_2(p_2\cdot q_1 - p_1\cdot p_2) \\
& + 4k_1^2 p_1\cdot p_2(p_1\cdot p_2\ q_1\cdot q_2 - 2p_2\cdot q_1\ p_1\cdot q_2) \\
& + 4m^2M^2((k_1\cdot p_2)^2 + 2p_1\cdot q_1\ p_1\cdot q_2) \\
& + 8m^2 p_1\cdot q_1\ p_1\cdot q_2(q_1\cdot q_2 - k_1\cdot q_1) + 8m^2 k_1\cdot q_2(p_1\cdot q_1)^2 \\
& + 4m^2 k_1\cdot p_2(k_1\cdot p_2\ q_1\cdot q_2 - 2k_1\cdot q_2\ p_2\cdot q_1) \\
& + 4m^4 k_1\cdot q_1\ k_1\cdot q_2 \\
& + k_1^2k_2^2\ q_1\cdot q_2(q_1\cdot q_2 - 2k_1\cdot q_1 - 2p_1\cdot q_1 + 2M^2 + m^2) \\
& \qquad - M^2k_1^2k_2^2(k_1\cdot q_1 + 4p_1\cdot q_1) \\
& + k_1^4k_2^2(q_1\cdot q_2 + M^2) \\
& + (q_1 \leftrightarrow q_2)
\end{aligned}
$$

3. The Numerical Integration

The cross sections of the previous section have been integrated numerically in order to determine the expected two-photon event rate. They were calculated on the SLAC IBM 370 computer system using double precision and Monte Carlo integration techniques.

The difficult problem of peaks in the integrand was alleviated in two ways. First the cuts of the SPEAR detector were imposed cutting out the worst of the peaked regions. With detector cuts, the integration ranges were:

$$\sqrt{(225\ \mathrm{MeV})^2 + M_p{}^2C^4} < W_1 < E$$

$$\sqrt{(225\ \mathrm{MeV})^2 + M_p{}^2C^4} < W_2 < E$$

$$-0.6 < \cos\theta_1 < 0.6$$

$$-0.6 < \cos\theta_2 < 0.6$$

$$M_e < E_1' < E$$

$$0° < \theta_1' < 49.6°$$

$$0° < \psi < 180°.$$

Second, integration factors were substituted for the variables W_1, W_2, and θ_1' to make the integrand flatter. The substitutions were:

$$W_{1,2} \rightarrow W_{min} + (W_{max} - W_{min})\ (e^{Z_{1,2}} - 1)$$

$$\int_{W_{min}}^{W_{max}} dW_{1,2} \rightarrow \int_0^{\ln 2} (W_{max} - W_{min})\ e^{Z_{1,2}}\ dZ_{1,2}$$

$$\theta_1' \rightarrow \theta'_{min} + (\theta'_{max} - \theta'_{min})\ \epsilon \left\{\left(\frac{1+\epsilon}{\epsilon}\right)^Y - 1\right\}$$

$$\int_{\theta'_{min}}^{\theta'_{max}} d\theta_1' \rightarrow \int_0^1 (\theta'_{max} - \theta'_{min})\ \epsilon \ln\left(\frac{1+\epsilon}{\epsilon}\right) \left(\frac{1+\epsilon}{\epsilon}\right)^Y dY$$

where

$$\epsilon = \text{some small constant.}$$

For each cross section, $d\sigma/d\psi$ was calculated at 20 different values of ψ, 8 between 0° and 20° and 12 between 20° and 180°. At each value of ψ, the other variables were chosen in Monte Carlo fashion with $N = 2 \times 10^5$ tosses. The cross section was then computed as

$$\sigma = \frac{1}{N} \sum_{i=1}^{N} \sigma_i .$$

The error in the computed cross section was also calculated as the standard deviation of the mean[38]

$$(\Delta\sigma)^2 = \frac{1}{N^2} \sum_{i=1}^{N} \sigma_i^2 - \frac{1}{N^3} \left(\sum_{i=1}^{N} \sigma_i \right)^2 .$$

The final integration over ψ was done in a piecewise fashion over a smooth curve drawn between the points.

We proceeded to compare the different phase space methods outlined in the last section: 1) the BKT method, formula F3 2) The GK method, formula F4 , 3) the BKT (corrected) method, formula F5 , and 4) the CRUDE method, formula F2 . The first conclusion we drew was that BKT and BKT (corrected) integrations gave identical results contradicting, at least in our range of integration, the claim of Grammer and Kinoshita[35] that the error in BKT could be as large as 30%. The choice seemed to be between the BKT method and the GK method. Figs. 34 and 35 show the results for $d\sigma/d\psi(e^+e^- \to e^+e^-\mu^+\mu^-)$ at 2.4 GeV for the BKT and GK methods respectively. As can be seen, the cross sections are

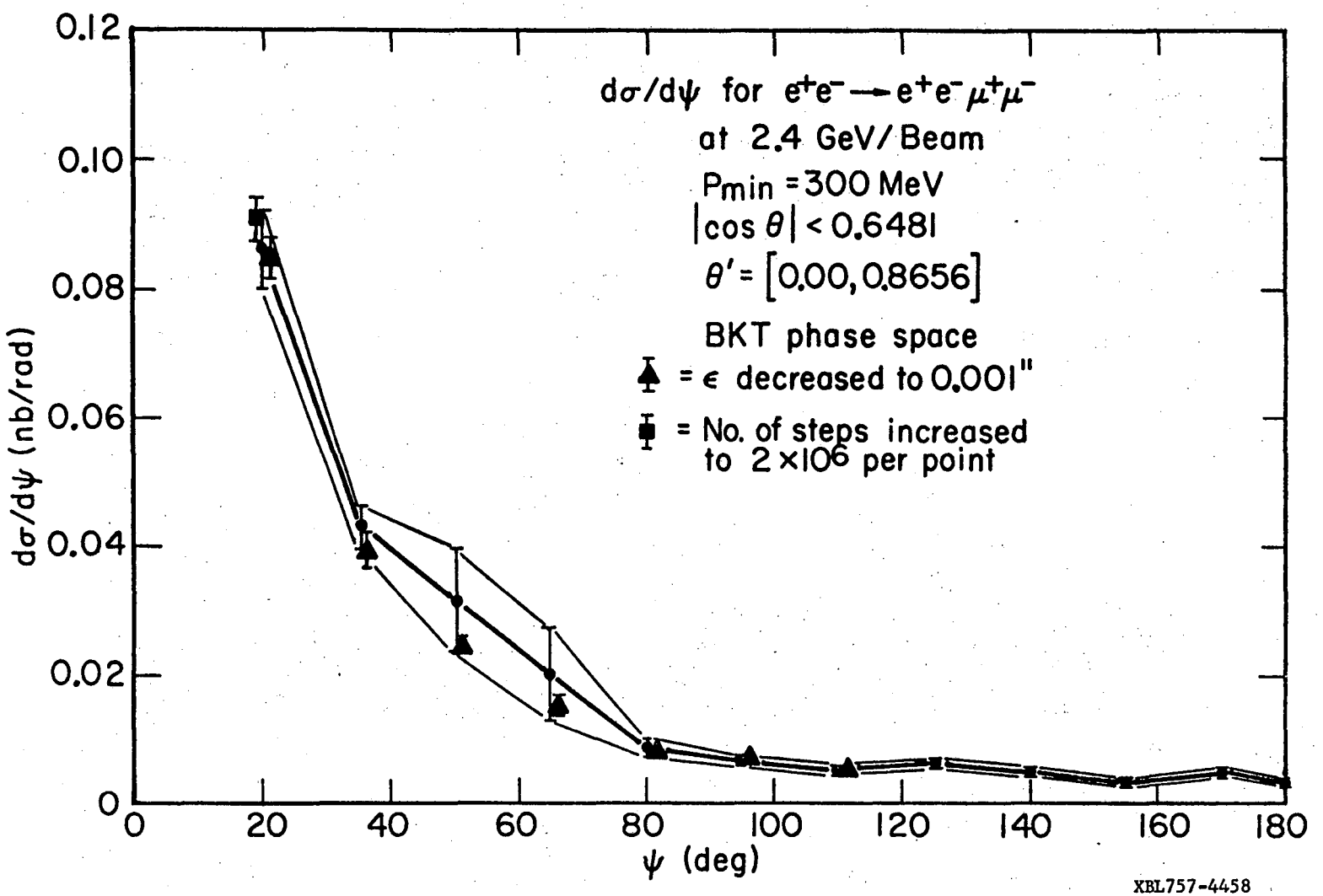
dσ/dψ for e⁺e⁻ → e⁺e⁻μ⁺μ⁻
at 2.4 GeV/Beam
Pmin = 300 MeV
|cos θ| < 0.6481
θ' = [0.00, 0.8656]
BKT phase space
= ε decreased to 0.001"
= No. of steps increased to 2×10⁶ per point
dσ/dψ (nb/rad)
ψ (deg)
0.12
0.10
0.08
0.06
0.04
0.02
0
0
20
40
60
80
100
120
140
160
180
XBL757-4458

Figure 34

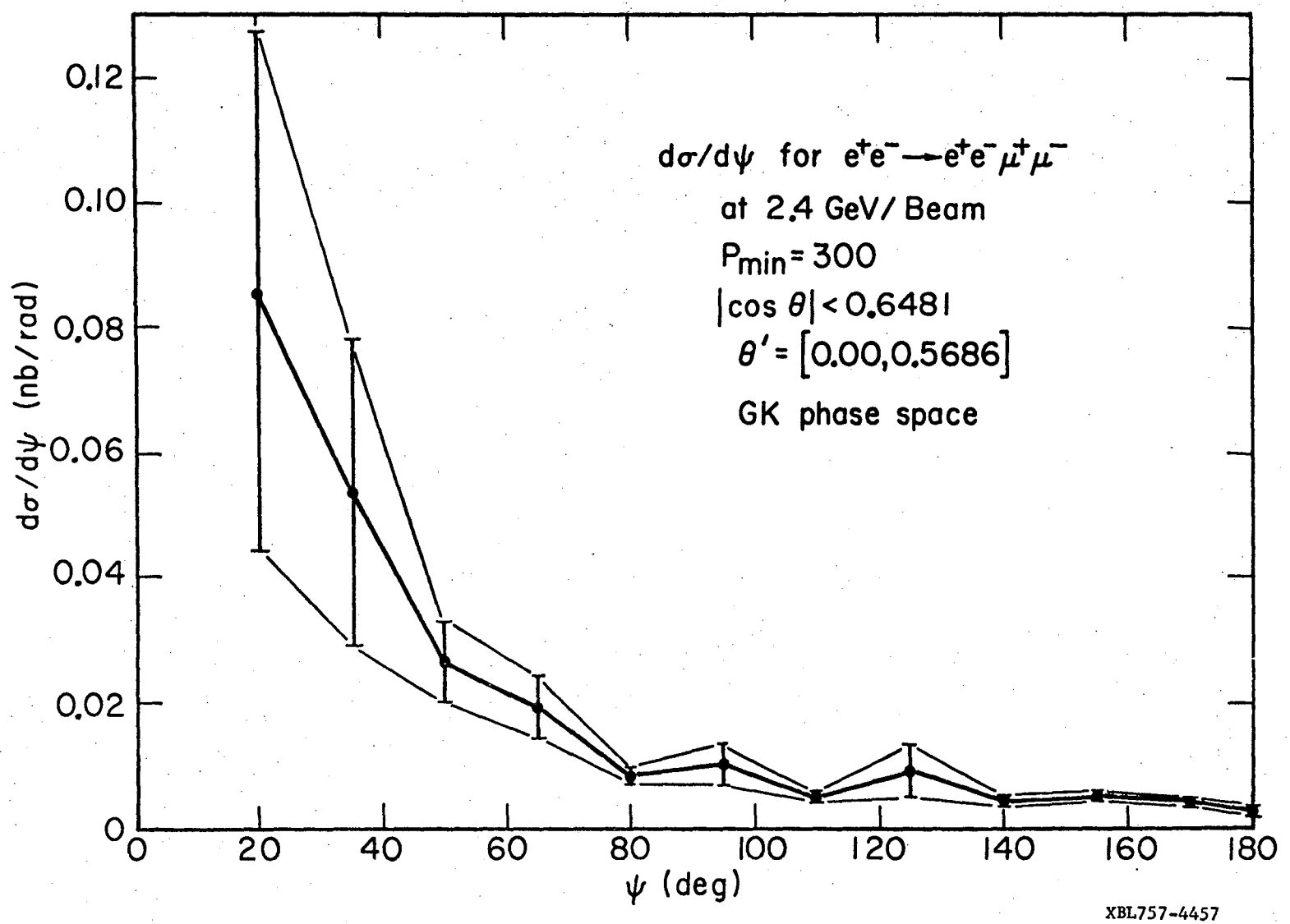
dσ/dψ for e⁺e⁻ → e⁺e⁻μ⁺μ⁻
at 2.4 GeV/ Beam
Pmin = 300
|cos θ| < 0.6481
θ′ = [0.00,0.5686]
GK phase space
dσ/dψ (nb/rad)
ψ (deg)
0
0.02
0.04
0.06
0.08
0.10
0.12
0
20
40
60
80
100
120
140
160
180
XBL757-4457

Figure 35

comparable, but the errors in the GK method become increasingly large as coplanarity approaches zero. For this reason, we chose the BKT method to do the exact calculations that follow.

The next problem was dealing with the peak in the integrand as $\theta' \to 0$. The extent of the problem is shown in Fig. 36 , a plot of $d\sigma/d\psi d\cos\theta'$ vs. ψ for various values of the angle θ'. As can be seen, the integrand is very peaked in θ' for all ψ and uniformly peaked in the region $\psi > 20°$. When integrating in the region $\psi > 20°$ the integrand was simply flattened by using the integrating factor described. ϵ was varied to assure that there was no dependence on its choice. The cross section stabilized at $\epsilon = .001$ and this value was used for the region $\psi > 20°$. In Fig. 34 the values of $d\sigma/d\psi$ are plotted for $\epsilon = .0001$ as well as $\epsilon = .001$ for comparison.

As can be inferred from Fig. 34 , the situation becomes much worse for smaller and smaller values of ψ, for the integrand is even more peaked in θ'. $d\sigma/d\psi$ was calculated down to $\psi = 0.1°$ but the integral became somewhat unstable with varying ϵ for $\psi < 2°$, and we feel less confident of the results in this region. (See section V-D5.)

In Table 5 we show the results for $e^+e^- \to e^+e^-e^+e^-(C = +)$, $e^+e^- \to e^+e^-\mu^+\mu^-(C = +)$ and $e^+e^- \to e^+e^-\pi^+\pi^-(C = +)$ (pointlike) for three different ranges of coplanarity ($\psi = 0°$ corresponds to oppositely directed particles in x-y space). Also in Table 6 we show similar results, except for "tagged events," that is where we have required at least one scattered electron to be detected in the small angle counters. All of these results have been corrected for shower counter inefficiency as discussed in section II-E and the

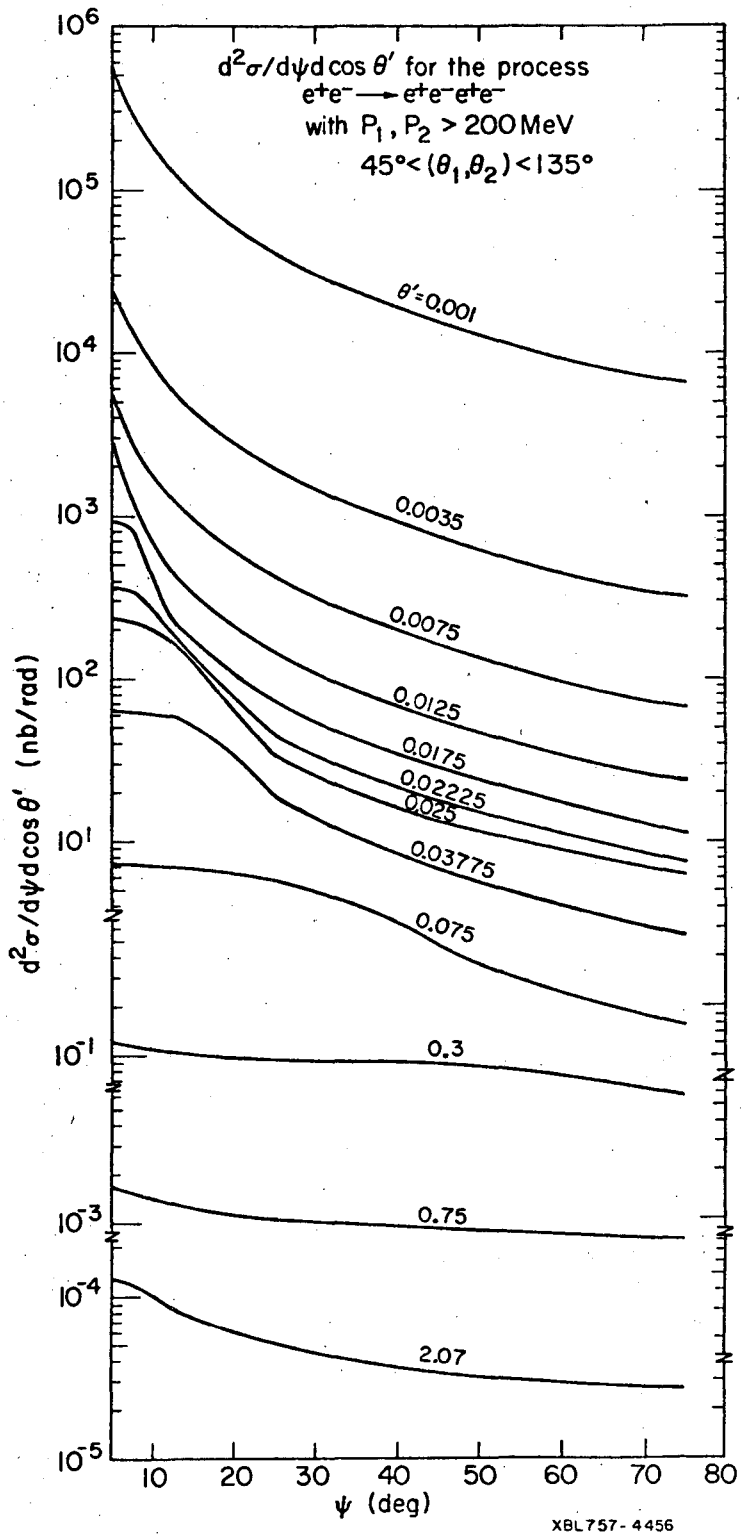
$d^2\sigma/d\psi d\cos\theta'$ for the process
$e^+e^- \rightarrow e^+e^-e^+e^-$
with $P_1, P_2 > 200$ MeV
$45° < (\theta_1, \theta_2) < 135°$
$\theta' = 0.001$
0.0035
0.0075
0.0125
0.0175
0.02225
0.025
0.03775
0.075
0.3
0.75
2.07
$d^2\sigma/d\psi d\cos\theta'$ (nb/rad)
ψ (deg)
XBL757-4456

Figure 36

σ_{EFF} For $e^+e^- \to e^+e^-A^+A^-$ at E=2.4 GeV/Beam

With $|\cos\theta_i| < 0.6$, $p_i > .225$ GeV/c

And .76±.08 Detection Efficiency

Exact Calculation (nanobarns)	$0° < \Psi < 20°$	$20° < \Psi < 160°$	$160° < \Psi < 180°$	$0° < \Psi < 180°$
e^+e^-(C=+)	.314±.047	.070±.010	.002±.0003	.387±.048
e^+e^-(C=-)	.003±.0003	.003±.0003	.007±.0007	.013±.0010
u^+u^-(C=+)	.245±.036	.058±.009	.002±.0002	.304±.037
$\pi^+\pi^-$(C=+) (pointlike)	.049±.007	.016±.002	.00055± .00008	.066±.008

WeizackerWilliams Calculation (nanobarns)				
e^+e^-(C=+)	-	-	-	.528±.056
u^+u^-(C=+)	-	-	-	.428±.045
$\pi^+\pi^-$(C=+) (pointlike)	-	-	-	.089±.009

Table 5

σ_{EFF} For $e^+e^- \to e^+e^-A^+A^-$ at E=2.4 GeV/Beam

With $|\cos\theta_i| < 0.6$, $p_i > .225$ GeV/c

And .76±.08 Detection Efficiency

One Scattered Electron "Tagged"

Exact Calculation (picobarns)	$0° < \Psi < 20°$	$20° < \Psi < 160°$	$160° < \Psi < 180°$	$0° < \Psi < 180°$
e^+e^-(C=+)	14.5±2.2	2.78±.31	.084±.009	17.4±2.3
e^+e^-(C=-)	.21±.02	.13±.02	.32±.03	.66±.04
u^+u^-(C=+)	13.2±2.0	2.14±.24	.063±.007	15.4±2.1
$\pi^+\pi^-$(C=+) (pointlike)	3.14±.47	.66±.07	.021±.002	3.82±.48

WeizackerWilliams Calculation (picobarns)				
e^+e^-(C=+)	-	-	-	25.0±2.6
u^+u^-(C=+)	-	-	-	20.3±2.2
$\pi^+\pi^-$(C=+) (pointlike)	-	-	-	4.28±.45

Table 6

8% of 2π azimuth obstructed by spark chamber support posts. The differential cross section, $d\sigma/d\psi$, was calculated for several values of ψ and the integration over ψ done by hand. In the region $0° < \psi < 1°$, a log-log plot was used to do the integration over ψ. Later we will compare these results to the data.

4. Comparison with the Equivalent Photon Method

Now that we have exactly calculated the fourth order cross sections, it will be of some interest to see how good the equivalent photon method does at approximating these cross sections with our detector cutoffs. To derive a suitable expression we start with equation F1 and apply the equivalent photon approximation to each photon. This approximation assumes the photon is emitted in the forward direction and is transversely polarized. This gives for the first photon:

$$\left(\frac{e^2}{(2\pi)^3}\right) \int \frac{d^3p_1'}{EE_1'} \left(\frac{1}{K_1^2}\right)^2 t^{\mu\nu}(p_1,K_1) M^+_{\mu\alpha} M_{\nu\beta}$$

$$\simeq \left(\frac{e^2}{(2\pi)^3}\right) \int \frac{d^3p_1'}{EE_1'} \left(\frac{1}{K_1^2}\right)^2 \left(-\frac{1}{2} K_1^2 + \frac{E^2E_1'^2}{\vec{K}_1^2} \sin^2\theta_1'\right) M^+_{\mu\alpha} M_{\nu\beta}$$

$$= \int \frac{d\omega_1}{\omega_1} \frac{1}{2\omega_1} N(\omega_1) M^+_{\mu\alpha} M_{\nu\beta}$$

where

$$N(\omega_1) = \frac{\alpha}{\pi} \left[\frac{E^2 + E_1'^2}{E^2} \left(\ln \frac{E}{m_e} - \frac{1}{2}\right) + \frac{(E - E_1')^2}{2E^2} \left(\ln \frac{2E_1'}{E - E_1'} + 1\right) + \frac{(E + E_1')^2}{2E^2} \ln \frac{2E_1'}{E + E_1'} \right].$$

When it is applied to both photons we get

$$\sigma_{ee}^{(0)}(E) = \left(\frac{e^2}{(2\pi)^3}\right)^2 \frac{1}{|\vec{V}_1 - \vec{V}_2|} \int \frac{d^3q_1}{2\omega_1} \int \frac{d^3q_2}{2\omega_2} \int \frac{d\omega_1}{\omega_1} \int \frac{d\omega_2}{\omega_2}$$

$$\times \frac{1}{2\omega_1} \frac{1}{2\omega_2} N(\omega_1)\, N(\omega_2)\, (2\pi)^4\, \delta^4\, (K_k + K_2 - q_1 - q_2)$$

$$\times \frac{1}{4} \rho_1 \rho_2\, M^+_{\mu\nu}\, M_{\mu\nu}$$

$$= \int_0^E \frac{d\omega_1}{\omega_1} \int_0^E \frac{d\omega_2}{\omega_2}\, N(\omega_1)\, N(\omega_2)\, \sigma_{\gamma\gamma}\, (\omega_1, \omega_2)$$

where we have set $\frac{1}{|\vec{V}_1 - \vec{V}_2|} = \frac{1}{2}$, and $\sigma_{\gamma\gamma}(\omega_1, \omega_2)$ is the cross section for the two photons to produce the final state.

It is important to notice here that we have assumed the photons have zero mass and travel forward, and we have averaged over the azimuthal angles of the electrons eliminating one degree of freedom, but in the process losing all information about coplanarity of the produced particles. In this approximation, we require the produced particles to have zero total transverse momentum.

As derived in appendix B, the result of plugging in $\sigma_{\gamma\gamma}$ gives:

$$d\sigma_{ee}^{(0)}(E) = \int_0^\pi d\theta_1 \int_0^\pi d\theta_2 \int_{4m^2}^{4E^2} \frac{ds}{s}\, 2\pi\alpha^2\, \frac{|\vec{q}_1| \sin\theta_1 |\vec{q}_1|\ |\vec{q}_2| \sin(\theta_1+\theta_2)}{|q|\,[\omega W_1 \sin^2\theta_1 + \omega W_2 \sin^2\theta_2 - W_1 W_2 \sin^2(\theta_1+\theta}$$

$$\times\ \theta\left[\left(E + \frac{s}{4E}\right)^2 - q^2\right] N(\omega_1) N(\omega_2) G(W_1, \theta_1)$$

where $\omega = \omega_1 + \omega_2$ $\quad q = \omega_1 - \omega_2$

and $G(W_1, \theta_1) = \frac{1}{8} \rho_1 \rho_2\, |M_{\gamma\gamma}|^2.$

Using this formula and detector cutoffs of

$$4(225\ \text{MeV})^2 + 4m_p^2C^4 < S < 4E^2$$

$$-0.6 < \cos\theta_1 < 0.6$$

$$-0.6 < \cos\theta_2 < 0.6$$

$$225\ \text{MeV/c} < q_1 < E/c$$

$$225\ \text{MeV/c} < q_2 < E/c$$

we calculated an equivalent photon expression to compare with the exact calculation. Again a Monte Carlo integration was done with 200,000 steps and is given with calculational errors in Table 5.

The formula for events "tagged" by at least one small angle counter is found by replacing

$$N(\omega_1)N(\omega_2) \rightarrow N(\omega_1)\ N'(\omega_2,\theta'_{min},\theta'_{max}) + N'(\omega_1,\theta'_{min},\theta'_{max})\ N(\omega_2)$$

where

$$N'(\omega_1,\theta'_{min},\theta'_{max}) = \frac{\alpha}{\pi}\ \frac{E^2+E_1'^2}{2E^2}\ \ln\frac{1+\cos(\theta_{max})}{1+\cos(\theta_{min})}$$

$$+ \frac{(E + E_1')^2}{4E^2}\ \ln\frac{E^2 + E_1'^2 - 2EE_1'\cos\theta_{min}}{E^2 + E_1'^2 - 2EE_1'\cos\theta_{max}}$$

where $\theta_{min} = 0.02$ rad $\theta_{max} = 0.03$ rad

appropriate to the small angle counters. These results are given in Table 5.

The equivalent photon cross sections are consistently about 30% larger than the exact cross sections. This is consistent with accuracies reported by other authors,[33,34,35] as the equivalent photon approximation, applied twice in this case, is expected to break

down when the electrons scatter to angles large compared to $\sqrt{m/E}$. The 30% agreement, however, increases our confidence in the accuracy of the exact calculation.

C. The C = - Process

Once we had available the expression for the cross section for $e^+e^- \to e^+e^-e^+e^-$ (C = +), it was a simple matter to convert this for C = - process. The method is shown by Fig. 37 : a) is the diagram for the C = + process with the produced particles detected and one scattered particle tagged. For the C = - process, the phase space is the same but the matrix element must be changed by exchanging certain variables.

If the produced particles are to be detected and one scattered particle undetected, the matrix element is shown in b). It is the same matrix element as for a) if the following substitution is made:

$$(E_2,\vec{p}_2) \leftrightarrow (-W_1,-\vec{q}_1)$$
$$(E_2',\vec{p}_2') \leftrightarrow (W_2,\vec{q}_2)$$
$$(w_2,\vec{K}_2) \to (-W_1-W_2,-\vec{q}_1-\vec{q}_2).$$

Alternatively for the C = - process one can detect only one produced particle and one scattered particle letting the other produced particle go undetected. Actually the detected state is no longer C = -. This is shown in c) and requires the substitution:

$$(E_2,\vec{p}_2) \leftrightarrow (-W_1,-\vec{q}_1)$$
$$(w_2,\vec{K}_2) \to (-W_1-E_2',-\vec{q}_1-\vec{p}_2').$$

This method is valid only for a final state of all electrons and

CHANGING THE C=+ DIAGRAM TO C=-

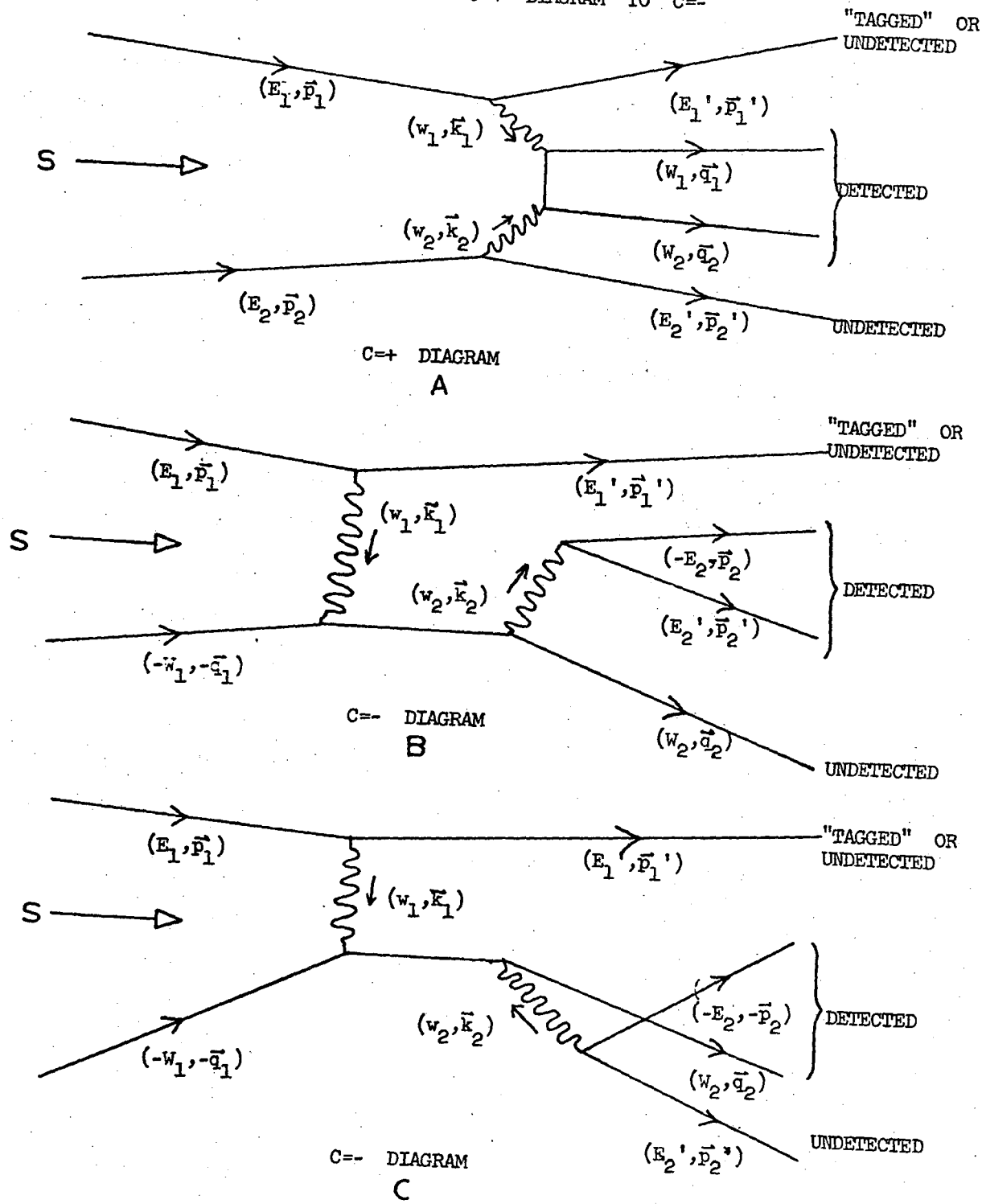

XBL 756-1728

Figure 37

positrons. Fig. 38 shows a comparison of $d\sigma/d\psi$ for $e^+e^- \to e^+e^-e^+e^-$ at 2.4 GeV for the three processes of Fig. 37 on a log scale. Notice the peak from diagram b) at coplanarity 180° characteristic of two particles produced by a photon. These calculations are also shown in Tables 5 and 6 where the C = -cross sections are doubled because both incident particles can pair produce. As can be seen, these cross sections should be negligible compared to the C = + cross sections.

D. Two-Prong Data

1. Nature of the Data

Two-photon events* are of interest as a source of background to the one-photon events in this experiment. It is very useful to the understanding of the calculated two-photon background to understand also the most prominent features of the two-photon events themselves. The most striking feature, as we have seen, is the sharp coplanarity peak of the two prongs ($\gamma\gamma \to A^+A^-$). Fortunately these events are not buried in Bhabhas or mu pairs for two reasons: they generally have momenta much less than the beam momenta and, although they tend to be coplanar, they do not tend to be colinear as do the Bhabhas and mu pairs.

The radiative Bhabhas:

$$e^+e^- \to e^+e^-\gamma$$

do overlap with the two-photon events somewhat since the electron and positron can lose a considerable fraction of their momentum.

*From here on, by "two-photon events" we mean the C = + process of Fig.30a

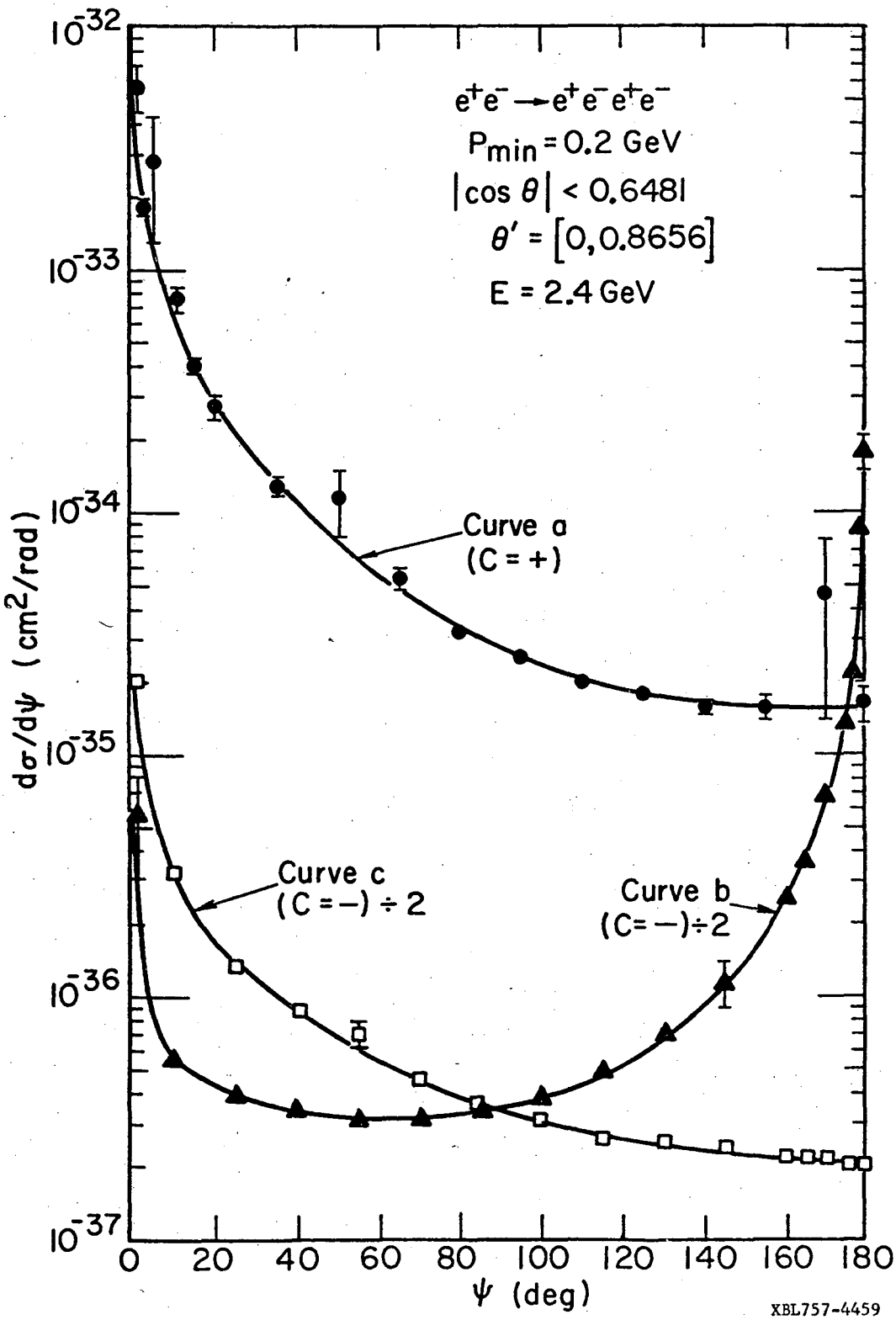
$e^+e^- \rightarrow e^+e^-e^+e^-$
$P_{min} = 0.2$ GeV
$|\cos\theta| < 0.6481$
$\theta' = [0, 0.8656]$
E = 2.4 GeV
Curve a
(C = +)
Curve c
(C = −) ÷ 2
Curve b
(C = −) ÷ 2
$d\sigma/d\psi$ (cm^2/rad)
ψ (deg)
10^{-32}
10^{-33}
10^{-34}
10^{-35}
10^{-36}
10^{-37}
0
20
40
60
80
100
120
140
160
180
XBL757-4459

Figure 38

The radiative Bhabhas are eliminated on the basis of their large pulse heights and the fact that one track must be $>2/3\ E_{beam}$.

The one-photon events also provide a background to the two prongs, specifically where the one photon produces many low-momentum tracks, only two of which are detected. Such one-photon events have a coplanarity distribution which is only slightly peaked at zero coplanarity. This distribution is found either from extrapolation of data from where the two-photon process is small (at resonant energies), or from simulated one-photon cross sections as will be discussed later. The one-photon events can be neatly subtracted to give a two-photon event distribution that agrees well with the calculation.

2. Event Classification

In order to compare the two-photon calculations with the experimental data, we look at the class of events which have two tracks found in the detector and separate out those events which do not come from the two-photon process. There are basically three types of background to the two-photon process:

1) Non-beam derived backgrounds:

   cosmic rays

   gas scatters (collision of an electron in one beam with a proton in the residual gas)

   pipe events (collision of photon produced by one beam with with the beam pipe)

2) Lower order quantum electrodynamic processes:

Bhabhas ($e^+e^- \rightarrow e^+e^-$)

mu pairs ($e^+e^- \rightarrow \mu^+\mu^-$)

radiative Bhabhas ($e^+e^- \rightarrow e^+e^-\gamma$)

3) One-photon hadronic events, specifically where many particles are produced, but only two tracks are detected.

Each of these types of background is separated by the event classification scheme which is shown in a simplified form in Table 7.

Cosmic rays can trigger the detector by passing close enough to the beam interaction region to trigger the pipe counter and leave a single track which looks like two back-to-back tracks coming from the beam position. These events are easy to separate from real events by their measured flight times. As the track passes through a trigger counter, the time is measured relative to the time the beams cross. For beam-originated two-prong events, the times in the two counters will both be the same, about 4 or 5 ns. For cosmic rays these two times will differ by the time it takes the cosmic ray to pass from one trigger counter to the other, about 8 to 9 ns. Since these times are measured with accuracy of 0.5 ns, the cosmics are easily identified and eliminated.

The next step for events with good flight times is to fit the tracks to a common vertex. A general fitting program, CIRCE,[13] is used which varies momenta and the vertex point to find the best fit to the spark chamber space points. Only events for which a convergent fit is found are kept. These events are represented by the top box in Table

Table 7

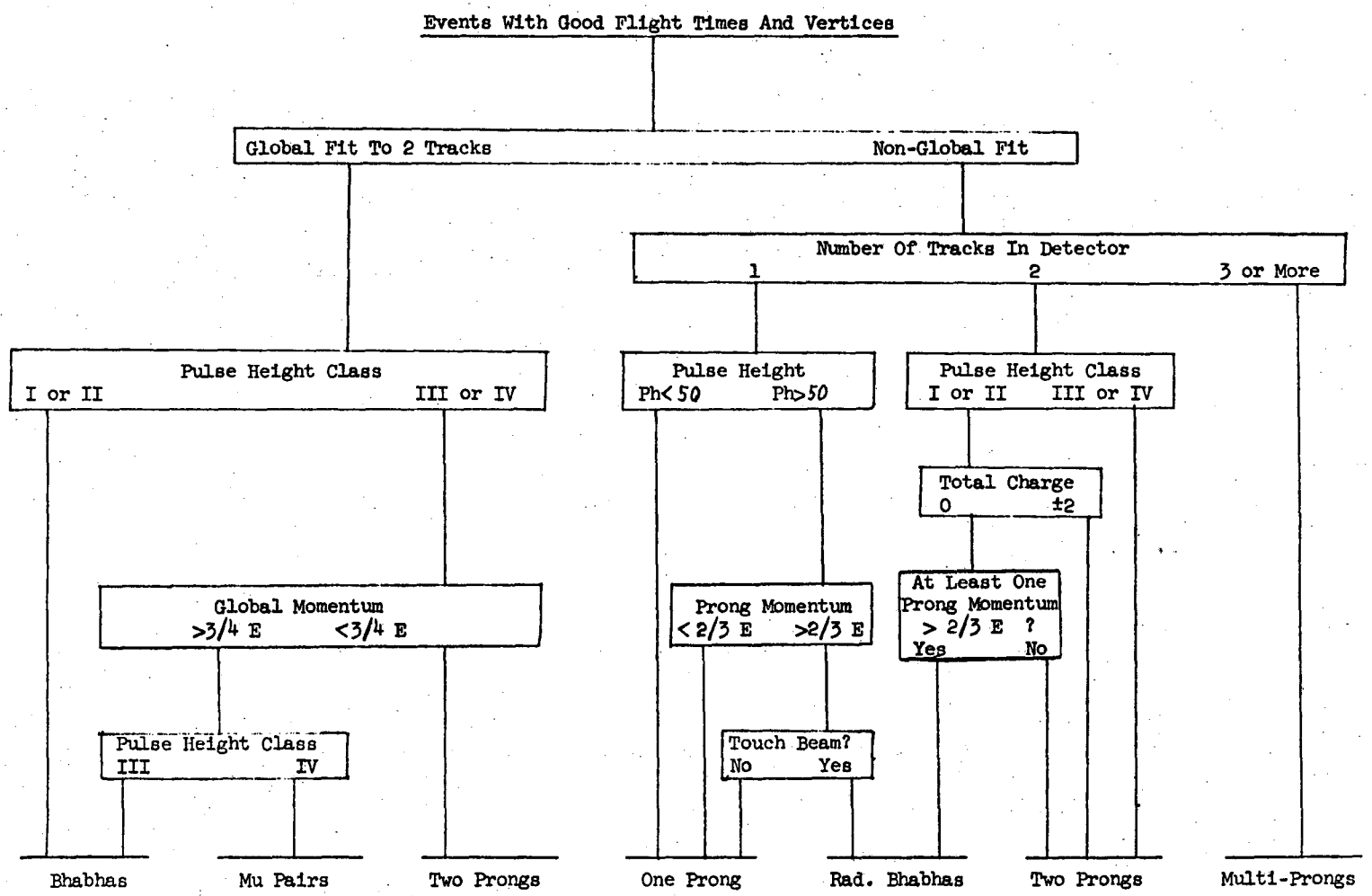

Pulse Height Classes:	I: Ph1>50 and Ph2>50	II: Ph1>100 or Ph2>100
	III: Ph1>50 or Ph2>50 but not I or II	IV: Ph1<50 and Ph2<50

XBL 757-1775

If an event produces only two charged tracks, their momenta must be equal and opposite and their charges opposite. The two tracks for such an event will look like one continuous curved track and can be fit to a single global momentum. This is the method used to identify Bhabhas and mu pairs. Only global tracks are considered candidates for Bhabhas and mu pairs and those must have momentum greater than 1/2 of the beam momentum, allowing for a reasonable momentum error at p = 2.4 GeV/c. The shower counters provide the discrimination between electrons and muons at these high momenta. Electrons will radiate in the shower counters giving up all of their energy and hence a large pulse height. The heavier muons are affected less by the lead and travel on through with only ionization energy loss. Pulse height classes for two-track events are shown in Table 7 with 50 being the minimum electron pulse height. The Bhabha and mu pair separation scheme is diagrammed.

The Bhabhas and mu pairs present the further problem that they can radiate significantly and be non-colinear enough to escape the global classification. Such events have tracks with a momentum distribution which falls rapidly with decreasing momentum from a peak at the beam momentum. The two-prong events, on the other hand, peak at low momentum as shown in Table

The remaining events are now called two prongs, but still need to have background and multihadron events subtracted to give the two-photon sample.

3. Background Separation

Next we consider the more difficult problem of separating out the background events. By background events, here, we mean non-colliding-beam-derived events other than cosmic rays, specifically gas scatters and pipe events.

These events have been studied carefully by running SPEAR in a mode where the beams pass each other but do not collide. In this mode, only background events will trigger. It is difficult to obtain absolute rates in this way, since there are no Bhabhas to normalize on, but valuable information can be found about the vertex distribution of these events.

The pipe events have a vertex distribution which peaks at $(x_v^2 + y_v^2)^{1/2} = 7\ 3/4$ cm rather than 0 cm in xy space and are rather uniform in z space between $z = \pm 45$ cm. The gas scatters vertex distribution is also uniform in z. To eliminate these events, a vertex cut is made at $(x_v^2 + y_v^2)^{1/2} < 3$ cm and $|z_v| < 30$ cm. This cut eliminates most of the background while having a negligible effect on the beam-beam derived events.

The remaining background events are also dealt with. After the $(x_v^2 + y_v^2)^{1/2} < 3$ cm cut is made on the data, the remaining background is still uniform in z_v. The $|z_v| < 30$ cm cut only removes a part of what remains. To estimate this remainder, the data satisfying $(x_v^2 + y_v^2)^{1/2} < 3$ cm and $30\text{ cm} < |z_v| < 45$ cm is sampled, and twice this amount is considered to be equal to the remaining background. The amount of this background is subtracted

from the amount of data satisfying $(x_v^2 + y_v^2)^{1/2} < 3$ cm, $|z_v| < 30$ cm to give the sample of beam-beam derived two prongs.

4. Multihadron Separation

The measured minus background two-prong distribution is shown in Fig. 39. This is certainly not all two-photon events for there are non-negligible contributions at large coplanarity. This contribution is due to one-photon multihadron events which send only two tracks into the detector and must be eliminated. This has been done in two independent ways.

The first method is to measure the two-prong distribution with sufficient cuts ($p > 300$ MeV/c, $\psi > 20°$) to eliminate two-photon events and combine this with all of the multiprong events to extrapolate the full distribution. This is, of course, just what is done when the total hadronic cross section is inferred from the detected hadronic cross section as discussed in part III. Here models must be supplied for the total number of charged and neutral tracks produced in an event and the angular distributions of these tracks. Then, using Monte Carlo computer simulations, the distribution and number of charged tracks reaching the detector is calculated and fit to the data by varying the parameters of the model. This model will then give the distribution of two-prong events in any region desired.

The second method is more direct and uses data from the $\psi(3095)$ resonance. The resonant data shows an enhancement of the hadronic

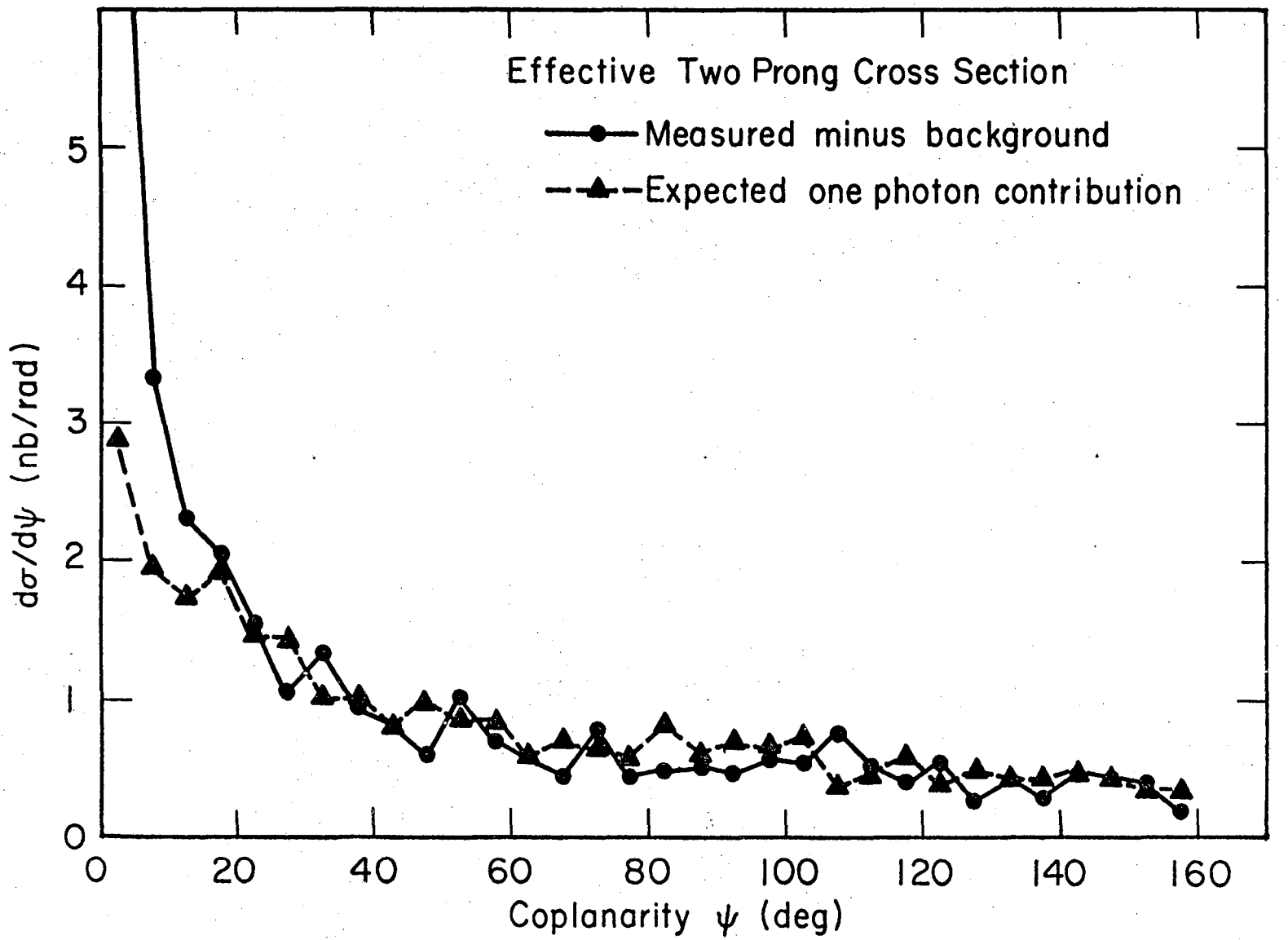

XBL757-4460

Figure 39

cross section by a factor of 200[2]. However, since this resonance is in the one-photon channel, it should not enhance the two-photon cross sections at all. For the resonant data, the two-photon cross section is a negligible fraction of the two prongs, which then reflect just the one-photon distribution of two prongs. This method, of course, assumes that the angle and number distributions of $\psi(3095)$-produced hadrons is the same as for photon-produced hadrons. This is not necessarily true, since the $\psi(3095)$ has been shown not to decay primarily by turning into a photon.[6] This method, however, shows excellent agreement with the first method. Fig. 39 shows the one-photon contribution as estimated by the second method. The data are consistent with most of the non-coplanar two prongs coming from one-photon processes.

5. Comparison with Calculation

Once the one-photon contribution has been estimated, it is subtracted from the two-prong class with non-beam events removed. A final cut is made on that data requiring $p_1 < 2/3\ E_{beam}$ and $p_2 < 2/3\ E_{beam}$ to eliminate radiative $e^+e^- \rightarrow \mu^+\mu^-$ events and any residual radiative $e^+e^- \rightarrow e^+e^-$ and non-beam events. The remaining events in the region $0° < \psi < 20°$ are shown in Fig. 40 with statistical errors. These are the two-photon events. The scale is absolute, the data being normalized to Bhabha events. Also shown with calculational errors is the calculated two-photon cross section for e's, μ's and pointlike π's. The agreement is excellent for

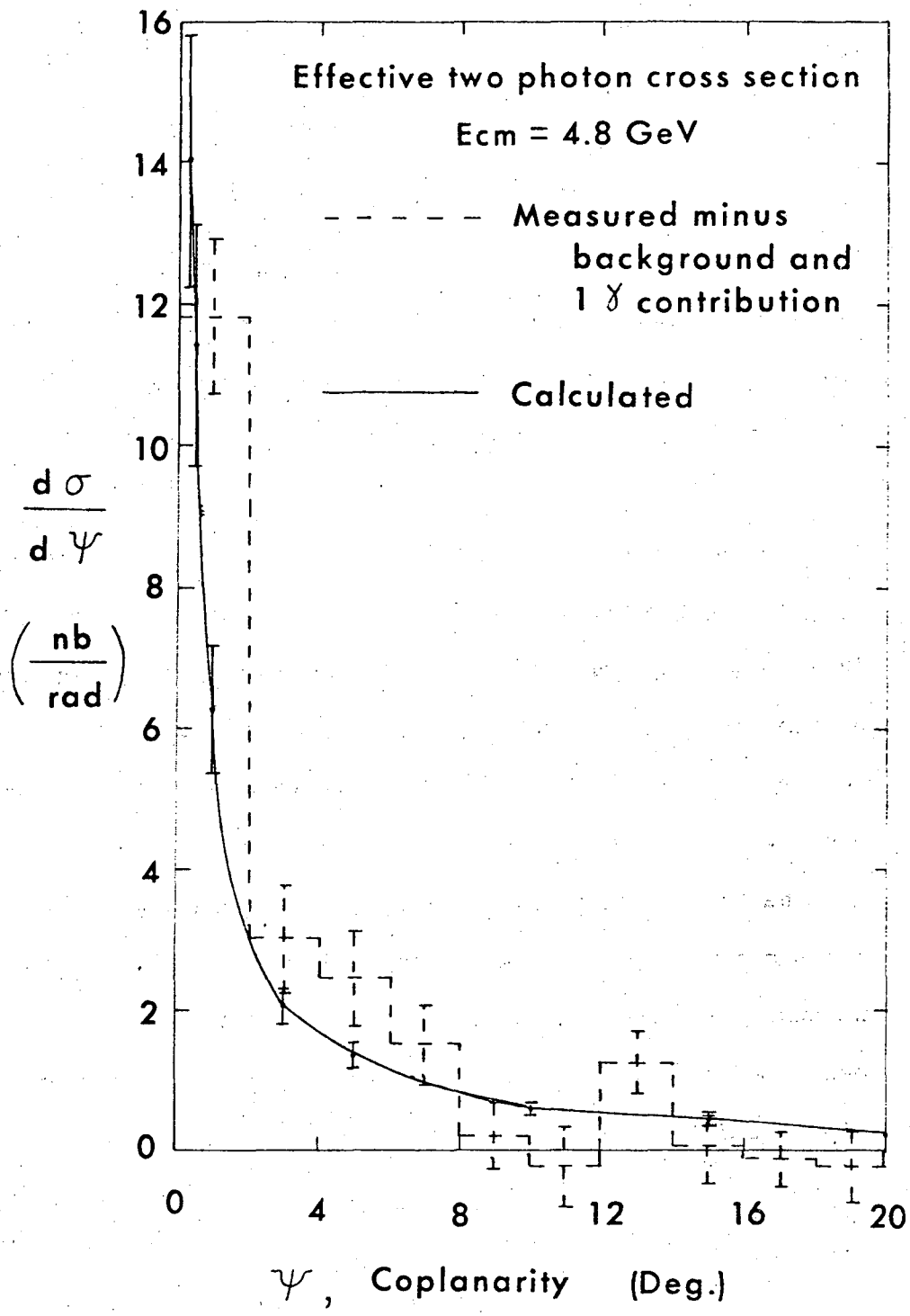

XBL759-4108

Figure 40

$\psi > 2°$. This is probably due to errors in calculating $d\sigma/d\psi$ in this region as discussed in section V-B3.

Numerical results are given in Table 8 for cross sections with two tracks in the detector and $p > 225$ MeV/c, $\psi < 20°$ at 2.4 GeV. The calculated cross section is shown to be 0.608 ± 0.075 nb and the measured cross section with backgrounds subtracted is 0.685 ± 0.069 nb. The overall agreement is quite good.

6. Other Features of the Data

To further compare the data with calculation we can plot event distributions versus other variables and observe further characteristics of the distinctive two-photon events. As with $d\sigma/d\psi$, the data will be cut such that $0° < \psi < 20°$ and one-photon and background events will be subtracted.

The most significant characteristic of the events is their peaking at low momentum due to the infrared divergence of the bremsstrahlung photons. Fig. 41 shows the distribution of the data with the momenta cut off at $p = 0.225$ GeV/c. Also shown for comparison is a calculation of $d\sigma/dp$. The calculation is done at $\psi = 1°$ where most of the data resides rather than for $0° < \psi < 20°$ to reduce the calculational errors. Fig. 42 shows the distribution of data with $|\cos\theta|$. Again the calculation is done at $\psi = 1°$. The data shows a slight peak as $|\cos\theta| \to 1$ unlike the hadronic one-photon data. Both calculations are normalized to the data. Errors are large on both data and calculation, but the agreement appears to be good.

Calculated and Measured σ_{EFF} for $e^+e^- \to e^+e^-A^+A^-$

At E=2.4 GeV/Beam with $|\cos\theta_i| < 0.6$, $p_i > .225$ GeV/c

$0° < \Psi < 20°$ and .76±.08 Detection Efficiency

Cross Sections in Nanobarns	No "Tagged" Electron	One "Tagged" Electron
Calculated Cross Sections:		
$e^+e^- \to e^+e^-e^+e^-$ (C=+):	.314±.047	.0145±.0022
$e^+e^- \to e^+e^-u^+u^-$ (C=+):	.245±.036	.0132±.0020
$e^+e^- \to e^+e^-\pi^+\pi^-$ (C=+,point):	.049±.007	.0031±.0005
Sum of Calculated Cross Sections:	.608±.075	.0308±.0038
Measured Cross Sections:		
Measured Two Prongs With Background Subtracted:	1.120±.066	.0310±.0090
Minus Hadronic Cross Section:	-.435±.021	-
Minus Accidental "Tags":	-	-.0009±.0003
Measured Two Photon Cross Section:	.685±.069	.0301±.0090

Table 8

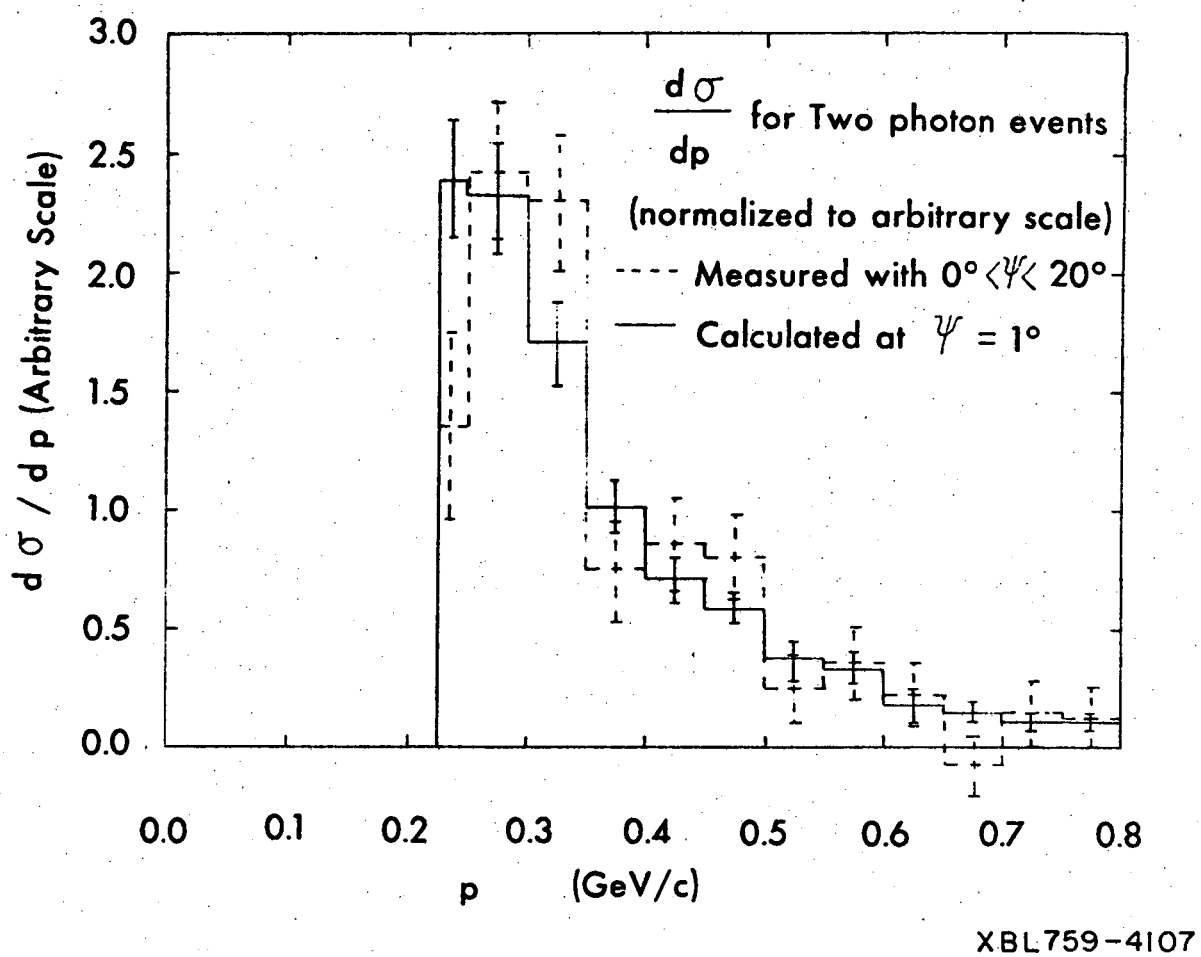
3.0
2.5
2.0
1.5
1.0
0.5
0.0
d σ / d p (Arbitrary Scale)
dσ/dp for Two photon events
(normalized to arbitrary scale)
Measured with 0° < Ψ < 20°
Calculated at Ψ = 1°
0.0
0.1
0.2
0.3
0.4
0.5
0.6
0.7
0.8
p (GeV/c)
XBL759-4107

Figure 41

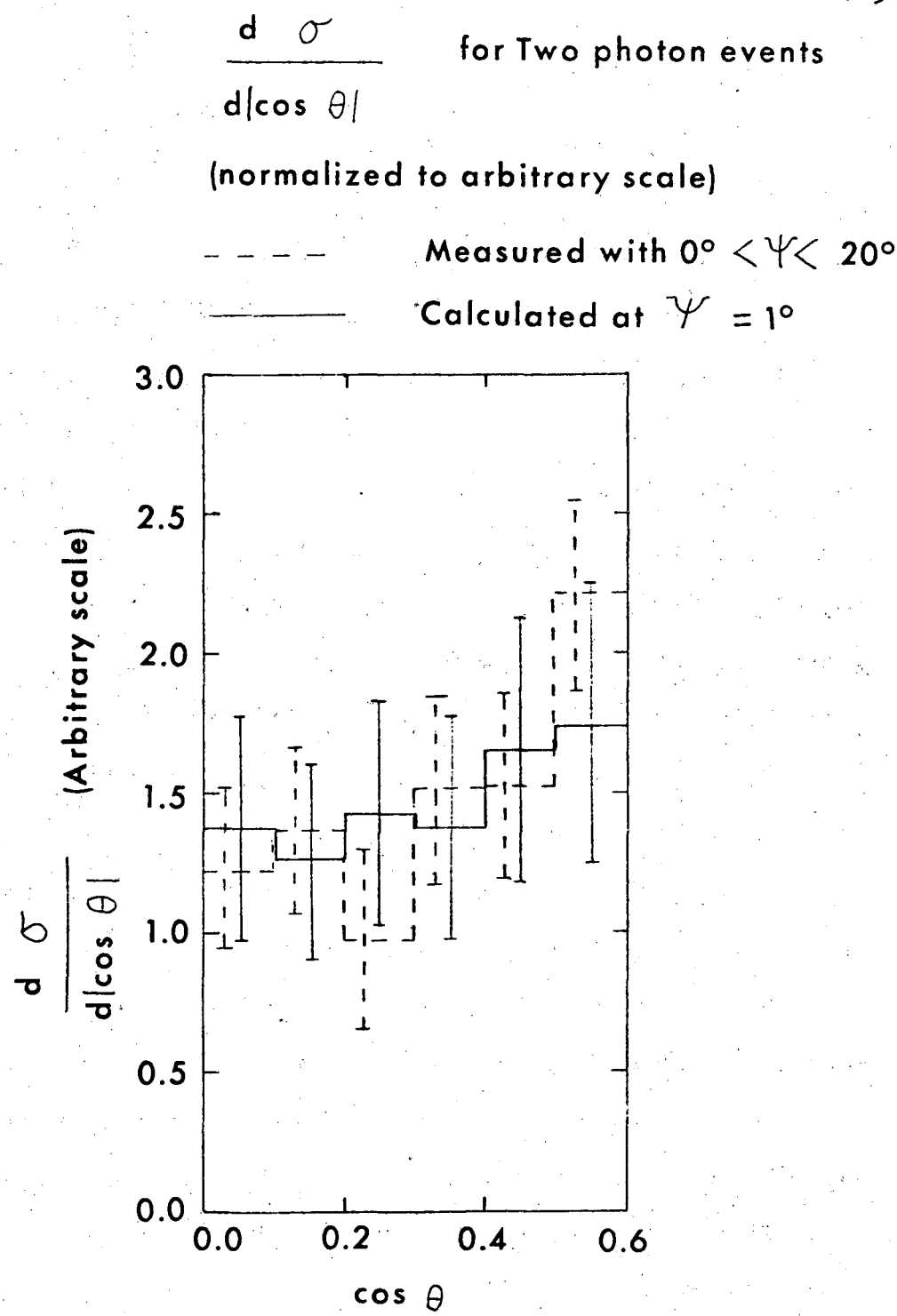

XBL759-4106

Figure 42

7. Particle Identification

In this experiment, we were unable to distinguish electrons from muons in the momentum range 200-500 MeV/c. Unfortunately, this is precisely where the two-photon events were produced, so we were unable to separate the events $e^+e^- \rightarrow e^+e^-e^+e^-$ from $e^+e^- \rightarrow e^+e^-\mu^+\mu^-$.

There were three separate means for electron muon discrimination. The most important was the shower counter system. High energy electrons (1 GeV) radiate all of their energy in the shower counters giving large pulse heights while high energy muons deposit only a fraction of their energies. At lower energies, the muons give off much more of their energy while the electrons have less energy to give. By 500 MeV/c the two pulse height distributions have merged.

The second means was the time-of-flight information from the trigger counters. From the flight time, one calculates velocity and, using the momentum, the rest mass. This works best at low momenta (100 MeV). At 200 MeV/c, β for an electron is $1\text{-}3\times10^{-6}$ and for a muon is .89; flight time is 4.9 ns for an electron and 4.4 ns for a muon. The .5 ns resolution of the flight times did not allow separation of electrons and muons, but the flight times were consistent with the two-photon events being about half of each.

Finally the muon spark chambers could only identify muons which passed through the iron flux return. This required at least 600 MeV/c.

E. "Tagged" Two-Prong Data

1. Tagging the Two Prongs

The two-prong data showed an excellent fit to the calculated two-photon cross section, but only after the estimated one-photon contribution was subtracted. The subtraction accounted for about 50% of the data and hence statistical errors were not small. It is desirable to find a means to separate the two-photon events from the one-photon events without resorting to a subtraction.

The simplest method is to detect one of the scattered electrons along with the particles found by the main detector. This method has the advantage that the one-photon events are eliminated but the disadvantage that, with our apparatus, only about 4.8 % of the two-photon events are detected. As far as statistics are concerned, these features approximately balance each other. The "tagged" events have one further advantage which is that, while most of the cross section is still within $\psi < 20°$, there is not as sharp a peak at $\psi = 0°$ as there was for the "untagged" events. This occurs because the tagged electrons must be collected at a relatively large angle and hence the produced state will have significant total transverse momentum.

Fig. 43b shows the tagging apparatus used to select two-photon events. The detector is schematically drawn as a barrel with particles which pass through its side. The four tagging counters consist of defining counters followed by shower counters. They are situated at 25 mr to the beam axis above and below the beam on each side. Each has an effective area of 3 square inches and the four subtend a total

TAGGING APPARATUS

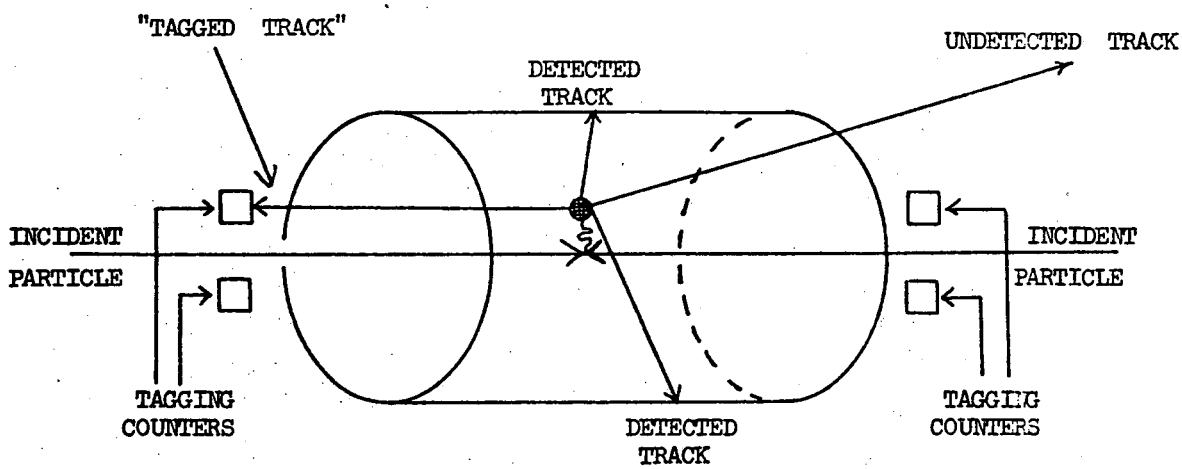

ONE PHOTON EVENT
A

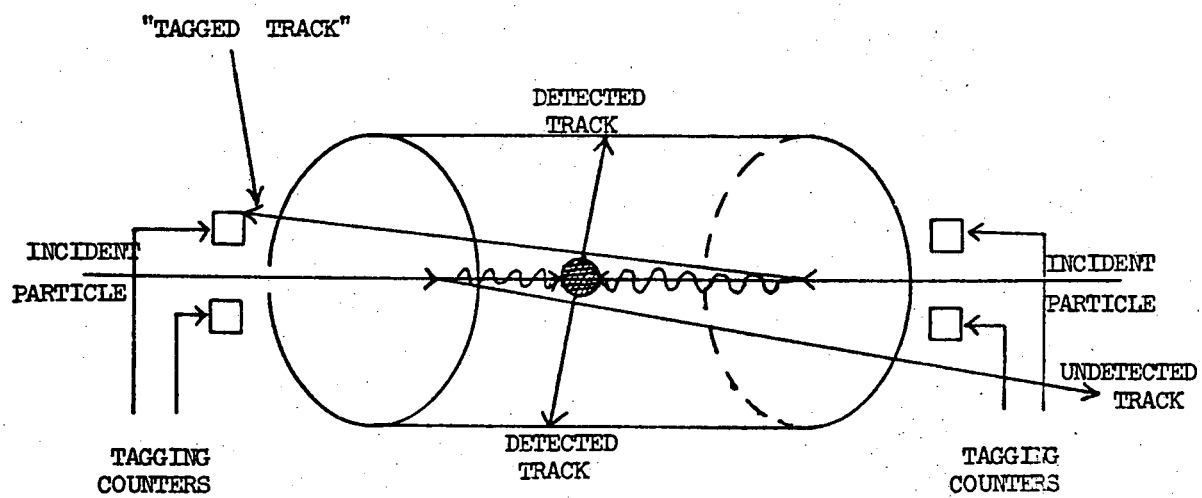

TWO PHOTON EVENT
B

XBL 756-1729

Figure 43

of 1.3×10^{-4} of 4π steradians. When an event has a signal present in any one of the four counters, it is considered a "tagged" two-prong. The bremsstrahlung electrons of the two-photon events are strongly peaked forward and the chance of such an event's being "tagged" in one of the four counters is greatly enhanced to about 4%. The chance for a one-photon two-prong event to be tagged as in Fig. 43a can be roughly estimated by phase space to be 3×10^{-4}. Such events are further discriminated against by requiring the pulse in the tagged shower counter to be large, characteristic of an electron, virtually eliminating the small pulses of pions from one-photon events. The actual pulse height cut was made at >50% of the pulse height from an electron with beam energy. Hence electrons with energy roughly 50% of the beam energy will be counted by the shower counter. This is the case for virtually all two-photon scattered electrons.

2. Accidental Rate

We obtained a good empirical estimation of the accidental rate in the tagging counters. Accidental tags can come from an accidental count in the defining counter and a gas-scattered electron in the shower counter for example. The number of "tagged" Bhabhas compared to the total number of Bhabhas is $8.1 \pm 2.4 \times 10^{-4}$. Since Bhabhas produce no other particles to be tagged, this must be just the accidental tagging rate.

To calculate the accidental two-prong cross section we merely multiply the accidental rate by the two-prong cross section with the background subtracted. This gives:

$$\text{Acc. Rate} = (8.1 \pm 2.4) \times 10^{-4} \times (1.12 \pm .03 \text{ nb})$$
$$= .0009 \pm .0003 \text{ nb}$$

(see Table 8).

3. Comparison with Calculation

Fig. 44 and Table 8 show the comparison between the data and the calculated tagged cross section. As can be seen, the agreement is again excellent, but statistics, based on 12 events, are not much better than for the untagged case. Notice the much flatter coplanarity distribution. From Table 8 we find the calculated cross section to be 0.0308 ± 0.0038 nb and the measured cross section 0.0301 ± 0.0090 assuming pointlike pions.

4. Angular Distribution

There is one further method to assure ourselves that the events we are observing are two-photon events. This is to observe the effect of the bias on the data caused by tagging the events. If the taggings were all accidental, there would be no bias, while, if we are indeed tagging two-photon events, the results are quite predictable.

We have already seen one effect of the tagging in the flatter coplanarity distribution of events. The untagged events have a strong coplanarity peak because the bremsstrahlung electrons are emitted very close to the forward direction and there is little transverse momentum available for the produced state. Hence the two produced particles are back-to-back in x-y projection.

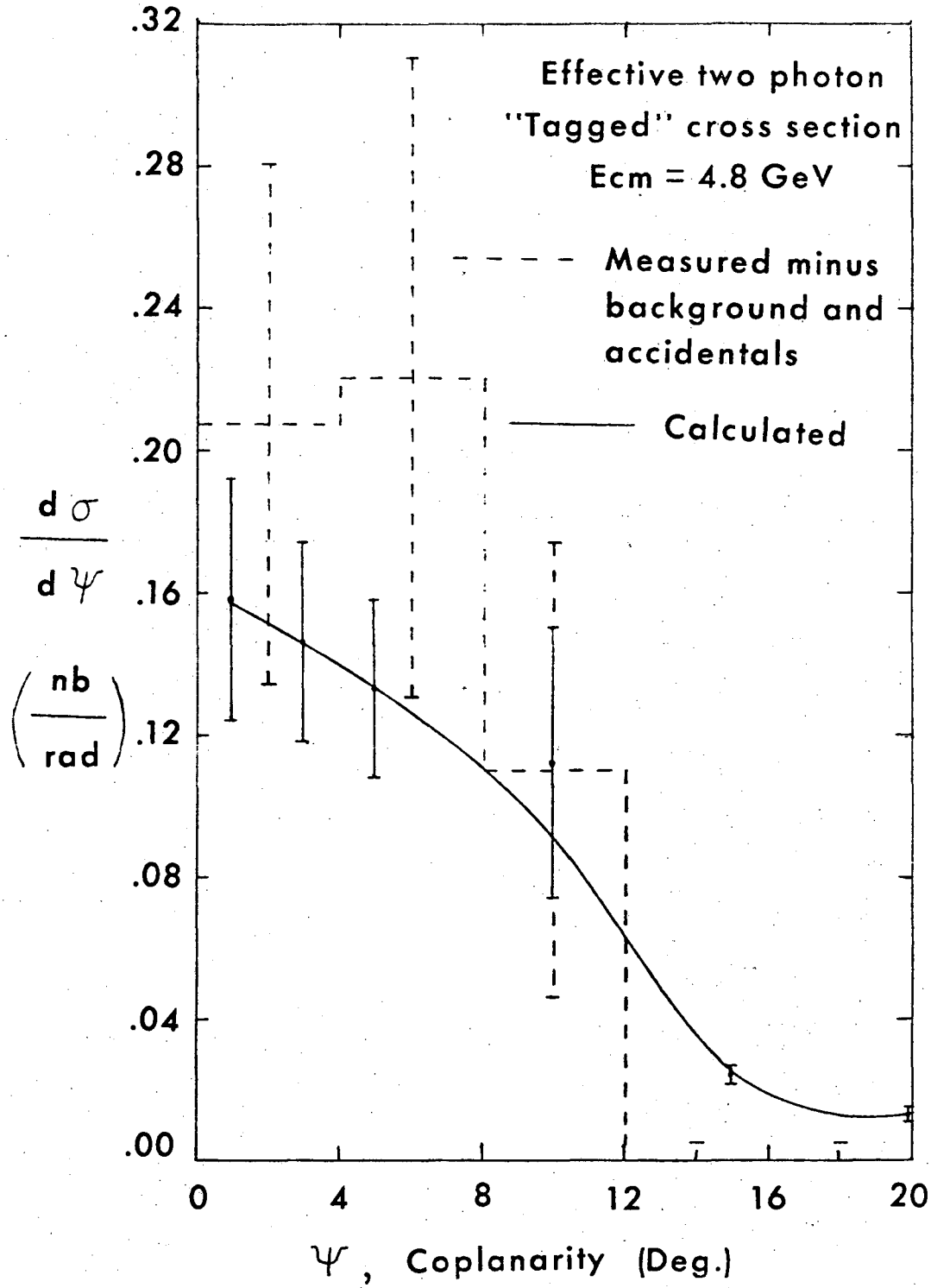

XBL759-4109

Figure 44

When we require one scattered electron to be tagged, the sample becomes biased. Most of the untagged scattered electrons are emitted at less than the 25 mr polar angle of the tagging counters. Thus the tagged electrons have roughly 40 MeV more transverse momentum than the average untagged electron. This transverse momentum is balanced by an equal (and opposite) total transverse momentum in the produced state. If the produced particles are emitted perpendicularly to this transverse momentum, the additional transverse momentum will have the effect of spreading out the coplanarity peak through about 15°. This is precisely what we see in Fig. 44.

We can further test this hypothesis. The additional transverse momentum is always in the vertical direction since the tagging counters are above and below the beam pipe. Thus produced particles emitted horizontally will feel the maximum effect of this transverse momentum, while those emitted vertically should show the same coplanarity peak as the untagged sample.

To attempt to observe this effect, we loosened the cuts on the tagged sample to provide more events and improve statistics. The looser cuts were $p_i > 200$ MeV/c and $|\cos\theta_i| < 0.6481$. Although the detector is somewhat inefficient in the added region the additional error due to this inefficiency should be less than 10%. The larger sample contained 22 events.

We divided the 22 tagged two-photon events with $\psi < 20°$ into two groups: the horizontals, where the tracks had $\cos^2\phi > 1/2$ and the verticals, which had $\cos^2\phi < 1/2$. We expect the verticals to

show a sharper coplanarity peak than the horizontals. Fig. 45 shows the coplanarity distribution of the two samples as well as calculations of the expected distributions.

A difference between the two distributions is apparent. Compared to the full sample of Fig. 44 we see the coplanarity peak is sharper for the verticals and almost flat for the horizontals out to $\psi = 15°$. Also, the agreement with calculation is excellent, making it even more plausible that these are two-photon events.

5. Doubly Tagged Event

We found one "exclusive" event where all four final particles were detected or tagged. It is shown in three projections in Fig. 46. Final state momenta in MeV/c are, using the notation of Fig. 31.

$p_{1x} = 179$	$p_{1y} = -155$	$p_{1z} = -25$
$p_{2x} = -192$	$p_{2y} = 55$	$p_{2z} = -125$
$p'_{1x} \simeq 0$	$p'_{1y} \simeq 56$	$p'_{1z} \simeq 2237$
$p'_{2x} \simeq 0$	$p'_{2y} \simeq 52$	$p'_{2z} \simeq -2088.$

This accounts for a measured cross section of .0026 ± .0026 nb for the exclusive channel, compared to the .0015 ± .0004 nb calculated cross section.

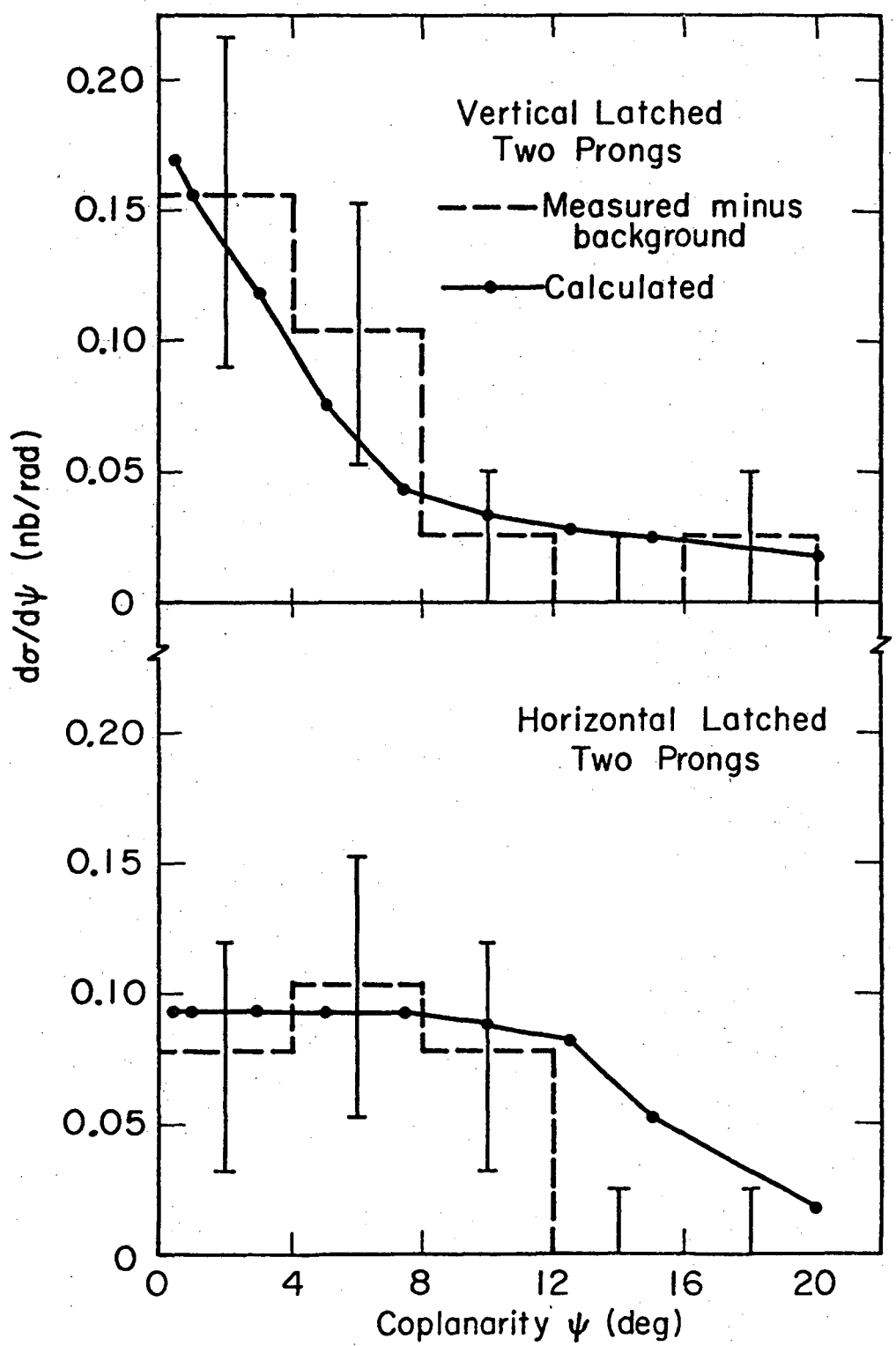

XBL757-4463

Figure 45

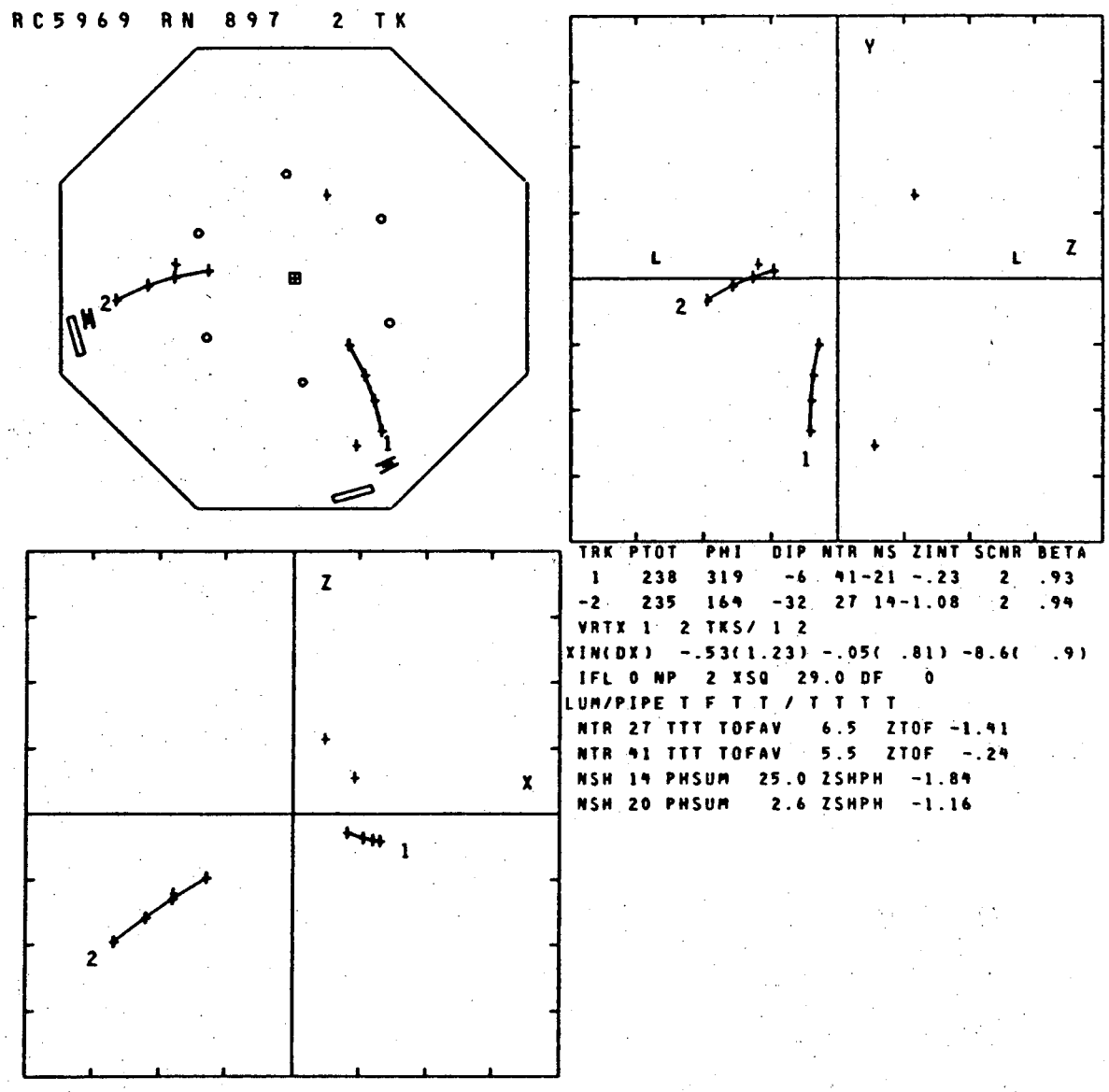

XBL 757-1773

Figure 46

F. Subtraction of Fourth Order Contamination

1. Method of Elimination

Now that we have a good understanding of the two-photon events, we return to the problem of eliminating them from the one-photon data. As we have seen the coplanarity peak is very sharp for two-photon events and also the momenta tend to be small. We can eliminate 2/3 of the two-prong two-photon events by requiring the coplanarity to be greater than 20°. About half of the remaining events can be eliminated by requiring the momentum to be greater than 300 MeV/c.

These two cuts on the two-prong events, while not drastic for the one-photon events, make the two-photon contribution negligible. The cut in $\cos\theta_i$ is loosened to $|\cos\theta_i| < 0.6481$ to include the maximum possible sample of events.

2. Calculated Contamination

The remaining two-photon contribution can be calculated from the exact formulas and is shown in Fig. 47 for beam energies from 1.2 to 4.0 GeV. This is the method used to calculate the two-photon contamination to the hadronic data. At 2.4 GeV, it accounts for 1.5 ± .2% of the two-prong data and is subtracted for calculation of the total hadronic cross section.

As a check on the calculation of two-photon cross sections in the acoplanar region we can compare the calculated acoplanar "tagged" cross section, .0124 ± .0010 nb for $|\cos\theta_i| < 0.6481$ and $p_i > 200$ MeV/c, with the equivalent measured quantity 0.149 ± .0066 nb. The agreement is excellent within the statistics.

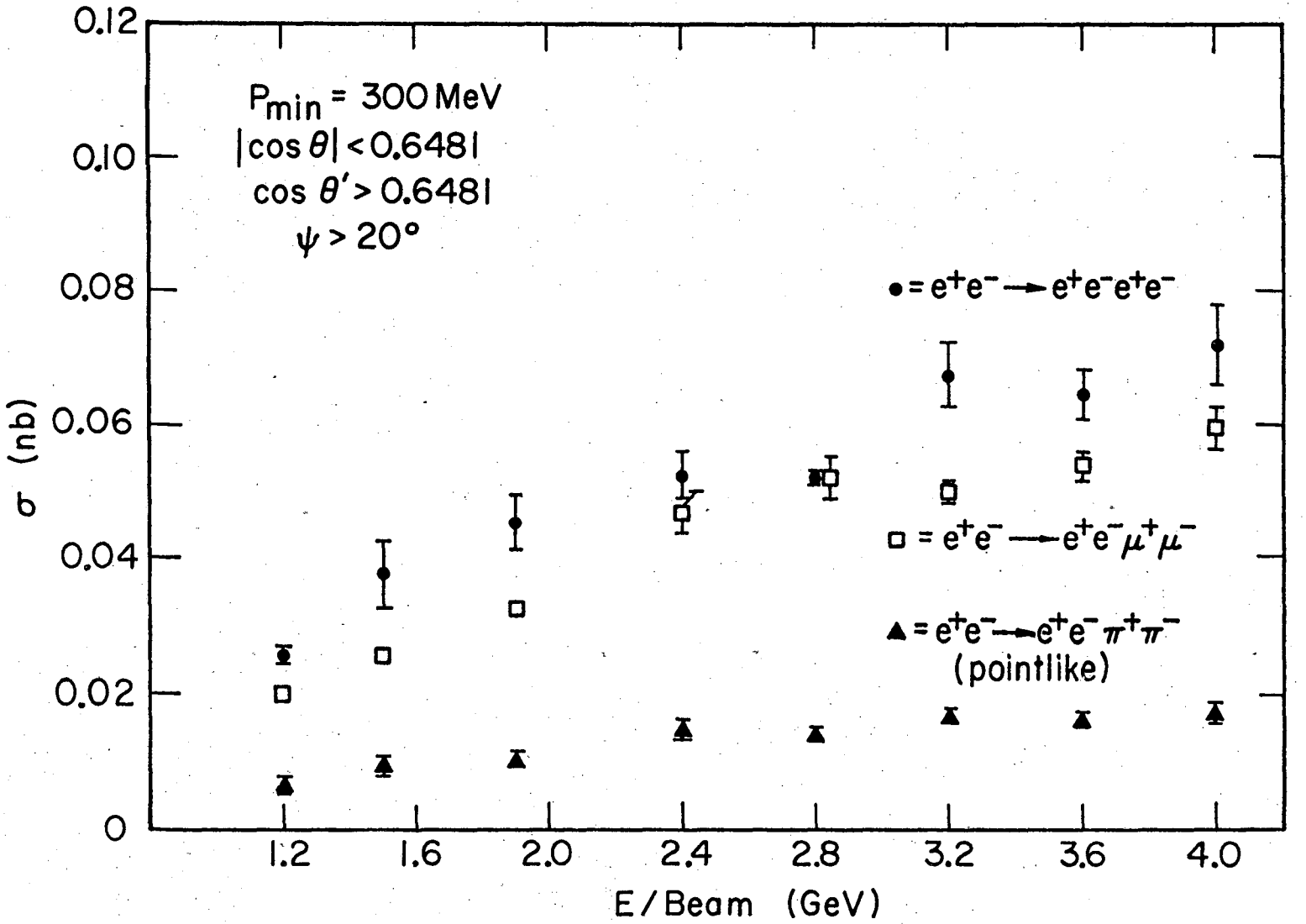

XBL757-4464

Figure 47

Finally the contamination rate for the multiprong events (3 or more) is estimated by measuring the cross section for "tagged" multiprongs minus accidental and dividing this by a general tagging efficiency of 4.8% ± 1.0 derived from the equivalent photon approximation. This upper limit for multiprong contamination is 2.0 ± 1.3%. The net effect of the two-photon events in the two prongs and multiprongs is to cause a 6% error in the measurement of the total detected hadronic cross section.

G. Hadron Physics with the Two-Photon Process

1. Two-Pion Results

There are several experimental results from two-photon processes that are useful to hadron physics, and these have been discussed by several authors.[26,27] Unfortunately this experiment cannot contribute extensively to this area of physics for two reasons; the hadronic two-photon sample is small, about 19 "untagged" events and 1 "tagged," as we were unable to separate the pions from muons and electrons in the relevant momentum range. For several quantities, however, we can make a first experimental estimate. In this section, we will discuss only those areas of two-photon hadron physics for which we made measurements or for which we felt we were close to making measurements.

The most fundamental quantity to measure is the cross section σ_π, for producing two charged pions by the process

$$e^+e^- \rightarrow e^+e^-\pi^+\pi^- .$$

Previously we had assumed the Born approximation and calculated this cross section, σ_π (pointlike), in the detector to compare with the measured two-prongs. The good agreement between calculation and measurement indicates that σ_π is not far from σ_π (pointlike).

We can make this more quantitative by calculating the ratio of σ_π, measured, to σ_π (pointlike), calculated. This is done in Table 9 separately for "untagged" and "tagged" events. Statistical accuracies are similar for the two classes since one must have the one-photon events subtracted and the other has a very small event rate. The cross sections are computed for events sending two tracks into the detector, $|\cos\theta| < 0.6$ and $p > 225$ MeV/c, and with coplanarity less than 20°. Thus the measured to calculated ratio, σ_π/σ_π (pointlike) is for the effective region only.

The first line of Table 9 is the measured two-photon cross section with the one-photon part subtracted in the "untagged" sample. Next the calculated cross sections for $e^+e^- \to e^+e^-e^+e^-$ and $e^+e^- \to e^+e^-\mu^+\mu^-$ are subtracted. The remainder is assumed to be from $e^+e^- \to e^+e^-\pi^+\pi^-$ and the ratio of this remainder to the calculated quantity is given. Results are

$$\frac{\sigma_\pi}{\sigma_\pi \text{ (pointlike)}} = \begin{array}{ll} 2.6 \pm 1.9 & \text{untagged case} \\ 0.8 \pm 3.1 & \text{tagged case .} \end{array}$$

Combing these two results (assuming them uncorrelated) we find

$$\frac{\sigma_\pi}{\sigma_\pi \text{ (pointlike)}} = 2.1 \pm 1.6.$$

Here statistical errors are large, but the result that emerges is that the cross section for two charged pions is not far from the pointlike approximation.

σ^{π}_{EFF} for $e^+e^- \to e^+e^-\pi^+\pi^-$ (C=+) at E=2.4 GeV/Beam

With $|\cos\theta_i| < 0.6$, $p_i > .225$ GeV/c, $0° < \psi < 20°$

And .76±.08 Detection Efficiency

Cross Section in Nanobarns	No "Tagged" Electrons	One "Tagged" Electron
Measured Two Photon Cross Section:	.685±.069	.0301±.0090
Minus Calculated Cross Sections for $e^+e^- \to e^+e^-e^+e^-$ and $e^+e^- \to e^+e^-u^+u^-$:	.559±.059	.0277±.0030
Measured Cross Section, σ^{π}_{EFF}, for $e^+e^- \to e^+e^-\pi^+\pi^-$ (difference of above):	.126±.091	.0024±.0095
Calculated Pointlike Pion Cross Section, σ^{π}_{EFF}(pointlike):	.0494±.0074	.0031±.0005
$\sigma^{\pi}_{EFF}/\sigma^{\pi}_{EFF}$(pointlike):	2.55±1.88	0.77±3.05

Table 9

The next result concerned a search for resonances in the two-pion channel, particularly the σ meson at 750 MeV. Again we are hampered by a small number of events and the lack of separation of e's, μ's, and π's. Fig. 48 is a plot of the effective mass of two-prong events with coplanarity $\psi < 20°$. This sample is 11% non-collision events, 37% one-photon events, 25% two-photon $e^+e^- \to e^+e^-e^+e^-$ events, 23% $e^+e^- \to e^+e^-\mu^+\mu^-$ events, and only 4% $e^+e^- \to e^+e^-\pi^+\pi^-$ events, the channel where a resonance is expected. Only a very sharp and strong resonance will appear in this sample which is mostly background. We can, however, put an upper limit on

$$\int_0^{\sqrt{4E^2}} \sigma_R(\sqrt{s})\, d\sqrt{s}\, \frac{\Gamma_{Detected}}{\Gamma_{Total}}$$

for a hypothetical resonance, where $\sigma_R(\sqrt{s})$ is the cross section for $\gamma\gamma \to$ Resonance at photon-photon invariant mass squared s, and $\Gamma_{detected}/\Gamma_{total}$ is the branching ratio for the resonance to decay to two pions in the detector. From the effective mass plot we can infer

$$\sigma_{e^+e^- \to e^+e^-\text{Resonance}}\ (E = 2.4\ \text{GeV})\ \frac{\Gamma_{detected}}{\Gamma_{total}} \leq .08\ \text{nb}$$

for a narrow (.1 GeV) resonance around .75 GeV.

Using the equivalent approximation:

$$\sigma_{e^+e^- \to e^+e^-R}(E) \simeq 2\left(\frac{\alpha}{\pi}\right)^2 \left(\ln\frac{E}{m_e}\right)^2 \int_0^{2E} \frac{2d\sqrt{s}}{\sqrt{s}}\, f\left(\frac{\sqrt{s}}{2E}\right)\sigma_{\gamma\gamma\to R}(\sqrt{s})$$

$$\simeq 9.9 \times 10^{-3}(\text{GeV})^{-1} \int_0^{4E^2} \sigma_{\gamma\gamma\to R}(\sqrt{s})\, d\sqrt{s}$$

at $E = 2.4$ GeV, $s = (.75\ \text{GeV})^2$.

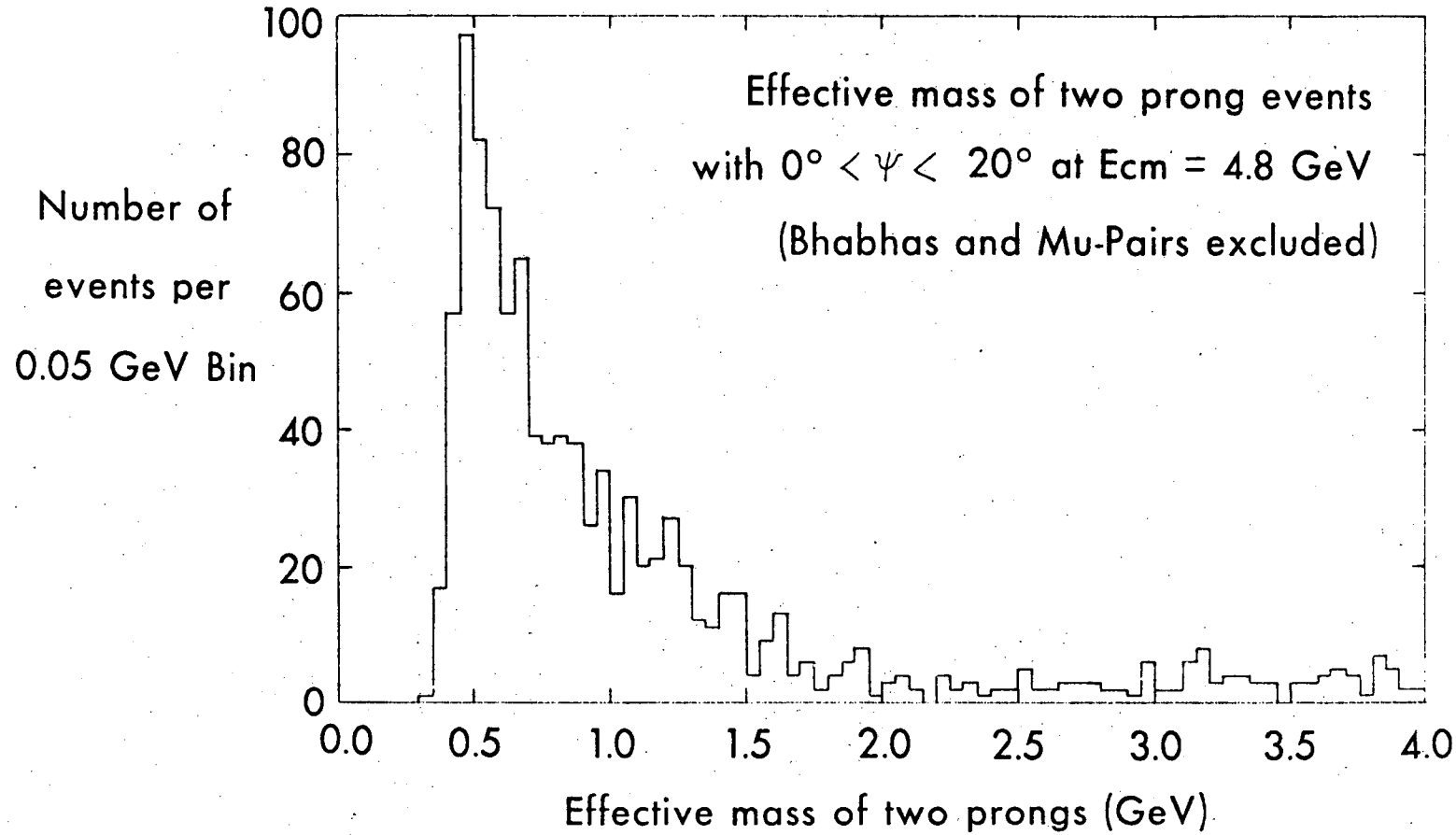

XBL759-4105

Figure 48

Therefore

$$\int \sigma_R(\sqrt{s})\, d\sqrt{s}\, \frac{\Gamma_{Detected}}{\Gamma_{Total}} < 8.1\ \mu b - MeV$$

near the predicted σ resonance.. These quantities are to be compared with the Born approximation calculations:

$$\sigma^{B}_{e^+e^- \to e^+e^-\pi^+\pi^-}(E = 2.4\ GeV) = 0.079\ nb$$

in the detector and

$$\sigma_{\gamma\gamma \to \pi^+\pi^-}\ (\sqrt{s} = .75\ GeV) = 0.2\ \mu b$$

total.

Finally the process $\gamma\gamma \to \pi^0$ is of interest as a direct measure of the π_0 lifetime. As first pointed out by Low[39] the π_0 lifetime T_{π_0} is related to the $\gamma\gamma \to \pi_0$ cross section by

$$\sigma_{\gamma\gamma \to \pi^0}(s) = \frac{8\pi^2\ \Gamma_{\pi^0 \to \gamma\gamma}}{m_\pi}\ \delta(m_\pi^{\ 2} - s)$$

where $\Gamma_{\pi^0 \to \gamma\gamma} = \frac{1}{T_{\pi_0}}$. Using the equivalent photon approximation

$$\sigma_{e^+e^- \to e^+e^-\pi^0}(E) \simeq \frac{16\alpha^2\ \Gamma_{\pi^0 \to \gamma\gamma}}{m_\pi^{\ 3}} \left(\ln\frac{E}{m_e} - \frac{1}{2}\right)^2 f\left(\frac{m_{\pi_0}}{2E}\right)$$

$$\simeq 1.0\ nb \text{ at } E = 2.4\ GeV$$

$$\text{with } \Gamma_{\pi_0 \to \gamma\gamma} = 8.6\ eV.$$

the best present value for the π_0 lifetime is $(.84 \pm .10) \times 10^{-16}$ sec. A good $\gamma\gamma$ detection system could hopefully provide a measurement to this accuracy.

In this experiment we were unable to make such a measurement. It would require detecting the two photons from $\pi^0 \to \gamma\gamma$ decay and

nothing else in the detector. This would best be done with a neutral trigger requiring one scattered electron to be tagged. The effective cross section for such a setup assuming perfect detection is about .03 nb. At SPEAR luminosity of 2×10^{30} $cm^{-2}sec^{-1}$we could collect at most 20 events in 100 hours of such special running and hope for an accuracy in the lifetime measurement of about 20-25%. Several backgrounds would have to be carefully considered. Still, this is a promising possibility for the future.

2. Multihadron Results

We can measure the cross section $\sigma_{e^+e^- \to e^+e^-x}$ for $e^+e^- \to e^+e^-\gamma\gamma \to e^+e^-$"Anything", where "Anything" assumes more than two charged hadrons detected. Since the untagged data contains primarily one-photon events, we must use the "tagged" three-or-more-prong sample and estimate the tagging efficiency from the Weizacker Williams approximation.

Of the 10 tagged multiprongs 4.6 ± 3.5 are estimated to be accidentals using the accidental rate derived from tagged Bhabhas. This leaves 5.4 ± 3.5 real tagged multiprongs. Using the Weizacker-Williams approximation for the equivalent photon spectrum (see section V-B4), we estimate the fraction of two-photon multiprongs tagged to be .048 ± .010. This means we expect 114 "untagged" events or an effective cross section in our detector of

$$\sigma_{e^+e^- \to e^+e^-x} = .21 \pm .14 \text{ nb.}$$

This accounts for about 2.0% ± 1.3% of all three-or-more-prong events in the detector.

There are many ways to estimate what this cross section should be. Brodsky et al.[12] estimate the cross section for three or more hadrons to be .3 μb and calculate

$$\sigma_{e^+e^- \to e^+e^-x}(E = 2.4 \text{ GeV}) = .4 \text{ nb}.$$

This of course does not include the requirement of our detector that two or more charged tracks must be detected within $|\cos\theta| < .6481$ and $p \gtrsim 150$ MeV/c. Taking this into account our measurement is in excellent agreement with this estimate.

It will ultimately be of interest to use the two-photon multi-hadron events to study deep inelastic electron-photon scattering. Here one electron is tagged and used to provide a spectrum of equivalent photons, while the other is scattered at a large angle from that photon as in Fig. 49.

The cross section can then be expressed in terms of structure functions as

$$\frac{d\sigma_{e\gamma\to ex}}{d\,Q^2\,d\nu} = -\frac{2\pi\alpha^2}{(Q^2)^2}\left[W_2(Q^2,\nu)(1-y) + W_1(Q^2,\nu)\frac{y^2Q^2}{2\nu^2}\right]$$

where W_1 and W_2 are defined by

$$(2\pi)^2 2P_0 \sum_n \langle p|J_\mu(0)|n\rangle\langle n|J_\nu(0)|p\rangle (2\pi)^4\delta^4(q + P - P_n)$$

$$= -\left(g_{\mu\nu} - \frac{q_\mu q_\nu}{q^2}\right) W_1(Q^2,\nu) + \left(P_\mu - \frac{(P\cdot q)q_\mu}{q^2}\right)\left(P_\nu - \frac{(P\cdot q)q_\nu}{q^2}\right) W_2(Q^2,\nu)$$

and

$$\nu = q\cdot P_\gamma\,, \quad Q^2 = -q^2\,, \quad y = \frac{\nu}{P_e\,P_\gamma}\,.$$

Substituting an equivalent photon spectrum for the tagged electron, one could, with a large amount of data, determine the

DEEP INELASTIC ELECTRON-PHOTON SCATTERING

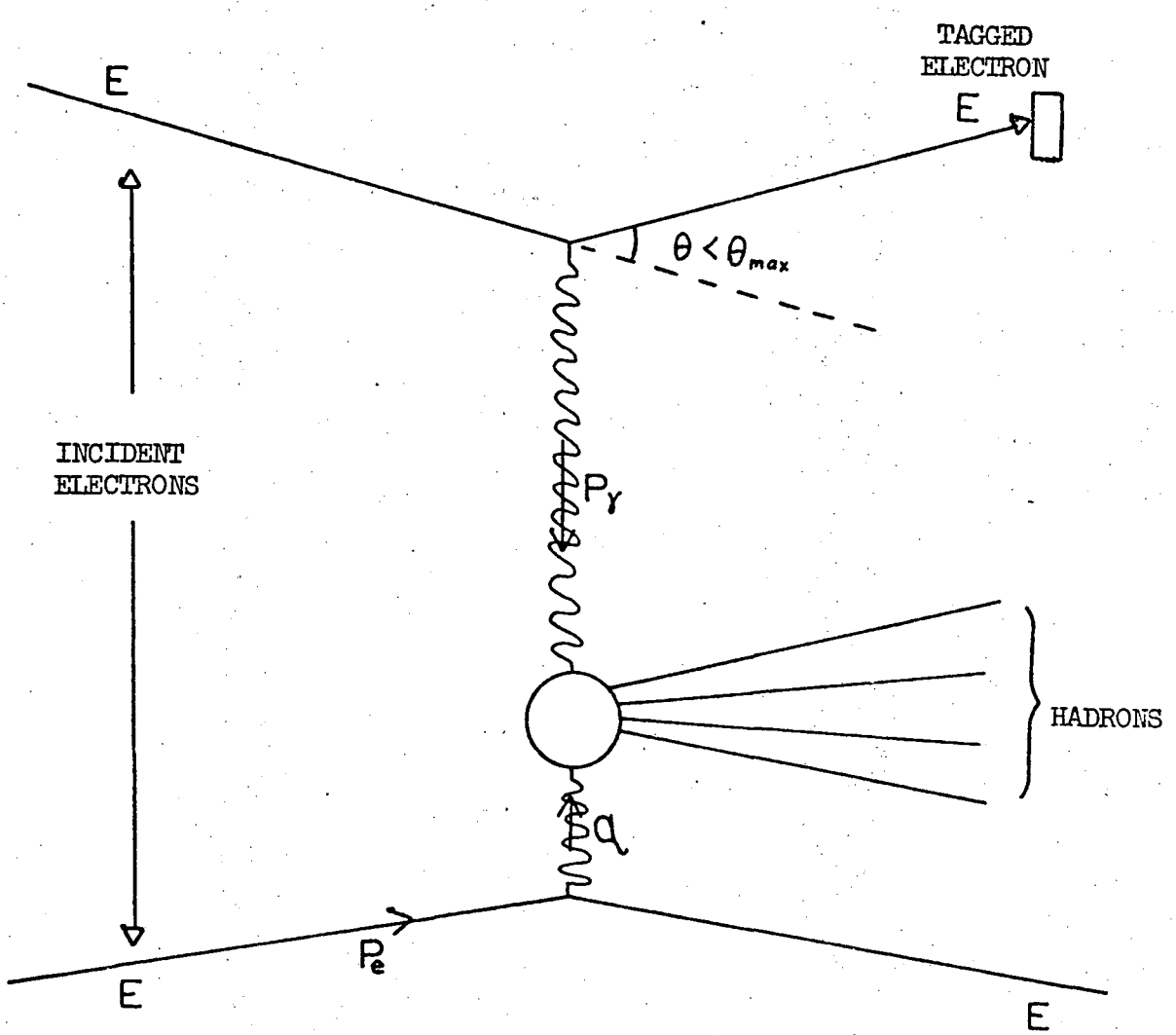

XBL 756-1730

Figure 49

dependence of the structure functions on Q^2 and ν. Unfortunately, we have only ten candidates for events of which none clearly show the presence of the strongly scattered electron in the detector. We cannot give measurements for W_1 and W_2; however, if Brodsky's estimate of the expected cross section for such events,[27]

$$\sigma_{e^+e^- \to e^+e^-x} \simeq .05 \text{ nb},$$

is accurate, we are not far from contributing in this area.

VI. Conclusion

The results of SPEAR to date have been impressive. Here we have increased the validity of hadronic results by demonstrating a clear understanding of the quantum electrodynamic processes which are present. QED is closely obeyed in this experiment and the tightest limits to date have been placed on QED breakdown models.

The two-photon processes have been shown to be present with expected coplanarity and momentum distributions. Twelve singly tagged events and 1 doubly tagged event have been seen and cross sections fall well within the limits of our calculations. We are just at the brink of being able to study the hadron physics of the two-photon process. The process $e^+e^- \rightarrow e^+e^-\pi^+\pi^-$ has been shown to be consistent with the pointlike calculation.

The future of SPEAR promises to bring many new results. Two-photon processes can be studied in more detail at higher energies, and a new frontier of hadronic physics has opened up in the one-photon channel. The success of the project continues.

REFERENCES

1. J. E. Augustin et al., Phys. Rev. Lett. 34, 764 (1975).
2. J. E. Augustin et al., Phys. Rev. Lett. 33, 1406 (1974).
3. G. S. Abrams et al., Phys. Rev. Lett. 33, 1453 (1974).
4. A. M. Boyarski et al., Phys. Rev. Lett. 34, 762 (1975).
5. G. S. Abrams et al., Phys. Rev. Lett. 34, 1181 (1975).
6. A. M. Boyarski et al., Phys. Rev. Lett. 34, 1357 (1975).
   A. M. Boyarski et al., SLAC-PUB-1599, Stanford Linear Accelerator Center, Stanford, California.
7. J. A. Kadyk et al., LBL-3687, Lawrence Berkeley Laboratory, Berkeley, California.
   V. Luth et al., SLAC-PUB-1617, Stanford Linear Accelerator Center, Stanford, California.
8. A. M. Boyarski et al., Phys. Rev. Lett. 34, 195 (1975).
9. F. A. Berends et al., Nucl. Phys. B57, 381 (1973).
10. F. A. Berends et al., Nucl. Phys. B63, 381 (1973).
11. F. A. Berends et al., Nucl. Phys. B68, 541 (1974).
12. S. J. Brodsky et al., Phys. Rev. D4, 1532 (1971).
13. D. E. Fries, SLAC-PUB-99, Stanford Linear Accelerator Center, Stanford, California.
14. R. J. Hollebeek, Ph.D. Thesis, LBL-3874, Lawrence Berkeley Laboratory, Berkeley, California.
15. H. L. Lynch et al., SLAC-PUB-1536, Stanford Linear Accelerator Center, Stanford, Calfornia.

16. G. J. Feldman and M. L. Perl, "Electron-Positron Annihilation above 2 GeV and the New Particles," to be published.

17. J. E. Augustin et al., Phys. Rev. Lett 34, 233 (1975).

18. B. L. Beron et al., Phys. Rev. Lett. 33, 663 (1974).

19. S. D. Drell, Ann. Phys. 4, 75 (1958).

20. T. D. Lee and G. C. Wick, Nucl. Phys. B9, 209 (1969).

21. J. Parisi, Journal de Physique V35, March 1974.

22. N. Arteaga-Romero et al., Phys. Rev. D3, 1569 (1971).

23. N. Arteaga-Romero et al., Lett. Nuovo Cimento IV, 933 (1970).

24. N. Arteaga-Romero et al., C. R. Acad. Sc. 269B, 1129 (1969).

25. V. N. Baier and V. S. Fadin, Lett. Nuovo Cimento 1, 481 (1971).

26. S. J. Brodsky, SLAC-PUB-1322, Stanford Linear Accelerator Center, Stanford, California.

27. S. J. Brodsky, Proc. Int. Sym. on e^+e^- Ints. at High Energies, N. B. Mistry (ed.) (Cornell University Press, Ithaca, N. Y., 1972).

28. A. M. Altuknov, Sov. Jour. Nucl. Phys. 14, 220 (1972), Yad. Fiz. 14, 391 (1971).

29. S. J. Brodsky et al., Phys. Rev. Lett 25, 972 (1970).

30. V. N. Baier and V. S. Fadin, Phys. Lett. 35B, 156 (1971).

31. H. Terazawa, Rev. Mod. Phys. 45, 615 (1973).

32. G. Bonneau et al., Nucl. Phys. B54, 573 (1973).

33. H. Cheng and T. T. Wu, Phys. Lett. 36B, 3 (1973).

34. H. Cheng and T. T. Wu, Nucl. Phys. B32, 461 (1971).

35. G. Grammer and T. Kinoshita, CLNS 201, Cornell University Press, Ithaca, N.Y.

36. C. J. Brown and D. H. Lythe, Nucl. Phys. B53, 323 (1973).

37. A. I. Akhiezer and V. B. Berestetski, Quantum Electrodynamics (Interscience, 1965), pp. 843, 845.

38. P. R. Bevington, Data Reduction and Error Analysis for the Physical Sciences (McGraw-Hill, New York, 1969), p. 70.

39. F. E. Low, Phys. Rev. 120, 582 (1960).

40. V. E. Balakin et al., Phys Lett., 34B, 663 (1971).

41. C. Bacci et al., Lett. Nuovo Cimento 3, 703 (1972).

42. G. Barbiellini et al., Phys. Rev. Lett. 32, 385 (1974).

APPENDIX A

Proof that $\dfrac{\partial(\phi_x, \cos\psi)}{\partial(\phi_1, \phi_2)} = |\sin\psi|$

We must write ϕ_x and $\cos\psi$ in terms of ϕ_1 and ϕ_2 and other variables of integration (W_1, W_2, θ_1, θ_2 E_1', θ_1')

$$\cos\psi = -\cos(\phi_1 - \phi_2)$$

$$\sin\phi_x = \frac{q_1\sin\theta_1\sin\phi_1 + q_2\sin\theta_2\sin\phi_2}{q_x\sin\theta_x}$$

$$q_x^2 = q_1^2 + q_2^2 + 2q_1q_2(\cos\theta_1\cos\theta_2 + \sin\theta_1\sin\theta_2\cos(\phi_1 - \phi_2))$$

$$\cos\theta_x = \frac{1}{q_x}(q_1\cos\theta_1 + q_2\cos\theta_2).$$

Differentiating

$$d(\cos\psi) = \sin(\phi_1 - \phi_2)d\phi_1 - \sin(\phi_1 - \phi_2)d\phi_2$$

$$\cos\phi_x d\phi_x = \frac{q_1\sin\theta_1}{q_x\sin\theta_x}\cos\phi_1 d\phi_1 + \frac{q_2\sin\theta_2}{q_x\sin\theta_x}\cos\phi_2 d\phi_2$$

$$- \frac{\sin\phi_x}{q_x\sin\theta_x} d(q_x\sin\theta_x)$$

$$= Ad\phi_1 + Bd\phi_2 + \frac{\sin\phi_x}{q_x\sin\theta_x}\frac{q_1q_2\sin\theta_1\sin\theta_2}{q_x\sin\theta_x}$$

$$\sin(\phi_1 - \phi_2)(d\phi_1 - d\phi_2)$$

$$= (A + C)\, d\phi_1 + (B - C)\, d\phi_2$$

where

$$A = \frac{q_1\sin\theta_1}{q_x\sin\theta_x}\cos\phi_1$$

$$B = \frac{q_2 \sin\theta_2}{q_x \sin\theta_x} \cos\phi_2$$

$$C = \frac{\sin\phi_x}{q_x \sin\theta_x} \frac{q_1 q_2 \sin\theta_1 \sin\theta_2}{q_x \sin\theta_x} \sin(\phi_1 - \phi_2).$$

The Jacobian can now be calculated:

$$J = \left| \frac{(\phi_x, \cos\psi)}{(\phi_1, \phi_2)} \right| = \begin{vmatrix} \frac{A + C}{\cos\phi_x} & \frac{B - C}{\cos\phi_x} \\ \sin(\phi_1 - \phi_2) & -\sin(\phi_1 - \phi_2) \end{vmatrix}$$

$$= \left| (A + B) \frac{\sin(\phi_1 - \phi_2)}{\cos\phi_x} \right|$$

$$= \left| \frac{q_1 \sin\theta_1 \cos\phi_1 + q_2 \sin\theta_2 \cos\phi_2}{q_x \sin\theta_x \cos\phi_x} \sin(\phi_1 - \phi_2) \right|$$

$$= |\sin(\phi_1 - \phi_2)| = |\sin\psi|.$$

APPENDIX B

Derivation of $\frac{d\sigma_{ee}^{(0)}}{d\theta_1 d\theta_2}$ by Equivalent Photon Method, following Brodsky et al.[12] We start with formula :

$$\sigma_{ee}(E) = \int_0^E \frac{d\omega_1}{\omega_1} \int_0^E \frac{d\omega_2}{\omega_2} N(\omega_1)\, N(\omega_2)\, \sigma_{\gamma\gamma}(\omega_1, \omega_2)$$

and calculate the quantity:

$$\frac{d\sigma_{ee}(E)}{d\theta_1 d\theta_2} = \int_0^E \frac{d\omega_1}{\omega_1} \int_0^E \frac{d\omega_2}{\omega_2} N(\omega_1)\, N(\omega_2)\, \frac{d\sigma_{\gamma\gamma}(\omega_1,\omega_2)}{d\theta_1 d\theta_2}$$

We will further use the approximations of the equivalent photon method by assuming that both photons travel along the z axis. Then letting s be the invariant mass squared of the γ-γ system, we have

$$\omega = \omega_1 + \omega_2 \qquad\qquad q = \omega_1 - \omega_2$$

$$s = \omega^2 - q^2 = 4\omega_1\omega_2$$

and

$$\frac{d\sigma_{ee}(E)}{d\theta_1 d\theta_2} = \int_{4m_f^2}^{4E^2} \frac{ds}{s} \int_{\sqrt{s}}^{E+s/4E} \frac{d\omega}{|q|} \sum_{q=\pm|q|} N(\omega_1)N(\omega_2)\, \frac{d\sigma_{\gamma\gamma}(\omega,q)}{d\theta_1 d\theta_2}$$

We must now calculate $\frac{d_{\gamma\gamma}\ (\omega,q)}{d\theta_1 d\theta_2}$ and, following Brodsky et al,[12] we will now define it in terms of

$$G(W_1,\theta_1) = 1/2\rho_1\rho_2\ 1/4\,|M|^2$$

where $\rho_i = 2\ M_f$ for fermions and $\rho_i = 1$ for bosons, and $|M|^2$ is the invariant matrix element summed over initial and final spins. We have

$$\frac{d\sigma_{ee}(E)}{d\theta_1 d\theta_2} = \int_{4m_f^2}^{4E} \frac{ds}{s} \int_{\sqrt{s}}^{E+s/4E} \frac{d\omega}{|q|} \sum_{q=\pm|q|} N(\omega_1)N(\omega_2)\, \frac{e^4}{(2\pi)^2}\, \frac{1}{2}\, \frac{1}{2\omega_1 2\omega_2}$$

(cont. below)

$$\frac{q_1{}^2 dq_1 \sin\theta_1 d\phi_2}{2W_2} \frac{q_2{}^2 dq_2 \sin\theta_2 d\phi_2}{2W_2} 2\delta^4(\omega_1 + \omega_2 - q_1 - q_2) G(W_1, \theta_1)$$

$$= 2\pi\alpha^2 \int_{4m_f{}^2}^{4E^2} \frac{ds}{s^2} \sum_{q=\pm|q|} N(\omega_1) N(\omega_2) G(W_1, \theta_1) \frac{q_1{}^2 q_2{}^2 \sin\theta_1 \sin\theta_2}{|q| W_1 W_2}$$

$$\theta\left(\left(E - \frac{s}{4E}\right)^2 - q^2\right) d\omega dq_1 dq_2 d\phi_2 \delta^4(\omega_1 + \omega_2 - q_1 - q_2).$$

It remains only to cancel the four dimensional delta function against $d\omega dq_1 dq_2 d\phi_2$ as follows:

$$d\omega dq_1 dq_2 d\phi_2 \delta^4(\omega_1 + \omega_2 - q_1 - q_2)$$

$$= d\omega dq_1\, dq_2 d\phi_2 \delta(\omega - \omega_1 - \omega_2) \delta(q_1 \cos\theta_1 + q_2 \cos\theta_2 - \sqrt{\omega^2 - s}\,)$$

$$\delta(q_1 \sin\theta_1 \cos\phi_1 + q_2 \sin\theta_2 \cos\phi_2)\ \delta\ (q_1 \sin\theta_1 \sin\phi_1 + q_2 \sin\theta_2 \sin\phi_2)$$

$$= dq_1 dq_2 d\phi_2 \delta(q_1 \cos\theta_1 + q_2 \cos\theta_2 - q^*) \delta(q_1 \sin\theta_1 \cos\phi_1 + q_2 \sin\theta_2 \cos\phi_2)$$

$$\delta(q_1 \sin\theta_1 \sin\phi_1 + q_2 \sin\theta_2 \sin\phi_2)$$

$$= dq_1 dq_2 \frac{1}{q_2 \sin\theta_2 |\cos\phi_2{}^*|} \delta(q_1 \cos\theta_1 + q_2 \cos\theta_2 - q^*)$$

$$\delta(q_1 \sin\theta_1 \cos\phi_1 + q_2 \sin\theta_2 \cos\phi_2^*)$$

$$= dq_1 \frac{1}{q_2{}^* \sin^2\theta_2} \delta(q_1 \cos\theta_1 + q_2{}^* \cos\theta_2 - q^{**})$$

$$= \frac{1}{q_2 \sin^2\theta_2} \left\{ \left| \cos\theta_1 + \frac{\sin\theta_1 \cos\theta_2}{\sin\theta_2} - \frac{\omega\left(\frac{q_1}{W_1} + \frac{q_2}{W_2} \frac{\sin\theta_1}{\sin\theta_2}\right)}{q} \right| \right\}^{-1}$$

$$= \frac{W_1 W_2 |\sin(\theta_1 + \theta_2)|}{q_2 \sin\theta_2} \left\{ \omega W_1 \sin^2\theta_1 + \omega W_2 \sin^2\theta_2 - W_1 W_2 \sin^2(\theta_1 + \theta_2) \right\}^{-1}$$

where we had $q^* = \pm\sqrt{q_1{}^2 + q_2{}^2 + 2m_f{}^2 + 2\sqrt{q_1{}^2 + m_f{}^2}\ \sqrt{q_2{}^2 + m_f{}^2} - s}$

$$\phi_2{}^* = \sin^{-1}\left(\frac{q_1\sin\theta_1}{q_2\sin\theta_2}\quad \sin\phi_1\right)$$

$$q_2{}^* = q_1\,\frac{\sin\theta_1}{\sin\theta_2}$$

$$q_2{}^{**} = \pm\sqrt{q_1{}^2 + q_2{}^{*2} + 2\,m_f{}^2 + 2\sqrt{q_1{}^2+m_f{}^2}\,\sqrt{q_2{}^2+m_f{}^2}\;-\;s}\;.$$

The result is

$$\frac{d\sigma_{ee}(E)}{d\theta_1 d\theta_2} = 2\pi\alpha^2 \int_{4m_f{}^2}^{4E^2} \frac{ds}{s^2}\; N(\omega_1)N(\omega_2)G(W_1,\theta_1)$$

$$\frac{q_1{}^2\sin\theta_1 q_2|\sin(\theta_1+\theta_2)|}{|q|(\omega W_1\sin^2\theta_1+\omega W_2\sin^2\theta_2-W_1W_2\sin^2(\theta_1+\theta_2))}\;\theta\left[(E-\frac{s}{4E})^2 - q^2\right]$$

where only one of the values $q = \pm|q|$ is permissable. We determine the variables by

$$a_1 = \left[\frac{\sin\theta_1}{\sin(\theta_1+\theta_2)}\right]^2 \qquad a_2 = \left[\frac{\sin\theta_2}{\sin(\theta_1+\theta_2)}\right]^2$$

$$q^2 = \frac{2\{a_1a_2s^2-m_f{}^2[a_1+a_2-(a_1-a_2)^2]s+m_f{}^4\}^{1/2} - (a_1+a_2-1)s - 2m_f{}^2}{4a_1a_2 - (a_1+a_2-1)^2}$$

$$q = \frac{|q\sin(\theta_1+\theta_2)|}{\sin(\theta_1+\theta_2)}$$

$$q_1 = \frac{q\sin\theta_2}{\sin(\theta_1+\theta_2)} \qquad q_2 = \frac{q\sin\theta_1}{\sin(\theta_1+\theta_2)}$$

$$W_1 = \sqrt{q_1{}^2+m_f{}^2} \qquad W_2 = \sqrt{q_2{}^2+m_f{}^2}$$

$$\omega = \sqrt{s+q^2}$$

$$\omega_1 = \frac{1}{2}(\omega+q) \qquad \omega_2 = \frac{1}{2}(\omega-q)$$

$$E_1{}' = E-\omega_1 \qquad E_2{}' = E-\omega_2.$$

Note the change in definition ($\theta_2 \to \pi - \theta_2$) when comparing with formula 5.11 of reference 12.

Finally the function G for spins 0 or 1/2 is calculated by Akhiezer and Berestetski[37] and given by Brodsky et al.[12]:

$$G_\pi(W_1,\theta_1) = \frac{1}{8}\,|M|^2$$

$$= 1 - \frac{2m_f^2}{W_1^2}\left(1 - \frac{m_f^2}{W_1^2}\right)\frac{\sin^2\theta_1}{\left[1-\left(1 - \frac{m_f^2}{W_1^2}\right)\cos^2\theta_1\right]^2}$$

$$G_\mu(W_1,\theta_1) = \frac{1}{8}\,4m_f^2|M|^2$$

$$= 2 + 4\left(1 - \frac{m_f^2}{W_1^2}\right)\frac{\left(1 - \frac{m_f^2}{W_1^2}\right)\sin^2\theta_1\cos^2\theta_1 + \frac{m_f^2}{W_1^2}}{\left[1 - \left(1 - \frac{m_f^2}{W_1^2}\right)\cos^2\theta_1\right]^2}\,.$$

LEGAL NOTICE

This report was prepared as an account of work sponsored by the United States Government. Neither the United States nor the United States Energy Research and Development Administration, nor any of their employees, nor any of their contractors, subcontractors, or their employees, makes any warranty, express or implied, or assumes any legal liability or responsibility for the accuracy, completeness or usefulness of any information, apparatus, product or process disclosed, or represents that its use would not infringe privately owned rights.

TECHNICAL INFORMATION DIVISION
LAWRENCE BERKELEY LABORATORY
UNIVERSITY OF CALIFORNIA
BERKELEY, CALIFORNIA 94720